Utilization of Nanoparticles for Photoacoustic Chemical Imaging

By

Chang Heon Lee

A dissertation submitted in partial fulfillment
of the requirements for the degree of
Doctor of Philosophy
(Chemistry)
in the University of Michigan
2018

Doctoral Committee:

Professor Raoul Kopelman, Co-Chair
Professor Xueding Wang, Co-Chair
Professor Zhan Chen
Professor Robert Kennedy
Professor Duxin Sun

Chang Heon Lee

lechang@umich.edu

ORCID iD: 0000-0002-4649-833X

DEDICATION

This thesis is dedicated to everyone from enemies to lovers who have shaped me who I am today.

ACKNOWLEDGEMENTS

First of all, I would like to express my profound gratitude to the co-chairs of my dissertation committee, Prof. Raoul Kopelman and Prof. Xueding Wang, for their invaluable lessons and influence on my research and life.

At the end of my second rotation in winter 2014, I was unable to find a lab to join. I still remember the email from the department's graduate chair at that time stating that I would be asked to leave the program if I cannot find a lab to join by the end of summer 2014. Among several faculties that I spoke to, Prof. Raoul Kopelman gave me the most firm answer giving me another chance to stay in the program. When I first met Prof. Kopelman, I was surprised to see how he is still excited to talk about his research. It was hard for me to think such an accomplished and well-established professor to still be enthusiastic about the research. His passion for science and research has truly inspired me of how a scientist should be. As a mentor, he always tries to motivate me rather than to force me to work, which, I believe, aims to frame a responsible and independent researcher. Now that I look back, I was really lacking in motivation for research and pursuing PhD. I truly believe that if I have not worked for Prof. Kopelman, I would have quit graduate school by now.

Soon after I joined the Kopelman group, I had my first meeting with Prof. Xueding Wang to discuss about future projects and plans. During the meeting, he asked me on some background photoacoustic imaging questions for the project. Rather than answering his questions, I answered,

"I don't think I'm responsible to know photoacoustic imaging since I am a chemist." He calmly responded to my ignorance and explained why I should learn photoacoustic imaging to have a successful collaboration and be a successful PhD candidate. I truly appreciated his thoughts and concerns for me, and it really changed my entire perspectives on collaboration in general. For just a graduate student from a collaborator's lab, he gave me endless support and advice, which might not be the best investment of his time and effort. About a year ago, when Prof. Wang became a co-chair in my dissertation committee, I was glad since he had always been an "unofficial" co-advisor for me.

I would like to thank my committee members, Prof. Zhan Chen, Prof. Robert Kennedy, and Prof. Duxin Sun for their help and wonderful guidance. Prof. Chen's Analysis Spectroscopic and Imaging course was one of the most useful and practical courses I have taken in this school for my research. His questions and comments during the Candidacy Exam were challenging, but inspiring. Prof. Kennedy has always been supportive of me. His compliments and thoughtful critiques have helped me to gain my confidence before and after oral exams. I truly appreciate Prof. Sun to be on my dissertation committee at such a short notice. His expertise in cancer biology has truly influenced my plans after the Data Meeting.

I would also like to express my gratitude to my former collaborators, Prof. Jerome Kalifa and Dr. Uma M. R. Avula. The first project that I was assigned to work on was in collaboration with Prof. Kalifa's group. Prof. Kalifa has been extremely supportive of me and my ideas. He always made himself available if I had any questions or suggestions. His brilliant ideas were inspiring, and I have no doubt that his visions will come true and have great impacts in the field. Uma has

been a good friend and a good teacher. Whenever I wanted to do *in vitro* or confocal microscope experiments, he had always given me help and advice.

The life of a PhD candidate can be challenging, but it has been soothed with my colleagues in the Kopelman group, especially my former mentor, Dr. Hyung Ki Yoon, who recommended to me to join the Kopelman group and taught me everything he knew (he literally told me "I have taught you everything I know") within 3 months before he left. Senior group members, Dr. Ming Qin, Dr. Teppei Shirakura, Dr. Leshern Karamchand, and Dr. Remy Elbez, had numerous discussions with me and gave precious advice. It is always pleasing to have discussions with my colleagues, Dr. Wei Qian, Dr. Priyanka Yadav, Binyamin Jacobovitz, Thomas Hopkins, Jeff Folz (also my former mentee), and Alan McLean. I also like to thank my past and current mentees, Dena Lowing, Steven Shawn, Edward Kim, Wuliang Zhang, and Iman William. I would also like to thank some of my colleagues/collaborators, Dr. Guan Xu (Gary), Joel Tan, and Wei Zhang, for helpful discussions and support in the Wang group.

None of the work presented in this thesis can be done without my mentor Dr. Janggun Jo in the Wang group. I have worked with Dr. Jo since the very beginning. When experiments do not go as I expect them to be, I become a little cranky. As a person who has to work with me in that state most of the times, I believe it can be very stressful sometimes. However, he never complained and always tried to stay calm to find the solutions. He always tried to answer my questions as much as possible to the best of his ability (this one time, he had to teach me an algorithm more than a few days until I felt comfortable discussing about it for a conference presentation.), and he was always available to consult with me for personal issues outside of science.

The work presented in this thesis was supported by NIH/NCI under the grant number R01CA186769 (R.K. and X.W.). I also would like to acknowledge generous fellowships/grants from the George Ashworth Endowment, Rackham Graduate School and Department of Chemistry, such as George Ashworth Analytical Chemistry Fellowship, One Term Dissertation Fellowship, Rackham Graduate Student Research Grant, Rackham Conference Travel Grant, and Chemistry Departmental Fellowship.

Last but not least, I want to express my great gratitude to my parents, Kee Hee Lee and Mi Seop Byun, and to my brother, Dai Heon Lee, for their endless support. I also would like to thank all of my friends for always being there for me. Nothing could have been accomplished without you.

TABLE OF CONTENTS

LIST OF FIGURES

ABSTRACT

Tumors are known to have unique chemical properties, such as low pH (acidosis), high K^+ (hyperkalemia), and low O_2 (hypoxia). Tumor acidosis has been known to influence therapeutic activities of chemotherapeutic drugs. Another conventional cancer treatment, radiation therapy, is highly dependent on local oxygen concentrations. Hyperkalemia has been recently reported to suppress the immune response of activated T-cells. It is also believed that the spatial distribution of these analytes and its heterogeneity, are of relevance. Despite the importance of such chemical information on tumors, there are no clinically available tools for "quantitative" pH, K^+, or tissue O_2 imaging. Here, photoacoustic (PA) imaging is employed to provide chemical imaging of all these target analytes for cancer (pH, O_2 and K^+). As for pH, we report on an *in vivo* pH mapping nanotechnology. This subsurface chemical imaging is based on tumor-targeted, pH sensing nanoprobes and multi-wavelength photoacoustic imaging (PAI). The nanotechnology consists of an optical pH indicator, SNARF-5F, 5-(and-6)-Carboxylic Acid, encapsulated into polyacrylamide nanoparticles with surface modification for tumor targeting. Facilitated by multi-wavelength PAI plus a spectral unmixing technique, the accuracy of pH measurement inside the biological environment is not susceptible to the background optical absorption of biomolecules, i.e., hemoglobins. As a result, both the pH levels and the hemodynamic properties across the entire tumor can be quantitatively evaluated with high sensitivity and high spatial resolution in *in vivo* cancer models. For K^+, we extend this technique to ion-selective photoacoustic optodes (ISPAOs) that serve at the same time as fluorescence-based ISOs, and apply it specifically to potassium (K^+).

However, unfortunately, sensors capable of providing potassium images *in vivo* are still a future proposition. Here, we prepared an ion-selective potassium nanosensor (NS) aimed at *in vivo* photoacoustic (PA) chemical imaging of the extracellular environment, while being also capable of fluorescence based intracellular ion-selective imaging. This potassium nanosensor (K^+ NS) modulates its optical properties (absorbance and fluorescence) according to the potassium concentration. The K^+ NS is capable of measuring potassium, in the range of 1 mM to 100 mM, with high sensitivity and selectivity, by ISPAO based measurements. Also, a near infrared dye surface modified K^+ NS allows fluorescence-based potassium sensing in the range of 20 mM to 1 M. The K^+ NS serves thus as both PA and fluorescence based nanosensor, with response across the biologically relevant K^+ concentrations, from the extracellular 5 mM typical values (through PA imaging) to the intracellular 150 mM typical values (through fluorescence imaging). Lastly, nano-enabled tissue O_2 monitoring by PA, called lifetime-based PA (PALT) imaging, was introduced and demonstrated. A known PALT oxygen indicator, Oxyphor G2, is conjugated into polyacrylamide nanoparticles, called G2-PAA NP. The oxygen sensing capability of the G2-PAA NP has been confirmed *in vitro* and *in vivo* studies. In an Appendix, we show how to monitor photodynamic therapy (PDT) using the PALT approach to measure the local oxygen depletion as a function of PDT time. Oxygen depletion during PDT is monitored using both oximeter and PALT spectroscopy *in vitro*. The latter is enabled by theranostic NPs of methylene blue (MB) conjugated PAA, used for both PALT and PDT. This synergistic approach has good potential for personalized medicine.

Chapter 1: Introduction

Today, cancer still remains one of the most fatal diseases. Among recent advances in cancer treatments, nanotechnology has received much attention due to its uniquely appealing features for drug delivery, diagnostics, and imaging. Nanoparticles, containing active molecules such as therapeutic drugs, biomacromolecular drugs, imaging contrast agents, etc., have been developed specifically for cancer treatments. Several nanoparticles are already FDA approved for cancer treatments and many are under clinical trials.[1-4] Here, novel methods for imaging tumor chemical footprints, specifically pH, tissue O_2, and K^+, are introduced.

1.1 Advantages of Nanotechnology in Cancer medicine

Cancer is formed as a result of uncontrollable cellular regeneration. Cancer cells strive for more oxygen and nutrients from blood as they require excessive energy for continuous cellular regeneration. Tumors, therefore, induce new blood vessel growth (angiogenesis) in order to compensate for the lack of nutrients and oxygen supplied for tumor cells that are distant from the regular blood vessels. Unlike regular blood vessels, new blood vessels formed by tumors are irregularly shaped, with leaky vasculature and lower blood pressure.

NPs (typically from 10 nm to 100 nm) are too large to penetrate through the regular blood vessels, but they are small enough to penetrate through the angiogenic blood vessels. This phenomenon grants NPs a passive targeting ability (Enhanced Permeability and Retention effect).

Due to the size of the NPs, they are not easily removed from the new blood vessels and accumulate around tumors. Besides the passive targeting ability, the surfaces of NPs can be easily engineered with one or more specific targeting moieties, such as RGD-peptide, F3-peptide, UM-A9 antibody, etc., granting active targeting ability.[5-17]

The targeting ability (both passive and active targeting) of NPs is highly attractive for cancer medicine. For example, most chemotherapeutic drugs are essentially toxins that kill tumor cells. Those drugs are usually not only toxins to the tumor cells, but also to other healthy cells, thus causing serious side effects. When the drugs, by themselves, are injected into the bloodstream, those drugs circulate and spread all throughout the body without recognizing specific targets. Due to this reason, the dosage of the drugs is strictly regulated (i.e. high dosage can cause serious side effects while low dosage can lead to none or less therapeutic efficacy). The targeting ability of NPs can offer a solution for this dilemma, so as to maximize therapeutic efficacy while minimizing side effects.

The surfaces of the NPs are typically covered by polyethylene glycol (PEGylated). PEGylation allows for minimal immune system (such as macrophages) recognition, and thereby, increasing retention time and biocompatibility in the bloodstream.[18] The NP matrix also serves as a protection device for the therapeutic cargoes and/or imaging agents. For example, in the case of pH sensing nanoparticles, the NP matrix protects the indicator dye from interacting with bio-macromolecules, such as albumin. When the free sensing indicator is allowed to interact with human serum albumin, which is the most abundant protein in mammals, the indicator's optical properties, along with that of the pH calibration, changed from their characteristics in an albumin free solution. On the other hand, the nanosensor exhibits no difference, whether in the presence or absence of albumins.[7]

1.2 Chemical footprints of cancer

Besides from their physical characteristics, tumors also exhibit unique chemical characteristics, such as low pH (acidosis), low O_2 (hypoxia), and high K^+ (hyperkalemia). Acidosis and hypoxia are explained by the Warburg Effect.[19] Tumor cells near the blood vessels take up most of the oxygen for themselves, so as to produce more energy, thus reducing the oxygen and nutrients that reach tumor cells far away from the blood vessels. As a result, the core of the tumor (the farthest from the blood vessels) is known to exhibit hypoxia. Tumors also transform their major metabolic pathway from aerobic glycolysis (consumes oxygen) to anaerobic glycolysis (does not consume oxygen). A side product of anaerobic glycolysis, lactic acid, is responsible for the acidic (low pH) tumor microenvironment causing acidosis. The chemically altered states are believed to cause metastasis, local recurrence and angiogenesis.[20-22]

Acquiring chemical information is not only providing valuable information to the study of a cancer's nature, but also can directly be translated into a next generation diagnostics and prognostic tool for personalized medicine. Well known are *hypoxia's* effects of obviating radiation therapy of any kind, from high energy radiation treatments to photodynamic therapy, due to the requirement of such therapies for the local presence of O_2, so as to create the Reactive Oxygen Species (ROS), which kill cells. Furthermore, the influence of local pH in relation to the administration of some of the commercial chemotherapeutic drugs has been reported, e.g. daunorubicin, doxorubicin, and mitoxantrone show reduced therapeutic efficacy under acidic conditions (*acidosis*); while some other drugs, such as chlorambucil, cyclophosphamide, and 5-fluorourcacil, show higher cytotoxicity at lower pH.[23]

More recently, *hyperkalemia* has been reported to be responsible for immunotherapy suppresion.[24] Hyperkalemia is believed to be caused from a necrotic core of a tumor. As a tumor expands, some of the tumor cells lack space, oxygen, and nutrients to survive, leading to necrosis in the core of the tumor, leaving a necrotic core, consisting of necrotic cells and debris surrounded by live tumor cells.[25] Typically, the intracellular potassium concentration is around 150 mM, while the extracellular potassium concentration is around 5 mM. Thus, the necrotic cells and debris cause a local elevation of potassium ion concentrations (around 5 to 10 folds higher than typical for the extracellular potassium concentration).[24]

Although the importance of tumor chemical information has been established, a simple and generally applicable clinical tool that gives spatially resolved quantitative chemical information throughout the tumor is not yet available. Here, a novel chemical imaging method is introduced. By combining nanotechnology and photoacoustic (PA) imaging, the chemical information on a cancerous tumor can be revealed.

1.3 Chemical imaging of cancer (Photoacoustic chemical imaging)

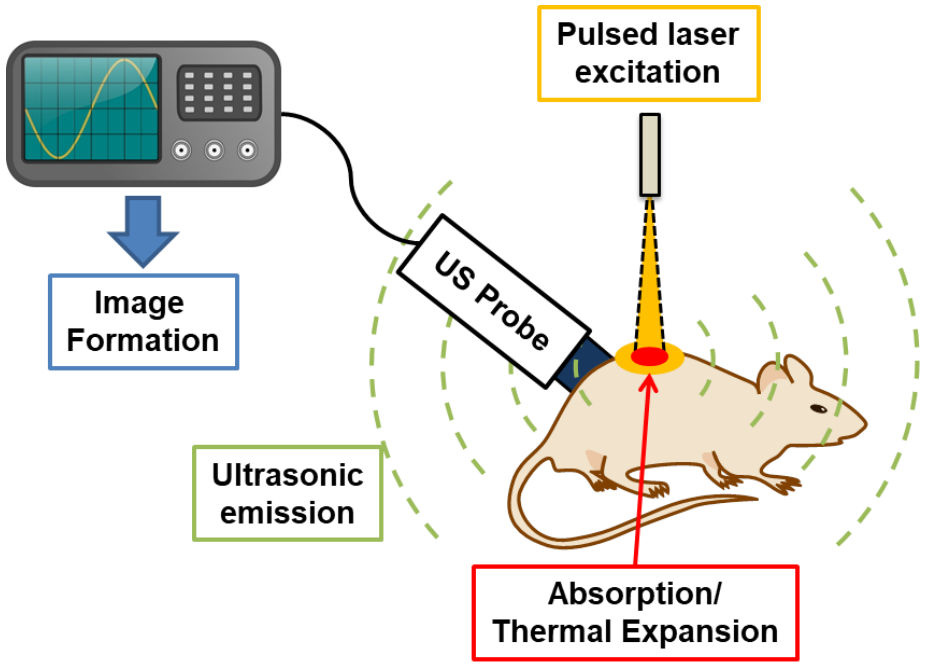

Figure 1.1 Photoacoustic (PA) imaging schematic. Pulsed laser is used to excite the optical contrast agent. Absorption by the laser excitation creates thermal expansion causing ultrasound emission. The ultrasonic emission is detected by an ultrasound (US) probe and the acquired information can be converted into both US and PA images.

Photoacoustic (PA) imaging is a hybrid imaging modality combining in a unique way traditional optical imaging and ultrasound imaging (**Figure 1.1**).[26] An optical contrast agent absorbs pulsed non-ionizing radiation, and converts the excited energy into thermoelastic expansion which induces a slight temperature increase and ultrasonic emission. The initial pressure rise due to a pulsed optical absorption (p_0) can be estimated from

$$p_0 = \Gamma \mu_a F, \tag{1}$$

where Γ is the Grüneisen parameter of the tissue, μ_a is the absorption coefficient, and F is the local light fluence. As shown in equation (1), the PA signal generated correlates linearly with the absorbance of the optical contrast agent, and thus with the optical absorption spectrum. Because

ultrasound travels far better than light in tissues, i.e. with little scattering, its imaging depth is mostly limited by the excitation light, thus providing a deeper tissue imaging ability than traditional optical imaging. Although label-free PA imaging has been widely explored for both structural and functional imaging, well-established optical sensors have also been coupled with PA imaging.[6-8, 27-29]

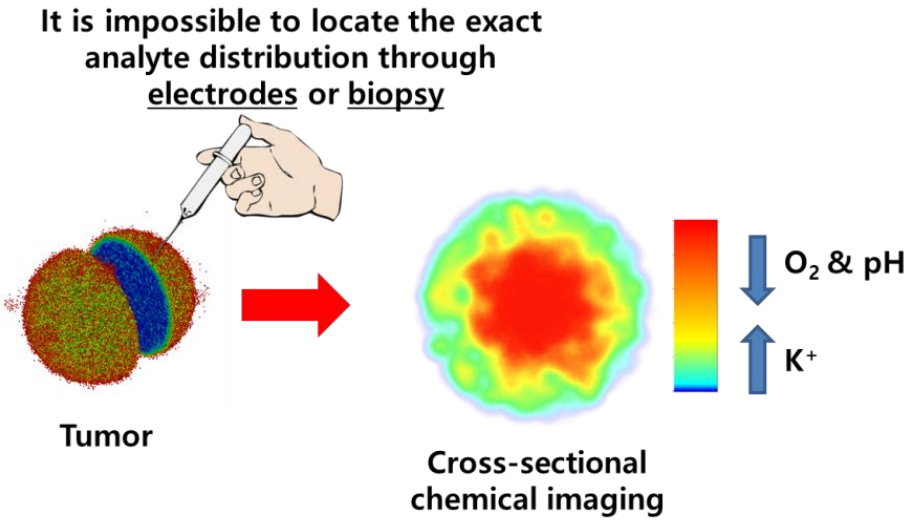

Figure 1.2 Importance of cross-sectional chemical imaging. The O_2 concentration and pH are known to be lower at the core while K^+ concentration is hypothesized to be higher. Colorimetric scale bar for O_2 and pH is indicated by a downward arrow (red is lower and blue is higher), while for K^+ it is indicated by an upward arrow (blue is lower and red is higher).

PA imaging is one of the fastest emerging biomedical imaging tools overcoming the imaging depth limit of traditional optical imaging modalities. PA imaging detects ultrasound, which penetrates far better than light in tissues, rather than light emanating from the sample. Thus, the imaging depth limit is only dependent on the excitation light source thus enabling subsurface (or cross-sectional) images of the tumor chemical environment, which cannot be accomplished with conventional optical imaging. Cross-sectional images of tumors are highly advantageous for

chemical imaging because tumors, as explained in the previous section, have necrotic cores, which have different chemical footprint compared to the boundary of the tumors, thus forming gradients of chemical content (**Figure 1.2**).

1.4 Outline of the Dissertation

This dissertation introduces the development of novel chemical imaging methods (quantitative and qualitative) with nanoparticle based sensors enabled PA imaging. Each chapter is intended to provide a story of developing PA chemical imaging for independent analytes (pH, K^+, and O_2). Nanoparticle based pH, K^+, and O_2 sensors have been prepared and tested with PA spectroscopy and imaging.

Chapter 2 presents the first demonstration of quantitative pH imaging in vivo (tumor model) through photoacoustic imaging.[7] We encapsulated commercially available pH indicator dye, SNARF-5F, into surface modified polyacrylamide nanoparticles. The nanoparticle encapsulation serves not only as a targeted delivery tool but also to protect the SNARF-5F from interference by body proteins or enzymes. Such interference is known to cause changes in the dye's optical properties, thus affecting the pH calibration. Utilizing PA, imaging, we hereby propose a method and present the "transaxial" pH images of tumors in vivo. There are a few recently reported works on PA pH imaging in vivo; however, they are unable to provide quantitative pH images, because of background signal interference due to optical absorption by the tissues. We remove from our images the background signal from the most absorbing factor in biological tissues, namely, "blood", which allows us to directly provide quantitative pH images. According to our study on a mouse cancer model (see example result in Fig. 1), the average pH of the tumors is 6.71 ± 0.22, while the

average pH of normal muscle tissues is 7.46 ± 0.095. These results match with "gold standard" pH electrode measurements done in situ. Moreover, we see the details of the non-homogenous distribution of the pH throughout the tumor, i.e., significant differences between core and periphery acidity.

Chapter 3 presents the first PA and fluorescence optimized potassium sensor.[8, 30] The potassium selective nanosensor (K+ NS) shows excellent response from 1 mM to 100 mM with PA imaging, and from 20 mM to 1 M with fluorescence imaging. Thus, the K+ NS can serve as both extracellular K+ sensor (typical concentration ~5 mM, but for cancer 10 mM to 50 mM) and intracellular K+ sensor (typical concentration ~150 mM. but less for cancer cells after therapy). The K+ NS can be further modified with an external near-infrared (NIR) absorbing/emitting dye. Unlike the absorption characteristics of the K+ NS (two signal peaks at 540 nm and 660 nm), there is a single fluorescence peak; thus, a secondary reference fluorescence peak is needed. Because the K+ NS contains primary amine groups on the surface, it can be utilized for conjugating a targeting moiety and/or an NIR reference dye.

Chapter 4 introduces PA tissue oxygen imaging, called PA lifetime imaging.[27] This method is an extension of time-resolved (or transient) absorption spectroscopy.[6, 28, 29, 31-38] The sensing mechanism is similar to that of phosphorescence quenching based oxygen sensors, but it is measured by PA imaging/spectroscopy, i.e. it is based on optical absorption rather than emission. Nanoparticles containing a known PA oxygen sensing dye, Oxyphor G2, were synthesized. The "proof-of-concept" experiment on the O2 sensing nanoparticle's oxygen sensing capability was performed by generating a calibration curve with photoacoustically measured lifetimes and known oxygen concentrations. Also, an initial experiment on a mouse model *in vivo* has been performed.

The PA lifetime imaging method is able to differentiate tissue oxygen levels.

Lastly, chapter 5 contains a summary of the thesis along with a discussion on current limitations and future directions regarding each project.

The Appendix describes the combining of PA lifetime spectroscopy and photodynamic therapy (PDT). This is another application of the PA lifetime imaging for oxygen sensing. PDT is a promising therapeutic modality for virtually all types of tumors. A photosensitizer (PS), under light excitation, converts oxygen into reactive oxygen species (ROS) that lead to high oxidative stress within the cell, so as to cause cell death. Since the mechanism of PDT is similar to PA lifetime imaging, these can be combined to provide a direct method of monitoring PDT. Employing nano-technology, we used methylene blue (MB), which is a well-known photosensitizer and also a known PA oxygen sensing dye, preparing MB conjugated PAA nanoparticles. The oxygen depletion during PDT was monitored using a gold standard oxygen meter as well as PA lifetime spectroscopy, *in vitro,* as a proof of principle for *in vivo* applications.

1.5 References

1. Ferrari, M. Cancer nanotechnology: opportunities and challenges. *Nature Reviews Cancer* **5**, 161 (2005).
2. Peer, D. et al. Nanocarriers as an emerging platform for cancer therapy. *Nature Nanotechnology* **2**, 751 (2007).
3. Shi, J., Kantoff, P.W., Wooster, R. & Farokhzad, O.C. Cancer nanomedicine: progress, challenges and opportunities. *Nature Reviews Cancer* **17**, 20 (2016).
4. Lee, Y.-E.K., Smith, R. & Kopelman, R. Nanoparticle PEBBLE Sensors in Live Cells and In Vivo. *Annual Review of Analytical Chemistry* **2**, 57-76 (2009).
5. Kopelman, R. et al. Multifunctional nanoparticle platforms for in vivo MRI enhancement and photodynamic therapy of a rat brain cancer. *Journal of Magnetism and Magnetic Materials* **293**, 404-410 (2005).
6. Jo, J., Lee, C.H., Kopelman, R. & Wang, X. Lifetime-resolved Photoacoustic (LPA) Spectroscopy for monitoring Oxygen change and Photodynamic Therapy (PDT). *Proc*

SPIE Int Soc Opt Eng **9708** (2016).
7. Jo, J., Lee, C.H., Kopelman, R. & Wang, X. In vivo quantitative imaging of tumor pH by nanosonophore assisted multispectral photoacoustic imaging. *Nature Communications* **8**, 471 (2017).
8. Lee, C.H. et al. Ion-Selective Nanosensor for Photoacoustic and Fluorescence Imaging of Potassium. *Analytical Chemistry* **89**, 7943-7949 (2017).
9. Orringer, D.A. et al. In Vitro Characterization of a Targeted, Dye-Loaded Nanodevice for Intraoperative Tumor Delineation. *Neurosurgery* **64**, 965-972 (2009).
10. Reddy, G.R. et al. Vascular Targeted Nanoparticles for Imaging and Treatment of Brain Tumors. *Clinical Cancer Research* **12**, 6677-6686 (2006).
11. Moffat, B.A. et al. A Novel Polyacrylamide Magnetic Nanoparticle Contrast Agent for Molecular Imaging using MRI. *Molecular Imaging* **2**, 15353500200303163 (2003).
12. Qin, M., Zong, H. & Kopelman, R. Click Conjugation of Peptide to Hydrogel Nanoparticles for Tumor-Targeted Drug Delivery. *Biomacromolecules* **15**, 3728-3734 (2014).
13. Wang, S. et al. Multifunctional Biodegradable Polyacrylamide Nanocarriers for Cancer Theranostics—A "See and Treat" Strategy. *ACS Nano* **6**, 6843-6851 (2012).
14. Ray, A. et al. Targeted blue nanoparticles as photoacoustic contrast agent for brain tumor delineation. *Nano Research* **4**, 1163-1173 (2011).
15. Winer, I. et al. F3-Targeted Cisplatin-Hydrogel Nanoparticles as an Effective Therapeutic That Targets Both Murine and Human Ovarian Tumor Endothelial Cells In vivo. *Cancer Research* **70**, 8674-8683 (2010).
16. Yoon, H.K. et al. Polymer-Protein Hydrogel Nanomatrix for Stabilization of Indocyanine Green towards Targeted Fluorescence and Photoacoustic Bio-imaging. *Journal of materials chemistry. B, Materials for biology and medicine* **1**, 10.1039/C1033TB21060J (2013).
17. Popovtzer, R. et al. Targeted Gold Nanoparticles enable Molecular CT Imaging of Cancer. *Nano letters* **8**, 4593-4596 (2008).
18. Jokerst, J.V., Lobovkina, T., Zare, R.N. & Gambhir, S.S. Nanoparticle PEGylation for imaging and therapy. *Nanomedicine (London, England)* **6**, 715-728 (2011).
19. Höckel, M. & Vaupel, P. Tumor Hypoxia: Definitions and Current Clinical, Biologic, and Molecular Aspects. *Journal of the National Cancer Institute* **93**, 266-276 (2001).
20. Raghunand, N. et al. Enhancement of chemotherapy by manipulation of tumour pH. *Br J Cancer* **80**, 1005-1011 (1999).
21. Tredan, O., Galmarini, C.M., Patel, K. & Tannock, I.F. Drug resistance and the solid tumor microenvironment. *J Natl Cancer Inst* **99**, 1441-1454 (2007).
22. Kato, Y. et al. Acidic extracellular microenvironment and cancer. *Cancer Cell Int* **13**, 89 (2013).
23. Chen, L.Q. & Pagel, M.D. Evaluating pH in the Extracellular Tumor Microenvironment Using CEST MRI and Other Imaging Methods. *Advances in Radiology* **2015**, 25 (2015).
24. Eil, R. et al. Ionic immune suppression within the tumour microenvironment limits T cell effector function. *Nature* **537**, 539 (2016).
25. Gimbrone, M.A., Leapman, S.B., Cotran, R.S. & Folkman, J. TUMOR DORMANCY IN VIVO BY PREVENTION OF NEOVASCULARIZATION. *The Journal of Experimental Medicine* **136**, 261-276 (1972).

26. Xu, M. & Wang, L.V. Photoacoustic imaging in biomedicine. *Review of Scientific Instruments* **77**, 041101 (2006).
27. Lee, C.H., Jo, J., Wang, X. & Kopelman, R. in Quenched-phosphorescence Dectection of Molecular Oxygen. (eds. D.B. Papkovsky & R.I. Dmitriev) (The Royal Society of Chemistry, 2017 (submitted)).
28. Shao, Q. et al. In vivo photoacoustic lifetime imaging of tumor hypoxia in small animals. *BIOMEDO* **18**, 076019-076019 (2013).
29. Ray, A., Rajian, J.R., Lee, Y.-E.K., Wang, X. & Kopelman, R. Lifetime-based photoacoustic oxygen sensing in vivo. *BIOMEDO* **17**, 0570041-0570044 (2012).
30. Lee, C.H. et al. Correction to Ion-Selective Nanosensor for Photoacoustic and Fluorescence Imaging of Potassium. *Analytical Chemistry* (2017).
31. Ashkenazi, S., Huang, S.-W., Horvath, T., Koo, Y.-E.L. & Kopelman, R. Photoacoustic probing of fluorophore excited state lifetime with application to oxygen sensing. *BIOMEDO* **13**, 034023-034023-034024 (2008).
32. Shao, Q. & Ashkenazi, S. Photoacoustic lifetime imaging for direct in vivo tissue oxygen monitoring. *BIOMEDO* **20**, 036004-036004 (2015).
33. Shao, Q., Biel, M.A. & Ashkenazi, S. in Proceedings of SPIE, Vol. 8931 89310H-89310H-89318 (2014).
34. Shao, Q., Morgounova, E. & Ashkenazi, S. in Proceedings of SPIE, Vol. 8943 89430F-89430F-89436 (2014).
35. Ashkenazi, S. Photoacoustic lifetime imaging of dissolved oxygen using methylene blue. *BIOMEDO* **15**, 040501-040501-040503 (2010).
36. Shao, Q., Morgounova, E. & Ashkenazi, S. in Proceedings of SPIE, Vol. 9323 932320-932320-932324 (2015).
37. Morgounova, E., Shao, Q., Hackel, B.J., Thomas, D.D. & Ashkenazi, S. Photoacoustic lifetime contrast between methylene blue monomers and self-quenched dimers as a model for dual-labeled activatable probes. *BIOMEDO* **18**, 056004 (2013).
38. Forbrich, A., Shao, P., Shi, W. & Roger, J.Z. Lifetime-weighted photoacoustic imaging. *Journal of Optics* **18**, 124001 (2016).

Chapter 2: Quantitative Photoacoustic pH Imaging

This chapter has been adapted from a following publication with minor modifactions:

Jo, J.[1]; **Lee, C. H.[1]**; Kopelman, R.; Wang, X., "In vivo quantitative imaging of tumor pH by nanosonophore assisted multi spectral photoacoustic imaging", *Nature Communications,* **2017**, 8, 471. [1]Indicates co-first authorship (Featured in UM engineering News Center: https://news.engin.umich.edu/2017/09/reading-cancers-chemical-clues/)

2.1 Introduction

The regulation of pH is central to the processes of homeostatic control in mammalian tissues. The pH determines the charge state on proteins and macromolecules. Thus pH change can affect various pathologies, such as inflammation, renal disease, ischemia, chronic lung disease, and intrauterine disorders[1-3]. In cases of cancer, the tumors are often found in an altered metabolic state, which leads to anomalous extracellular chemical composition, such as acidosis (low pH), hypoxia (low oxygen), and/or hyperkalemia (high potassium)[4-7]. Acidity of the tumor is explained by the Warburg Effect, which describes how lack of nutrients and oxygen converts the tumors' metabolic pathway from aerobic glycolysis into anaerobic glycolysis[8]. A side product of anaerobic glycolysis, lactic acid, is responsible for the acidic tumor microenvironment, the excess lactic acid production surpasses the buffering capacity of the body fluid which thus becomes more acidic[8]. The chemically altered states are believed to cause metastasis, local recurrence and angiogenesis, and are among the causes for failure of cancer treatment[9-11]. Although the importance of pathological acidosis has been established, a simple and generally

applicable clinical tool that gives spatially resolved quantitative pH information throughout the tumor is not yet available.

Quantitative *in vivo* pH imaging methods have been developed mostly for magnetic resonance imaging (MRI)[12-14], positron emission tomography (PET)[15, 16], and optical imaging[17-20]. MRI and PET based methods have serious limitations such as high cost and limited access. In addition, MRI cannot be utilized on patients with pacemakers or implants, and PET utilizes ionizing radiation which has safety concerns. Optical spectroscopy based techniques are highly desirable due to many advantages such as low cost, non-invasiveness, and ease of use. Optical pH imaging has been developed for many decades, historically starting with litmus paper. In recent years, numerous near-infrared fluorescent pH indicators have been developed[17-20]. Based on the measurement of the pH-dependent emission spectrum, fluorescence microscopy has been heavily used for pH measurements of cells *in vitro* or of superficial tissues *in vivo*. However, as a result of the strong optical scattering of biological tissues, traditional optical spectroscopy is not able to achieve satisfactory spatial resolution when the target tissue is beyond the sample surface. This limited spatial resolution in imaging subsurface tumor also inevitably leads to limited accuracy in evaluating the cancer microenvironment, because the functional hallmarks of tumor including the acidosis also show strong heterogeneity.

Combining the merits of light and ultrasound, the emerging non-ionizing and non-invasive photoacoustic imaging (PAI) holds the potential to overcome these challenges[21-24]. In PAI, the spatial resolution is not limited by the detection of photons which are highly scattered in most soft tissues, but instead by the detection of ultrasound waves which are much less scattered. Thus, the spatial resolution of PAI is comparable to that of ultrasound (US) imaging which,

especially when working at high frequencies, is superior in delineating the morphology of subsurface solid tumors. Our group, followed by others, has performed some preliminary pH measurements using PAI[20, 25-29]. A well-known ratiometric pH indicator SNARF-5F, i.e. 5-(and-6)-Carboxylic Acid, has been explored for qualitative pH measurement *in vivo*. The emission spectrum of SNARF-5F undergoes a pH-dependent wavelength shift, allowing the ratio of the fluorescence intensities at two emission wavelengths to be used for the measurement of pH. Similar to the emission spectrum, the absorption spectrum of SNARF-5F is also a function of pH. Therefore, following the idea of fluorescent dual-wavelength ratiometric measurement, PA absorption dual-wavelength ratiometric measurement of SNARF-5F has been explored, and its capability in detecting 0.1 pH change has been demonstrated.[29] However, due to the severe background optical absorption in biological tissues (mostly from hemoglobin), none of the previous studies, including ours, has achieved truly quantitative pH measurement of tumor *in vivo*. When the two forms of hemoglobin also contribute to the PA signals, providing accurate spatial pH information is nearly impossible without careful consideration of the background optical absorption spectrum.

In this study, we developed a method for quantitative pH imaging of tumor *in vivo* using PAI. To make the pH sensitive nanosonophores, we encapsulated the commercially available optical pH indicator, SNARF-5F, into polyacrylamide nanoparticles, which we call SNARF-PAA NPs. The NP matrix protects the indicator dye from interacting with large outside molecules, such as albumin, while the surface modification of the NPs makes the pH nano-indicator to be both tumor targeting and immune system avoiding, allowing more efficient and targeted delivery of the pH sensing cargo via intravenous injection[30-33]. As demonstrated by our previous studies, our hydrogel-based standard design of nanoprobes are biocompatible and bio-eliminable[34, 35],

benefiting potential translation into clinic. As stated, the nanoparticle matrix not only serves as a vehicle for delivery but also prevents SNARF-5F interference with/by body proteins or enzymes. Such interference would affect the optical properties of the pH indicators and thus invalidate the pH calibration. Furthermore, by imaging a tumor with quadruple (i.e. four) laser wavelengths and then performing spectral unmixing, the contributions to the PA signals from the SNARF-PAA NPs and the two forms of hemoglobin (i.e. oxygenated hemoglobin and deoxygenated hemoglobin) can be separated. Thus, this method can provide truly quantitative and spatially resolved pH information in the tumor. At the same time, additional functional bits of information on tumor hemodynamic properties are also mapped, including the spatially distributed total hemoglobin concentration (i.e. blood volume) and the hemoglobin oxygen saturation (i.e. blood oxygenation).

2.2 Results

SNARF-5F incorporated polyacrylamide pH-sensing nanoparticles

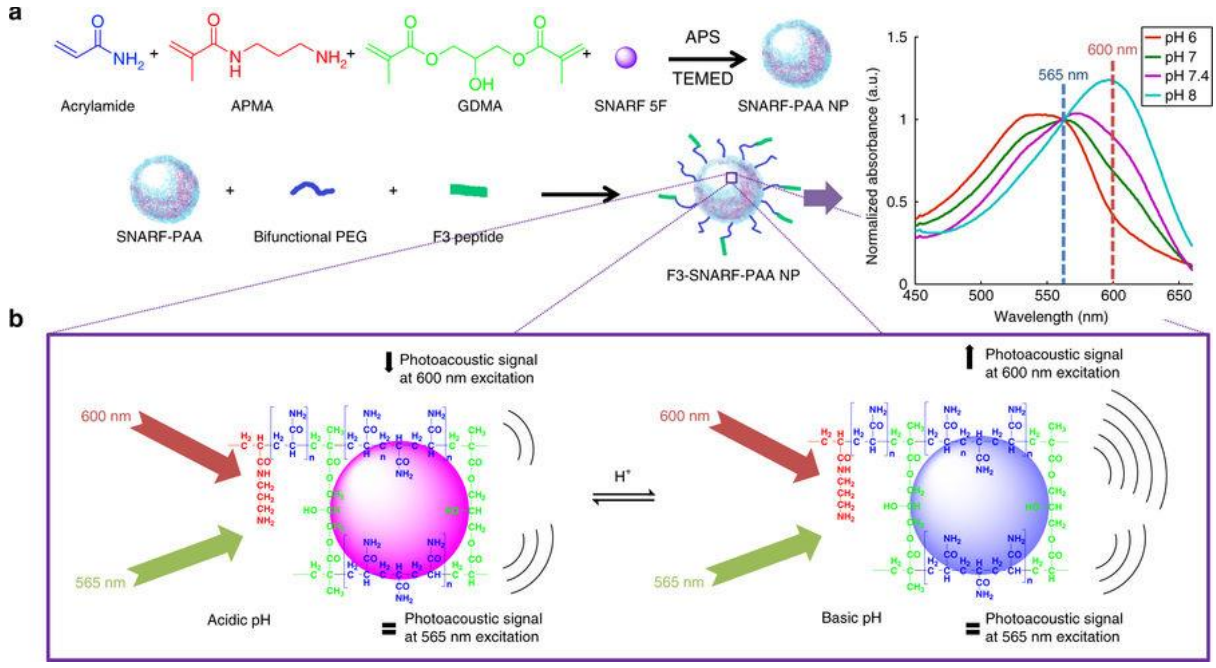

Figure 2.1 SNARF-5F encapsulated polyacrylamide based nanoparticle (NP) synthesis and pH-sensing scheme. (a) Two-step synthesis schematic of SNARF-5F encapsulated acrylamide-based NP. The surface of the SNARF-PAA NP is modified with polyethylene glycol, for immune system avoidance, and with the tumor-homing F3 peptides. The normalized optical absorption spectra at different pH levels indicate the SNARF-PAA NP's capability of pH sensing. The absorption at 565 nm, i.e., the isosbestic point, can be used as an internal reference point. The absorption at 600 nm can be used as a sensing point, which responds to difference in pH level. (b) PA pH-sensing scheme. The PA signal increases linearly with the optical absorption of NPs. Thus, the PA signal amplitude at 600 nm changes as the environmental pH changes; while the PA signal amplitude at 565 nm remains unchanged, acting as an internal reference signal.

As shown in the normalized optical absorption spectra (**Figure 2.1a**), measured by a UV-VIS spectrometer, the spectroscopic absorption of SNARF-PAA NPs varies with the pH level. The absorption at 565 nm presents an isosbestic point (i.e. the pH independent point). The isosbestic point can serve as the internal standard without need for a secondary reference probe. The ratio

between the intensity at another optical wavelength, such as 600 nm, and that of the isosbestic point correlates with the pH level. The 600 nm is picked because the optical absorption of SNARF-PAA NP at this wavelength has a large dynamic range when pH changes from 6 to 8. The selection of this wavelength can lead to better sensitivity in pH measurement.

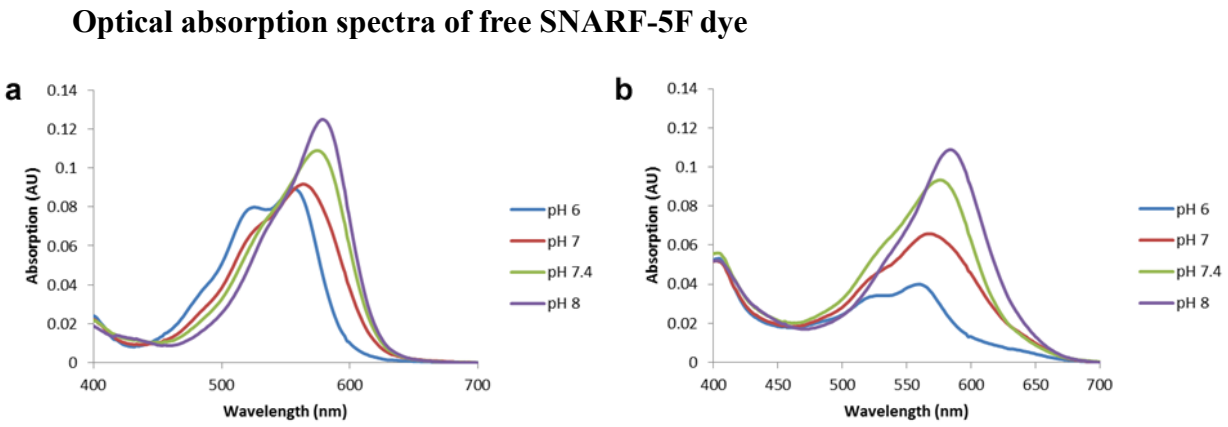

Figure 2.2 (a) pH-dependent optical absorption spectrum of SNARF-5F solution. (b) pH-dependent optical absorption spectra of SNARF-5F solution mixed with human serum albumin (4mg ml^{-1}).

The optical absorption spectrum of free SNARF-5F dye as a function of pH level is shown in **Figure 2.2a**. Similar to its emission spectrum which undergoes a pH-dependent wavelength shift, the absorption spectrum of SNARF-5F also changes with pH. When human serum albumin was added in the SNARF-5F solution, the interaction between SNARF-5F dye and proteins can change the optical absorption spectra of the dye, as shown in **Figure 2.2b**.

Characterization of SNARF-PAA NP

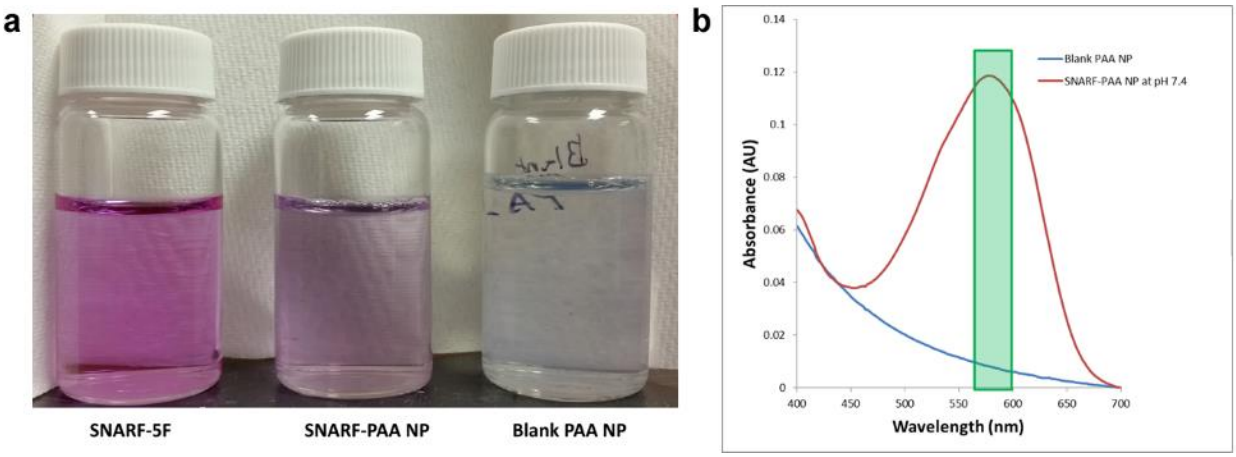

Figure 2.3 (a) Photo showing SNARF-5F, SNARF-PAA NP, and blank PAA NP solution (2mg ml^{-1} or equivalent dye concentration in PBS pH 7.4). (b) UV-VIS spectra of blank PAA NPs and SNARF-PAA NPs at equal concentration (2 mg ml^{-1}). The green rectangle indicates the range of the optical wavelengths (i.e. 565-600 nm) for quad-wavelength ratiometric PAI of tumor pH.

The blank PAA NP solutions are optically clear in the visible spectrum, as shown in the photograph in **Figure 2.3a** in comparison with the PAA NPs containing SNARF-5F. As checked by the UV-VIS spectrometer, the optical spectrum of blank PAA NP solution is significantly weaker than that of SNARF-PAA NPs in the wavelength range of 565-600 nm, as shown in **Figure 2.3b**. This weak spectrum of blank PAA NPs measured by the UV-VIS, instead of reflecting their optical absorption, should mostly come from their optical scattering of the lower wavelength light.

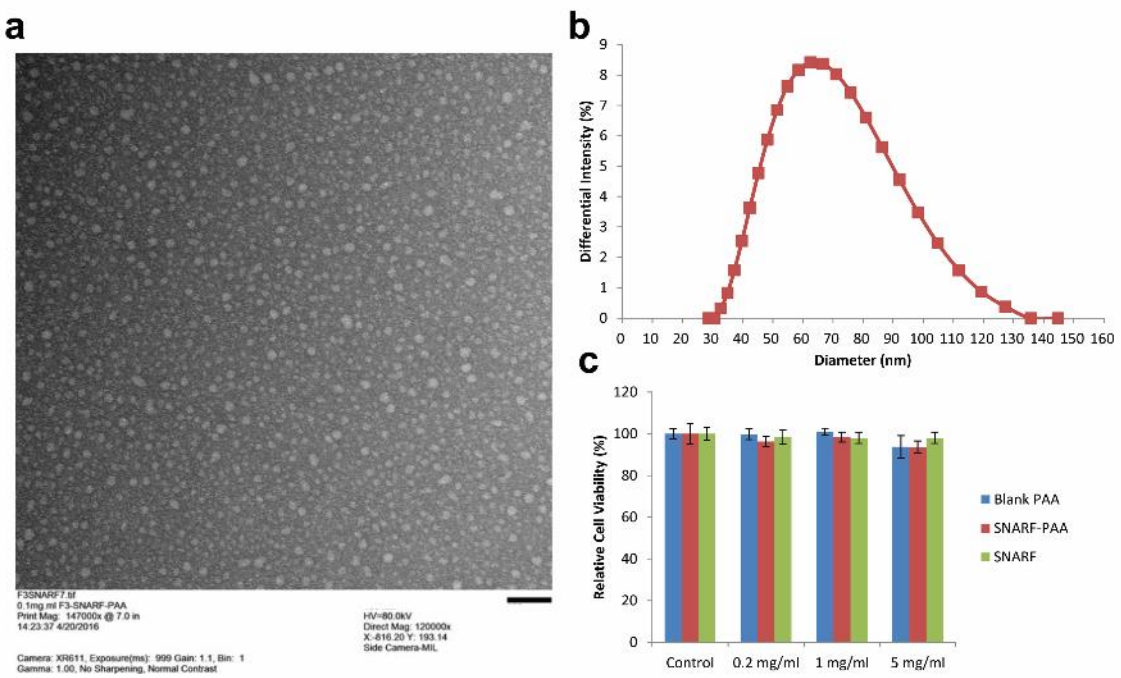

Figure 2.4 SNARF-PAA NP size and toxicity characterizations. (a) Transmission Electron Microscopy image of SNARF-PAA NPs. Scale bar, 100 nm (b) Hydrodynamic size measurements of SNARF-PAA NPs using Dynamic Light Scattering. (c) *In vitro* cytotoxicity test of free SNARF-5F dye, blank PAA NPs, and SNARF-PAA NPs. The relative cell viability was calculated for averages and standard error (n=3). The concentration marked was based on SNARF-PAA NP concentration. The concentration of SNARF-5F dye is equivalent to that loaded in SNARF-PAA NPs.

A Philips CM-100 transmission electron microscope (TEM) was used for dried size determination by negative staining using uranyl acetate. A Dynamic Light Scattering instrument (DLS, Delsa Nano C particle analyzer instrument, Beckman Coulter) was used to determine the hydrodynamic particle size and zeta potential. The hydrodynamic size of surface modified SNARF-PAA NP was ~60 nm (optimum for passive targeting towards tumor); while the dehydrated NP size was ~17 nm (**Figures 2.4a and 2.4b**). The sizes of naked SNARF-PAA NPs did not differ significantly from surface modified SNARF-PAA NPs. Zeta potential (surface charge) dropped from 26±2.3 mV to 17±1.2 mV as a result of surface modification. The zeta

potential was slightly reduced because of the PEGylated surface.

To test the cytotoxicity, 9L rat glioma cell line (American Type Culture Collection) was cultured in RPMI 1640 medium supplemented with 10% Fetal Bovine Serum (FBS) and 1% Antibiotic-antimycotic. Approximately 10,000 cells were seeded on 96 well plates. SNARF-5F, blank PAA NPs, and SNARF-PAA NPs were dissolved in the culture medium (20 mg ml^{-1}). The concentration of free SNARF-5F solution was equivalent to that loaded in SNARF-PAA NPs. Appropriate amounts of SNARF-5F, blank PAA NPs, or SNARF-PAA NPs were added and diluted with fresh culture medium to make final concentrations of 0.2 mg ml^{-1}, 1 mg ml^{-1}, and 5 mg ml^{-1} in each well. Wells that contained cells without being treated with SNARF-5F or SNARF-PAA NPs served as the control. After overnight incubation, the culture medium in each well were carefully removed and replaced with 100 μL of colourless RPMI. Then, 20 μL of (3-(4,5-Dimethylthiazol-2-yl)-2,5-Diphenyltetrazolium Bromide) (MTT) (5 mg ml^{-1}) was added into each well and incubated at 37^{o}C for 4 hours. In order to dissolve insoluble MTT formazan product, 100 μL of DMSO was added into each well and placed at room temperature for 2 hours. The cell viability was analyzed, by measuring absorbance at 590 nm (reference 620 nm), by an Anthos 2010 Microplate Absorbance Reader (Biochrom Ltd.) (n=3). The MTT assay result (**Figure 2.4c**) demonstrates that none of free SNARF-5F, blank PAA NPs, or SNARF-PAA NPs exhibits any significant cytotoxicity at the concentrations tested.

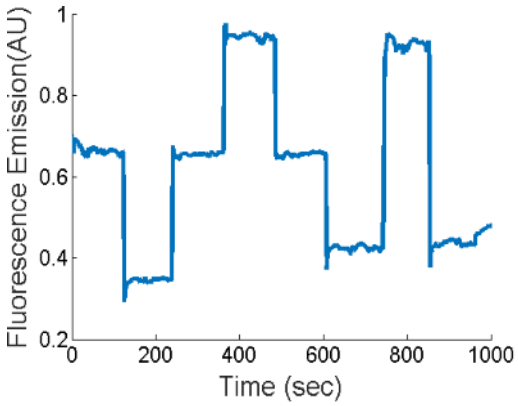

Figure 2.5 Time-dependent fluorescence measurement (540 nm ex/580 nm em) demonstrating the kinetics of SNARF-PAA NPs in sensing the environmental pH change.

Based on our former studies, the response time of our PAA NP based nanosensors can vary, depending on the nanoparticle composition and matrix[36]. To study the kinetic response of our SNARF-PAA NPs to the change of environmental pH level, we have conducted a time-dependent fluorescence measurement taken by Horiba Fluoromax-3. The fluorescence measurement of a SNARF-PAA NP solution (540 nm ex/580 nm em) was continuously taken (once every second) over a period of 1000 seconds. During the measurement, the solution was kept stirred using magnetic stirrer equipped within the fluorometer. To change the pH level in the solution, small volumes of 1M HCl or 1M NaOH were added alternatively (setting the solution at pH 6, pH 7 or pH 8). As shown in **Figure 2.5**, the fluorescence measurement as a function of time demonstrated fast optical response of the SNARF-PAA NPs to the pH change in the solution medium. The fluorescent signal from the SNARF-PAA NPs responded within 1 second after adding of either HCl or NaOH, and stabilized in a few seconds. The time needed for signal stabilization is due to the limited stirring speed. This result, besides validating the quick kinetics of the SNARF-PAA NPs, also confirmed their reversibility in sensing the pH level.

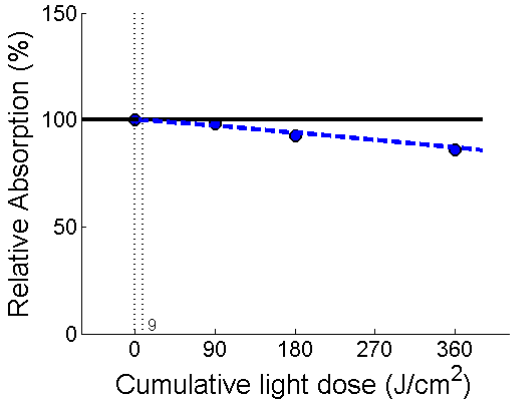

Figure 2.6 Photostability of SNARF-PAA NPs. The optical absorption of SNARF-PAA NP solution (2mg ml^{-1} in PBS pH 7.4) was measured at different time points during a total period of 60 min when the solution was continuously illuminated with 565 nm laser beam with homogeneous light fluence of 10 mJ cm^{-2}. The relative absorption of the solution is presented as a function of the cumulative light dose.

To study the photostability, a SNARF-PAA NP solution (2mg ml^{-1}, in PBS pH 7.4) was continuously illuminated with a laser beam at 565-nm wavelength and 10 mJ cm^{-2} light fluence over a total time period of 60 minutes. The optical absorption of the solution at different time points (i.e. 15 min, 30 min, and 60 min) was measured by the UV-VIS spectrometer. The relative percentage change in optical absorption was used to study the photobleaching. Although it has been known that SNARF-5F can be photobleached, the photostability of the SNARF-PAA NPs, as demonstrated by **Figure 2.6**, is satisfactory. At 15 min after illumination (accumulated light dose 90 J cm^{-2}), the change in optical absorption is about 2% which further increased to about 10% at 60 min (accumulated light dose 360 J cm^{-2}). This slow speed of photobleaching is highly desirable for potential *in vivo* applications. Using our current system, quad-wavelength ratiometric PAI of a tumor takes less than 1 minute for image acquisition at all the four wavelengths. The estimated photobleaching during this time period is less than 0.2%.

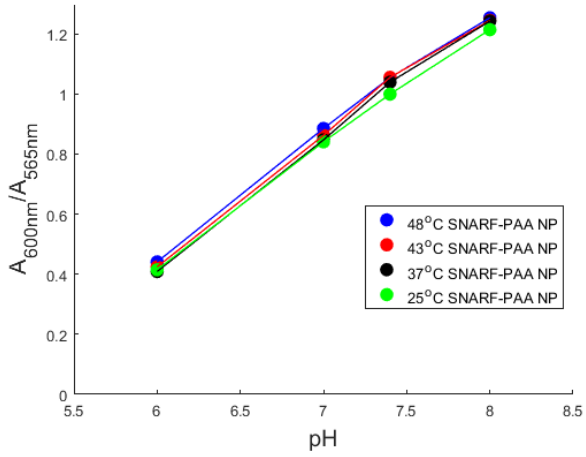

Figure 2.7 Calibration curves of SNARF-PAA NPs at different temperatures.

To study the potential change of the optical absorption spectrum of SNARF-PAA NPs with temperature, we have generated calibration curves at different temperatures, including 25°C (room temperature), 37°C (body temperature), 43°C, and 48°C. Each calibration curve reflects the ratio between the absorbance at 600 nm and 565 nm (i.e. A_{600nm}/A_{565nm}) as a function of the pH level. As shown in **Figure 2.7**, there is no obvious difference among the calibration curves at different temperatures, demonstrating good temperature stability of SNARF-PAA NPs.

Nanosensor vs. Molecular sensor

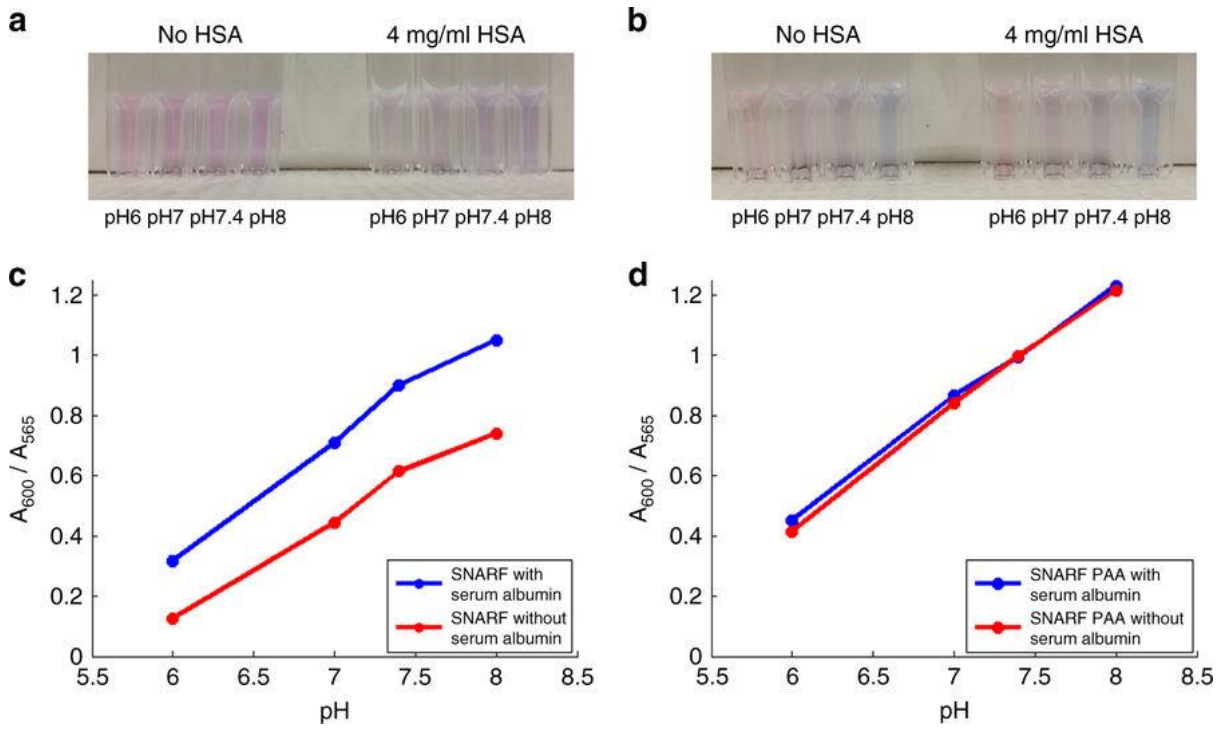

Figure 2.8 The different interactions of free SNARF-5F and SNARF-PAA NP with human serum albumin (HSA). (a) Direct observations of the free SNARF-5F buffered at different pH of 6, 7, 7.4 and 8. The differences in color can be seen for solutions with and without HSA (4 mg ml^{-1}). (b) Direct observations of SNARF-PAA NPs buffered at different pH of 6.0, 7.0, 7.4 and 8.0. No obvious difference in color can be seen for solutions with and without HSA (4 mg ml^{-1}). (c) pH calibration curves (absorbance at 600 nm divided by absorbance at 565 nm) of free SNARF-5F with (*blue*) and without (*red*) HSA. Significant changes caused by the interaction of SNARF-5F with HSA can be noticed. (d) pH calibration curves of SNARF-PAA NPs with (*blue*) and without (*red*) HSA. No noticeable changes can be noticed, demonstrating the advantages of having the dye encapsulated in the PAA matrix.

In the dye's free form without being protected by nanoparticles, the SNARF-5F can interact with the large proteins in the bloodstream (such as serum albumin). The direct interaction between SNARF-5F and proteins can change the optical properties of the dye and thus affect its pH sensing capability, as demonstrated in **Figure 2.2**[29]. The use of nanoparticles can overcome this problem and stabilize the optical properties of the dye *in vivo*. The PAA matrix, which allows

penetration of water and ions but not of protein molecules, essentially protects the dye molecules from the environment, preventing them from directly interacting with the proteins. To demonstrate this improvement, we modeled the interaction of SNARF-5F and SNARF-PAA NP with human serum albumin (HSA). The serum albumin is the most abundant protein found in the bloodstream, typically ranging from 3mg ml^{-1} to 5mg ml^{-1} [37]. The HSA (4mg ml^{-1}) was added to either SNARF-5F free dye or SNARF-PAA NPs in solutions buffered at pH 6, pH 7, pH 7.4 or pH 8. The photographs in **Figure 2.8a** show the color changes of free SNARF-5F after adding of HSA; while no obvious color change can be noticed for SNARF-PAA NPs after adding of HSA, as shown by the photographs in **Figure 2.8b**. The calibration curves (i.e. the optical absorption ratios between 600 nm and 565 nm at different pH levels) with and without the appearance of HSA were shown in **Figure 2.8c and Figure 2.8d**, respectively, for free SNARF-5F and SNARF-PAA NPs. We can clearly see the change in the calibration curve of the free SNARF-5F caused by HSA; while the calibration curve of the SNARF-PAA NPs was unaffected after the adding of HSA. This study suggested that, compared to free SNARF-5F, SNARF-PAA NP is a better choice for *in vivo* applications where the appearance of proteins cannot be avoided.

Dual-wavelength ratiometric PAI of pH

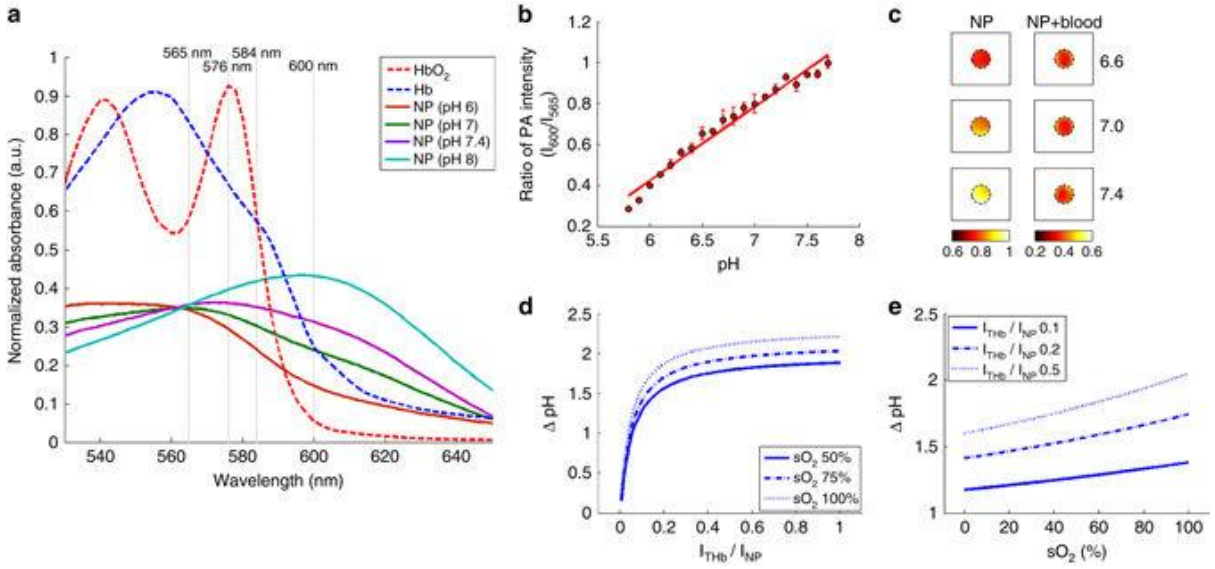

Figure 2.9 Limitation of dual-wavelength ratiometric photoacoustic imaging of pH. (a) Spectroscopic optical absorption of oxygenated hemoglobin (HbO_2), deoxygenated hemoglobin (Hb) and SNARF-PAA NPs at different pH levels. (b) Measured PA signal amplitude ratios between the two wavelengths (600 nm/565 nm) as a function of pH (pH 5.8–7.8 with 0.1 pH interval) ($n = 3$, error bars represent standard deviations). By performing a linear fitting of the scattered measurements in the range of pH 5.8–7.8, a calibration line was generated. (c) The PA ratiometric images (600 nm/565 nm) of phantoms containing SNARF-PAA NPs buffered at pH 6.6, 7.0 and 7.4, respectively. The nanoparticle (NP) images are for phantoms with NPs and the NP + blood images are for phantoms with NPs containing blood (1% w/w). The color scale represents the ratio between the PA intensities at the two wavelengths (600 nm/565 nm). (d) Estimated errors (i.e., ΔpH) in dual-wavelength ratiometric PA pH measurement as a function of the ratio between the PA signal amplitudes from total hemoglobin (THb) and SNARF-PAA NPs (i.e., I_{THb}/I_{NP}). The three curves are for three different hemoglobin oxygen saturation (sO_2) levels (50, 75 and 100%). (e) Estimated errors (i.e., ΔpH) in dual-wavelength ratiometric PA pH measurement as a function of the blood sO_2. The three curves are for three different ratios of I_{THb}/I_{NP} (0.1, 0.2 and 0.5). PA imaging processing and analyses were performed by Dr. Janggun Jo.

Figure 2.9a shows the optical absorption spectra of SNARF-PAA NPs at different pH levels.

The optical absorption spectra of oxygenated hemoglobin (HbO_2) and deoxygenated hemoglobin

(Hb), the major two types of hemoglobin in blood, are also presented. Assuming that the pH sensing dye is the only chromophore in the target tissue, ratiometric PA measurements at two laser wavelengths are sufficient for quantifying pH level. Although this assumption has been adopted by many previous studies including ours[29], it cannot stand in most circumstances when the optical absorption from background tissue cannot be ignored. In the visible to nearly infrared spectral region, the dominant chromophores in most biological tissues are hemoglobin. When hemoglobin also contributes to the PA signal, then ratiometric PAI using two laser wavelengths is not sufficient anymore for quantifying pH.

An experiment on phantoms was performed to demonstrate the challenges of ratiometric PA pH imaging based on two wavelengths. Before pH measurement, a calibration line for SNARF-PAA NP was first generated from pH 5.8 to pH 7.8, as shown in **Figure 2.9b**. This calibration line shows the PA intensity ratios between the two wavelengths (i.e. 600nm/565nm) at different pH levels. With this calibration line, any ratiometric PA measurement at the two wavelengths leads to a corresponding pH level. Phantoms were made of porcine gels containing SNARF-PAA NPs, and were buffered at different pH values (i.e. pH 6.6, pH 7.0, and pH 7.4). Each phantom was a long cylinder (1.6-mm diameter), and was imaged along the cross section. In one set of phantoms, no blood was added and, therefore, the SNARF-5F dye was the only optical absorber. In another set of phantoms, whole blood was mixed in each phantom with a concentration of 1% (w/w). Each phantom was imaged at the two laser wavelengths (565 nm and 600 nm). With the ratiometric measurements, the pixel-by-pixel pH levels in each phantom were calculated. As we can see, for phantoms containing no blood, their pH can be measured well by performing dual-wavelength ratiometric PAI, as shown in **Figure 2.9c**. However, for phantoms containing blood which also contributed to the PA signals, dual-wavelength ratiometric PAI was not able to

quantify their pH levels (**Figure 2.9c)**.

To understand how much the presence of blood in a target tissue can affect the dual-wavelength ratiometric PAI of pH, a theoretical simulation was conducted. The optical absorption of blood is contributed mainly by the two forms of hemoglobin, i.e. HbO_2 and Hb, which have different optical absorption spectra[38]. Therefore, not only the total hemoglobin concentration (THb) but also the hemoglobin oxygen saturation (sO_2) affects the spectroscopic PA signal amplitudes from a biological tissue. In simulation, the true pH level was set as 7.4. We estimated the errors in pH measurement (i.e. ΔpH) as functions of THb and hemoglobin sO_2. Since THb affects the ratiometric PA measurement by producing background PA signals, the relative contribution of THb is counted as I_{THb}/I_{NP} (i.e. the ratio between the PA signal amplitudes from THb and SNARF-PAA NP). As we can see in **Figure 2.9d** and **Figure 2.9e**, not only the presence of hemoglobin but also the hemoglobin sO_2 can strongly affect the accuracy in dual-wavelength ratiometric PAI of pH. The error can be large even when the THb is relatively low compared to SNARF-PAA NP. For example, even when I_{THb}/I_{NP} is lower than 0.1, meaning that the SNARF-PAA NP is still the major optical absorber, the ΔpH can be larger than 1. This result suggests that, without considering the impact of hemoglobin to spectroscopic PA measurement, quantifying the pH level in biological tissues *in vivo* is very difficult. For characterizing tumor microenvironment, this is especially challenging, as both the blood content and the blood oxygenation in cancer tumors are largely heterogeneous.

Quad-wavelength ratiometric PAI of pH

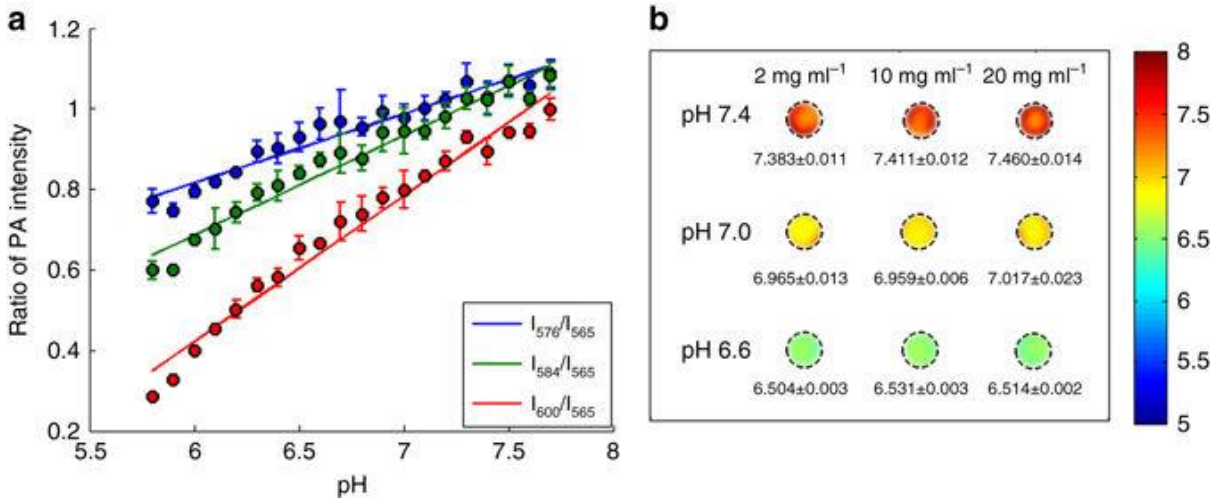

Figure 2.10 Quad-wavelength ratiometric PA pH imaging of phantoms. (a) Measured PA signal amplitude ratios between the three wavelengths and the isosbestic point (i.e., 576 nm/565 nm, 584 nm/565 nm, and 600 nm/565 nm) from pH 5.8–7.7 with 0.1 pH interval (n = 3, error bars represent standard deviations). By performing linear fittings of the scattered measurements in the range of pH 5.8–7.8, three calibration lines were generated. (b) Quantitative pH images of phantoms containing different concentrations (2, 10 and 20 mg ml^{-1}) of SNARF-PAA NPs buffered at different pH levels (pH 6.6, 7.0 and 7.4). The means and the standard deviations of the pH levels in each PA image were calculated. The measurement accuracy was better than 0.1 pH. The presence of whole blood (1%, w/w) did not affect the quantification of pH levels. PA imaging processing and analyses were performed by Dr. Janggun Jo.

To overcome the problem faced by dual-wavelength ratiometric PAI, quad-wavelength ratiometric PAI was developed, as described in detail in the Method section. By working with SNARF-PAA NPs buffered at different pH levels from pH 5.8 to pH 7.8, the PA amplitude ratios between the three wavelengths (576 nm, 584 nm, and 600 nm) and the isosbestic point (565 nm) were measured, as shown in **Figure 2.10a**. Each scattered point shows the average and the standard deviation of the measurements from three samples. The scattered PA measurements for the three wavelengths are linearly fitted, leading to three calibration lines, as marked by I_{576}/I_{565}, I_{584}/I_{565}, and I_{600}/I_{565}, respectively. The three calibration lines enable quantitative measurement of

the pH levels by performing quad-wavelength PAI. **Figure 2.10b** shows the imaging results from gel phantoms buffered at different pH levels (pH 6.6, pH 7.0, and pH 7.4). Although these phantoms were also mixed with whole blood at 1%, the quad-wavelength ratiometric PAI approach successfully quantified the pH levels in each phantom. In addition, no obvious difference can be seen when comparing the results from the three columns in **Figure 2.10b,** suggesting that the result from the quad-wavelength ratiometric PAI method is independent on the concentration of the SNARF-PAA NPs. This is extremely important for applications *in vivo*, as the local concentration of SNARF-PAA NPs in the target tissue is difficult to control, and could also be highly heterogeneous.

***In vivo* quad-wavelength ratiometric PAI of tumor**

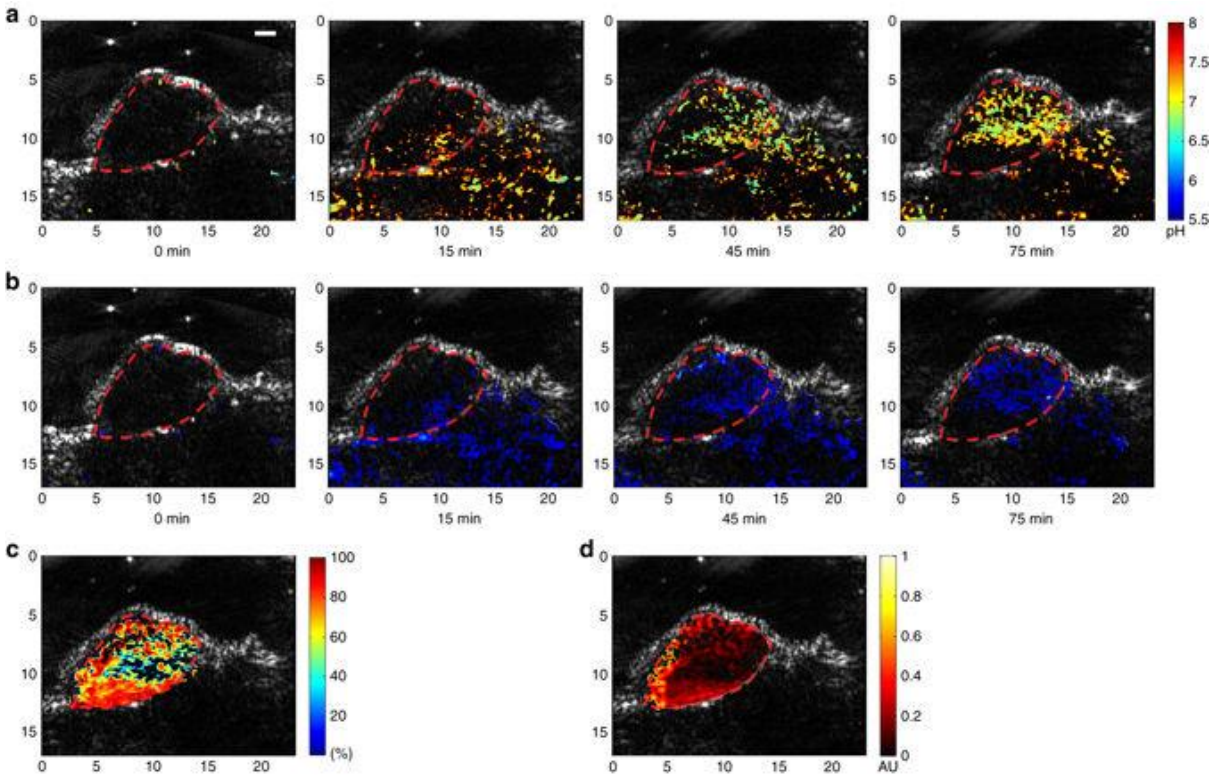

Figure 2.11 Example in vivo quad-wavelength ratiometric PAI of a tumor. Each PA functional image in pseudo-color is superimposed on the gray-scale US image. The tumor area is marked by the dashed line in each image. (a) Quantitative PA pH images at different time points after SNARF-PAA NP injection. *Scale bar*, 2 mm. (b) PA images showing the distributions of SNARF-PAA NPs at different time points after injection. (c) PA image showing the spatially distributed hemoglobin oxygen saturation (sO_2) in the tumor area at 75 min after injection. (d) PA image showing the spatially distributed total hemoglobin concentration (THb) in the tumor area at 75 min after injection. PA imaging processing and analyses were performed by Dr. Janggun Jo.

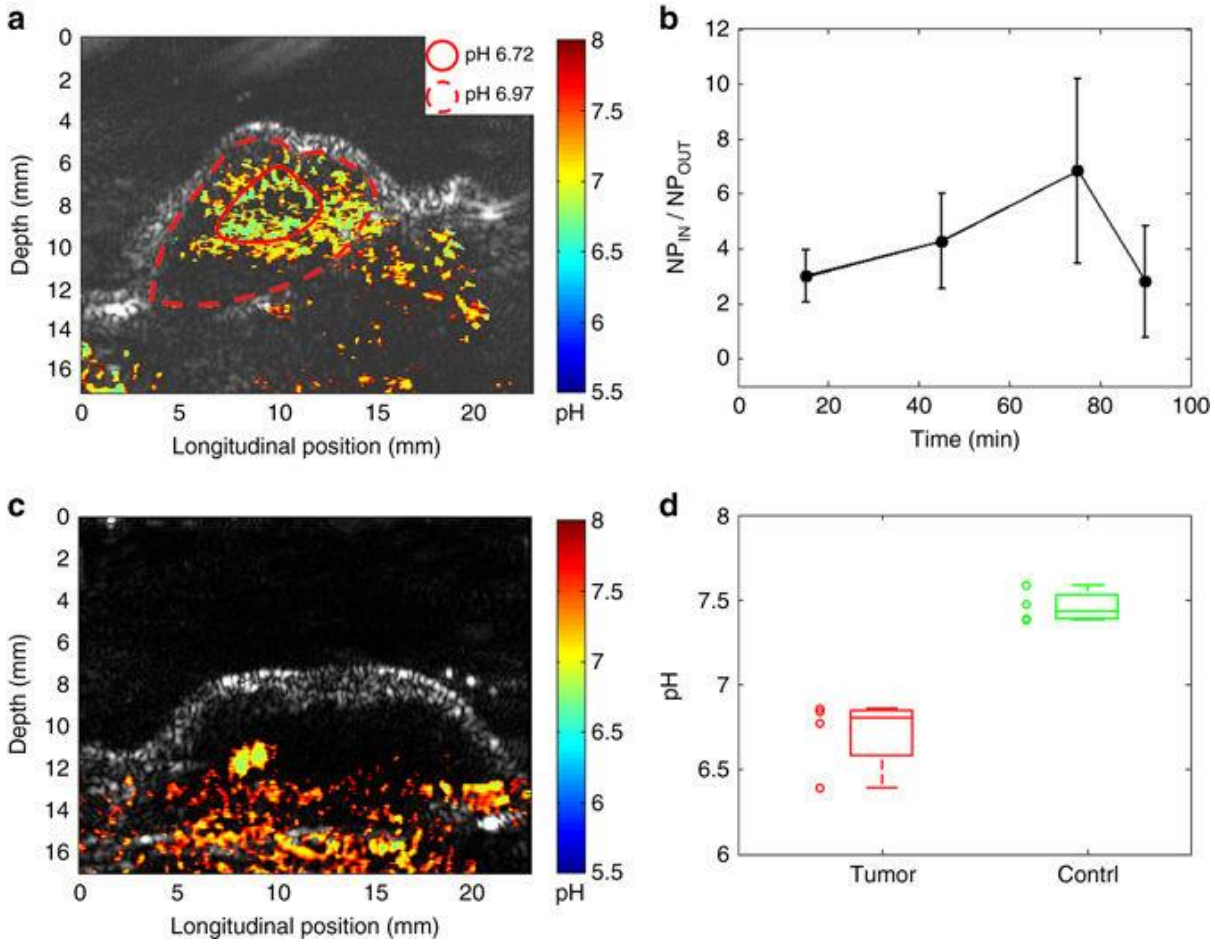

Figure 2.12 Statistical analyses of the PAI results from the in vivo mouse model. (a) A close-up view of the PA pH image of a tumor shown in Figure 2.11 (75 min). The pH in the center area (i.e., the area in the solid line) and the peripheral areas (i.e., the area between the solid line and the dash line) are averaged respectively. (b) Analysis of the SNARF-PAA NP accumulation in the tumors at different time points after systemic injection represented by the ratio between the NP concentrations inside and outside the tumor (NP_{IN}/NP_{OUT}). With the measurements from four animals ($n = 4$), the average and the standard error for each time point are presented. (c) Example PA pH image of a normal tissue (i.e., thigh), showing relatively higher pH. (d) The boxplot showing the pH levels in tumors ($n = 4$) vs. the pH levels in normal tissues (i.e., thigh) ($n = 4$), as quantified from PA pH images. The measurements from individual sample (tumors and thighs) are also presented by scattered points. PA imaging processing and analyses were performed by Dr. Janggun Jo.

An example of time-dependent functional imaging result of a subcutaneous tumor is shown in **Figure 2.11**. Each PA functional image is super-imposed on the gray-scale US image acquired at the same time using the same acquisition system. Naturally co-registered with the PA image, the US image works well in delineating the tissue structures including the tumor boundary (as marked by the dash line in each image). The PA images in the first line show the spatially distributed SNARF-PAA NPs in the imaged B-scan section at different time points after systemic administration. The NPs were preferentially accumulated in the tumor area gradually, which, we believe, is a combined result of the enhanced permeability and retention (EPR) effect and the tumor homing F3 peptides. The totally amount NP in the tumor reached a peak at around 75 minutes after injection. The second line in **Figure 2.11** shows the spatially distributed pH levels in the imaged section at different time points after injection. By looking at the pH image at 75 minutes, we can notice that the pH at the center area of the tumor was a little lower than the pH at the peripheral area of the tumor. A close view of this pH image at 75 minutes is shown again in **Figure 2.12a**, where the two red lines (solid and dash) marked the center area and the peripheral area of the tumor, respectively. The quantitative measurements demonstrate that the averaged pH level in the area within the solid line is 6.72 ± 0.29, while the average pH level in the area between the solid line and the dash line is 6.97 ± 0.35.

By performing quad-wavelength ratiometric PAI, we also quantified the spatially distributed hemoglobin oxygen saturation (i.e. blood sO_2) and the spatially distributed total hemoglobin concentration (i.e. THb) within the marked tumor area, as shown in **Figure 2.11c** and **Figure 2.11d**, respectively. The quantified blood sO_2 image at 75 minutes shows that the center of the tumor area had lower blood sO_2 compared to the peripheral area, matching our expectation for tumor hypoxia. The THb image at 75 minutes shows that the center of the tumor also had

relatively lower blood content. This example imaging result demonstrates that, by performing quad-wavelength ratiometric PAI, important functional parameters describing the tumor microenvironment, including acidosis and hypoxia, can be quantitatively mapped at the same time.

With the results from four animals, the targeted delivery of SNARF-PAA NPs to the tumors after systemic administration was further evaluated. With a pseudo-color PA image showing the distribution of NPs (e.g. the images in **Figure 2.11a**), the average NP concentration in an area can be computed by the number of color pixels divided by the total number of pixels. The accumulation of NPs in a tumor can be evaluated by the ratio between the NP concentrations inside and outside the tumor (i.e. NP_{IN}/NP_{OUT}). A larger ratio suggests better targeted delivery. As the result shown in **Figure 2.12b**, the largest ratio appears at 75 minutes after injection, confirming again that the concentrations of NPs in the tumors reached a peak at this time point. After the imaging experiment, animal was euthanized, and the accumulations of SNARF-PAA NPs in different organs were studied *ex vivo*.

An example PA pH image of a thigh is shown in **Figure 2.12c** which was acquired using the same method for tumor imaging. Compared to the pH images from the tumors, as the example in **Figure 2.12a**, the images from the thighs as normal controls show pH levels that are neutral (around pH 7.4). The average pH levels in the tumor areas and in the normal thigh muscles from four mice were examined (n=4), as shown by the boxplot in **Figure 2.12d**. The average pH in the thigh muscles was 7.46±0.095 while the average pH in the tumors was 6.71±0.22. A t-test was performed with a hypothesis that the pH quantified by the quad-wavelength PA ratiometric imaging cannot differentiate the tumors and the normal thigh muscles. A $P<0.001$ was reached,

suggesting that the pH values in the tumors measured by PAI were significantly different from those in the controls. The imaging finding was confirmed by the measurements from a micro pH electrode (STAR A221, Fisher Scientific, Hampton, NH) as the gold standard. The readings from the electrode placed at multiple positions in the tumors were in the range of pH 6.4-7; while the readings from the electrode placed at multiple positions in the thigh muscles were in the range of pH 7.2-7.5.

SNARF-PAA NP accumulations in organs and tumors

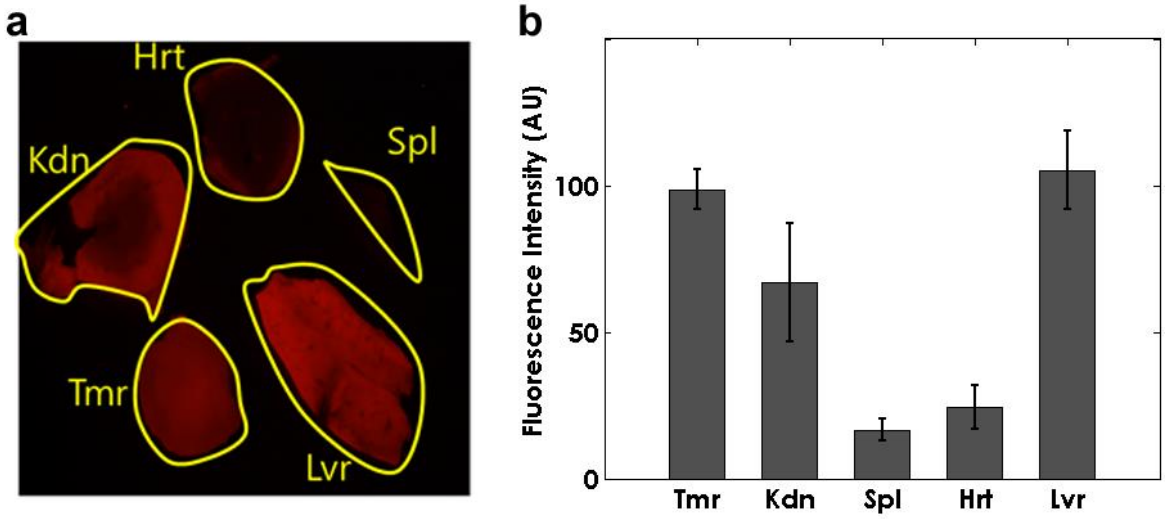

Figure 2.13 Organ accumulations of SNARF-PAA NPs. (a) Fluorescence image (ex 560 nm/em 630 nm) showing SNARF-PAA NPs accumulated in the major organs and the tumor dissected from a mouse. (b) Quantified fluorescence intensities were compansted with the intensity of tumor and calculated for averages and standard deviations in different tissues (n=3). Tmr: tumor, Kdn: kidney, Spl: spleen, Hrt: heart, and Lvr: liver.

The SNARF-PAA NP's accumulations in organs were studied on a mouse model. As soon as the last sets of images were taken, the mice were sacrificed. Then, the organs and the tumor

tissues were isolated and kept in 10% buffered formalin acetate solution for 24 hrs. The tissues were dissected into thin slices and the fluorescence images (ex 560 nm/em 630 nm) were taken using Leica DMIRB inverted fluorescence microscope. The fluorescence intensities were quantified using MATLAB. As shown in **Figure 2.13**, SNARF-PAA NPs were mostly accumulated in the tumors and the livers. The liver accumulation is common for intravenously injected nanoparticles that are 50-100 nm in size.

Error in pH quantification due to optical attenuation

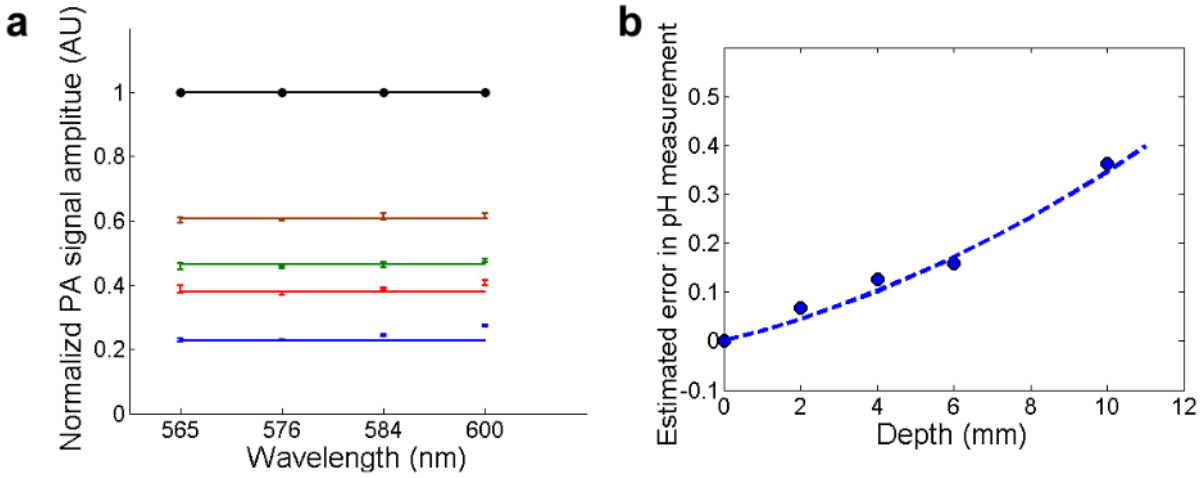

Figure 2.14 Error in pH quantification due to the spectroscopic difference in optical attenuation in tissue. (a) At different depths (2, 4, 6, and 10 mm), the PA signal amplitudes at the four wavelengths for ratiometric PAI are normalized to the measurements at depth=0 (when the object was not covered by any tissue). The spectroscopic differences in the normalized PA signal amplitudes become larger when the image depth increases. (b) The estimated error in pH quantified by ratiometric PAI as a function of the imaging depth. This error in pH measurement as a result of the wavelength-dependent optical attenuation increases with the imaging depth. The dash line shows the result of Gaussian fitting.

We estimated the potential error in pH quantification due to the optical attenuation at

different wavelengths for quad-wavelength PA ratiometric imaging. A line target (a black mental wire) was covered by slices of chicken breast tissue with different thicknesses (depths=2 mm, 4 mm, 6mm, and 10 mm, respectively), and measured at the four wavelengths (i.e. 565 nm, 576 nm, 584 nm, and 600 nm). The PA signal amplitude at each wavelength was then normalized respectively by the signal amplitude acquired from the target without being covered (i.e. depth=0), as shown in **Figure 2.14a**. At 2 mm or 4 mm depth, the difference among the normalized PA signal amplitudes at the four wavelengths were small (<1%). At 6 mm depth which was the maximum tumor depth for the animal model involved in this study, the normalized PA signal amplitudes at 600 nm and 565 nm showed a difference of 4.8% as a result of the wavelength-dependent optical attenuation. Without compensating this 4.8% difference, the estimated error in pH quantification based on ratiometric PAI is 0.16 pH. When tissue depth was further increased to 10 mm, a larger difference of 10% was observed between the normalized PA signal amplitudes at 600 nm and 565 nm. Without compensating this 10% difference, the estimated error in PA pH imaging is 0.34 pH. **Figure 2.14b** shows the estimated error in pH measurement as a function of the imaging depth. As expected, the error becomes larger when the imaging depth increases. This error in pH quantification due to the spectroscopic difference in optical attenuation in tissue can potentially be compensated by considering the optical fluence in the simulation for quad-wavelength ratiometric PAI.

Sensitivity of PAI of SNARF-PAA NPs

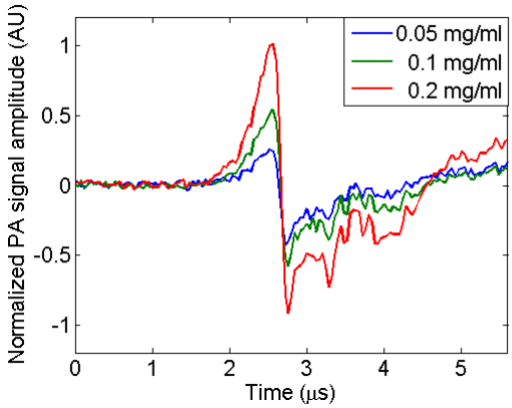

Figure 2.15 PA signals of SNARF-PAA NP solutions embedded 6-mm deep in optically scattering tissue. The signals correspondent to different NP concentrations (0.2 mg ml^{-1}, 0.1 mg ml^{-1}, and 0.05 mg ml^{-1}) can all be detected with good signal-to-noise ratio.

An experiment has been conducted to assess the sensitivity limit of PA imaging in detecting the SNARF-PAA NPs in subsurface tissue. The SNARF-PAA NP solutions (in PBS pH 7.4) were placed in an optically transparent tube (1.8 mm inner diameter) which was covered by a slab of 6-mm thick chicken breast tissue. The surface of the chicken breast was illuminated with a homogenous light beam with light fluence of 20 mJ cm^{-2} at 565-nm wavelength. The SNARF-PAA NP solutions were diluted to different concentrations, including 0.05 mg ml^{-1}, 0.1 mg ml^{-1}, and 0.2 mg ml^{-1}. The PA signals detected from the NP solutions are shown in **Figure 2.15**. At even very low concentration of 0.05 mg ml^{-1} which is 400 times dilution of the injection concentration, the NP solution was still detectable with a good signal-to-noise ratio over 20 dB. 400 times of dilution was decided because we estimated that the tumor volume was around 1/400 of the mouse body and assumed SNARF-PAA NPs were uniformly distributed in the body. Considering the preferential accumulation of the NPs in the tumor due to both enhanced permeability and retention (EPR) effect and the active tumor targeting moiety, the actually NP

concentrations in the mouse tumors *in vivo* should be higher.

Hemoglobin oxygen saturation (sO_2) images before the injection of SNARF-PAA NPs

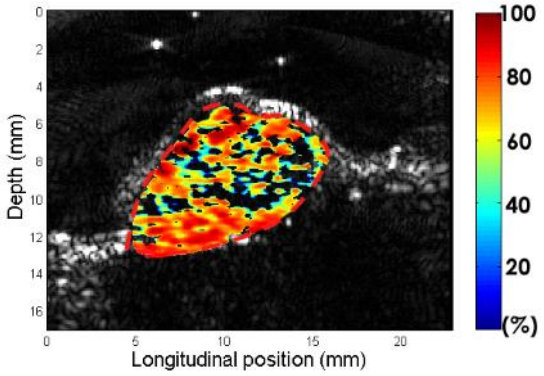

Figure 2.16 PA hemoglobin oxygen saturation (sO_2) image in the tumor *in vivo* before the injection of SNARF-PAA NPs. PA imaging processing and analyses were performed by Dr. Janggun Jo.

The quad-wavelength PA ratiometric imaging provided hemodynamic functional imaging including both hemoglobin oxygen saturation (sO_2) and total hemoglobin concentration (THb) at the same time of pH imaging, as shown in **Figure 2.11c and 2.11d**. We also studied the sO_2 image of the same tumor at 0 min (i.e. before the injection of SNARF-PAA NPs), as shown in **Figure 2.16**. This image at 0 min shows similar sO_2 level as the image acquired at 75 minutes. The center area of the tumor also has relatively low oxygen saturation.

Quad-wavelength ratiometric calibration of the PAI system

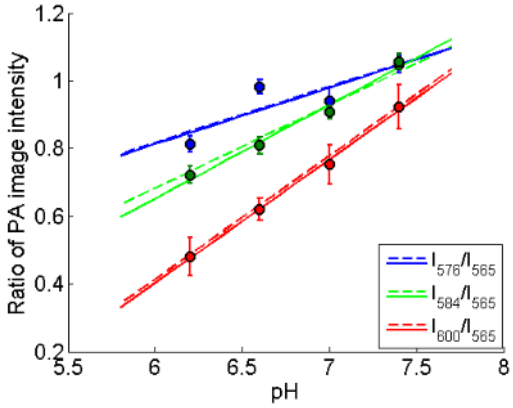

Figure 2.17 Quad-wavelength ratiometric calibration lines measured by the PAI system built on the Verasonics platform. The solid lines (i.e. 576 nm/565 nm, 584 nm/565 nm, and 600 nm/565 nm) are the linear fittings of the measurements at four different pH levels (i.e. pH 6.2, pH 6.6, pH 7, and pH 7.4). The dashed lines are the results from the V312 transducer (Figure 2.10a) for comparison. The points show the averages of image intensity ratios with standard deviations (n=50).

Gel phantoms (1.6-mm cylinders) contained SNARF-PAA NPs (concentration 10 mg ml^{-1}) at different pH buffers (i.e. pH 6.2, pH 6.6, pH 7, and pH 7.4) were made. Each phantom was imaged along the cross section using the PAI system built on the Verasonics US platform at the four wavelengths (565 nm, 576 nm, 584 nm, and 600 nm). For the PA image at each wavelength, the pixel intensities in the phantom were averaged. The average PA image intensities at the three wavelengths (576 nm, 584 nm and 600 nm) were divided by the average PA image intensity at the isosbestic point (565 nm). For each ratiometric measurement at each pH level, the measurements from 50 images were averages and the standard deviation was calculated, as shown in **Figure 2.17**. Linear fittings of the measurements at the four pH levels were conducted, and the resulted calibration lines (i.e. 576 nm/565 nm, 584 nm/565 nm, and 600 nm/565 nm) were compared to those from the V312 transducer. The calibration lines from the two systems are similar.

2.3 Discussion

Although the importance of pH in biological tissue, especially with respect to tumor acidosis, has been noted for many decades, we still lack a practical method for imaging and non-invasively quantifying pH in biological samples *in vivo*. Here we presented a nanoparticle assisted, non-invasive, and *in vivo* PAI technique for quantitative pH imaging of subsurface solid tumors *in vivo* based on optical spectroscopy. The PA pH nanosensors were fabricated by encapsulating the SNARF-5F dye in the PAA NPs. The nanoparticle matrix serves a critical role in chemical imaging *in vivo*, protecting the sensing dye molecules from direct interactions with interfering proteins or enzymes as well as enabling specific targeting of tumor cells. For instance, direct interaction with albumin can significantly influence an indicator dye molecule's optical characteristics and reduce its pH sensing capability. The experimental results from the phantoms and the animal model demonstrated that quad-wavelength ratiometric PAI allows a differentiation of the optical spectra of hemoglobin and pH-dependent SNARF-PAA NPs. As a result, quantitative imaging of pH without being affected by the background light absorption in biological tissues becomes possible. In addition, the quantification of pH is unaffected by the variation in the SNARF-PAA NP concentration. All these features are crucial for practical applications of the technique *in vivo*. At the same time, for pH imaging, the quad-wavelength PAI also allows quantitative evaluation of tumor hemodynamic properties, including blood volume and blood oxygenation.

In this study, we assumed that the major chromophores in the target biological samples are the two forms of hemoglobin, which is true in the spectral region of 565-600 nm. In the future, when other chromophores may be present in the target tissue, imaging at additional wavelengths will be needed. However, the number of wavelengths scanned by for PAI is related to the cost of

the imaging system as well as the imaging speed. Currently, using a single tunable laser as the light source, the switching between laser wavelengths limits the imaging speed. When a multi-wavelength light source (e.g. a system working with multiple lasers each firing at different wavelength) or a tunable laser enabling very fast wavelength switching becomes available, 2D B-scan imaging of tumor pH could be achieved at higher speed or even in real-time fashion. In the future, 3D imaging of the tumor microenvironment is also possible, either by performing a scan of a linear array ultrasound probe or by using a more advanced 2D array ultrasound probe.

The commercially available SNARF-5F is considered as a long-wavelength fluorescent pH indicator, and has been well-developed and widely used for fluorescence based measurement of pH *in vitro*. This is the reason that the SNARF-5F was employed to build the pH sensing PAA NPs in this proof-of-principle study. Working in the spectral range of 565-600 nm, quantitative imaging of pH by quad-wavelength ratiometric PA measurement can be achieved with satisfactory accuracy in subsurface tissue at a depth up to 6 mm. We have further estimated the error in pH quantification due to the optical attenuation at different wavelengths for quad-wavelength PA ratiometric imaging, as described in **Figure 2.14**. As expected, the error becomes larger when the imaging depth increases. However, at 6-mm depth in an optically scattering tissue, the error caused by the optical attenuation was less than 0.16 pH. This error could be further reduced by compensating the wavelength-dependent optical attenuation when simulating the point-by-point pH levels. In another experiment, as described in the **Figure 2.15**, we have further assessed the sensitivity limit of PA imaging in detecting the SNARF-PAA NPs in subsurface tissue. At the depth of 6 mm in an optically scattering tissue, a SNARF-PAA NP solution at very low concentration of 0.05 mg ml^{-1} can still be detected with a good signal-to-noise ratio (SNR) over 20 dB. The 6-mm depth achieved by PA pH imaging is one order of

magnitude deeper than that accessible by fluorescence microscopy. With the current imaging depth, many clinical applications on relatively superficial tumors become possible, such as head and neck cancer, colorectal cancer, and cervical cancer, which are all associated with an acidic tumor microenvironment[39-41]. For imaging of deeper tumors, pH indicating dyes that absorb at longer optical wavelengths (e.g. 650-950 nm) will be needed so as to further improve the optical penetration. One advantage of our PAA NP system is that replacing the dye inside the NP is quite simple.

2.4 Conclusion

In oncology, low pH (acidosis) is believed to influence cell metabolism and tumor progression. We believe that our imaging technique has a high potential for cancer research by answering some important general biological or pathological questions. With its many advantages, this non-invasive and non-ionizing imaging technique is also highly translational, and may enable image-guided treatment of cancer in clinical settings. It has been reported that the cytotoxicity, i.e. efficacy, of certain drugs such as daunorubicin, doxorubicin, and mitoxantrone are reduced under acidic condition; while other drugs, such as chlorambucil, cyclophosphamide, and 5-fluorouracil, show higher cytotoxicity at lower pH[42]. Therefore, being capable of quantifying the pH level of the tumor microenvironment using imaging technology may enable instant optimization of chemotherapy and facilitate personalized treatment for cancer patients. In addition, this nanotechnology based imaging method can readily be applied to other diseases where pH plays an important role. The PA nanosensors described in this work can also be developed for other biologically relevant chemical analytes and thus functional imaging of

other physiological parameters (e.g. hyperkalemia or hypoxia) can be realized using the chemical PAI approach. On top of the sensing capability, other therapeutic agents (i.e. chemotherapy and/or photo-activated therapy) can also be incorporated into such a multifunctional nanoparticle[34, 35], turning them into theranostic nanoparticles. Our PA chemical imaging method can thus broaden the field of nano-diagnostics and even combine it with nano-therapeutics.

2.5 Methods

Chemicals

All chemicals were purchased from Sigma Aldrich or ThermoFisher Scientific unless otherwise noted.

Synthesis of SNARF-PAA NP and F3 surface modification

SNARF-5F has a pKa ~7.2 which is optimal for sensing near neutral physiological pH. The SNARF-5F was encapsulated by polyacrylamide polymers crosslinked by glycerol dimethacrylate (GDMA) to produce SNARF-PAA NPs[29]. All reactions were performed in the dark. Monomer solution containing 1.3 mL of Millipore water, SNARF-5F 5-(and-6)-carboxylic acid (SNARF) (3mg in 100 μL DMSO), Acrylamide (9.7 mmol), 3-(aminopropyl)methacrylamide hydrochloride salt (APMA) (0.3 mmol), and the crosslinker, GDMA, (2 mmol) was added and emulsified in a surfactant solution of AOT (1.6g) and Brij L4 (3.3 mL) in Hexane (45 mL). The polymerization was initiated by addition of N,N,N′,N′-tetramethylethylenediamine (TEMED) (100 μL) and 10% (w/w) Ammonium Persulfate (100 μL). A small percentage of APMA was introduced as another monomer to provide primary

amines used for later surface modification. The reaction was allowed to stir for 2 hours and hexane was removed by rotary evaporation. The prepared nanoparticles were washed with ethanol and water with Amicon Filter Cell using a 300 kDa filter, and then lyophilized. Although slight leaching of the dye was observed initially, during purification, there was no leaching during further steps of the synthesis. The surface of the SNARF-PAA NP was PEGylated and conjugated with tumor homing F3 peptides, following previous protocols[32]. The cancer targeting capability of our PAA NPs conjugated with F3 peptides has been extensively studied[30, 43, 44]. Bi-functional Polyethylene Glycol (MAL-PEG-SCM, 2kDa, Creative PEGWorks) (4 mg) was added into SNARF-PAA in PBS (pH 7.4) (50 mg per 2.5mL). After 30 min of stirring, it was washed with PBS using Amicon Ultra Centrifugal Filter (100 kDa) and F3 Peptide (KDEPQRRSARLSAKPAPPKPEPKPKKAPAKKC, RS Synthesis) (11mg) was added and stirred overnight. Cysteine (0.63 mg) was added and stirred for 2 hours to deactivate unreacted maleimide groups. The NP solution was washed with water and lyophilized. Blank PAA NPs were synthesized in the same method without SNARF-5F. The dye loadings of the nanoparticles were approximately 2.4 nmol of SNARF-5F per 1 mg of NPs. The SNARF-PAA NP was characterized by UV-VIS spectroscopy (UV-1601 Spectrometer, Shimadzu), fluorescence spectroscopy (FluoroMax-3, Horiba), and Dynamic Light Scattering instrument (DLS, Delsa Nano C particle analyzer instrument, Beckman Coulter).

Study of free SNARF-5F and SNARF-PAA NP interactions with albumin using UV-VIS

Different pH buffers were prepared by mixing different amounts of NaOH and KH_2PO_4. The pH level of each sample was confirmed using the micro pH electrode. To study the free SNARF-

5F and the SNARF-PAA NP interactions with proteins, human serum albumin (HSA) (4 mg ml-) was introduced into different pH buffers containing either free SNARF-5F or SNARF-PAA NPs (2 mg ml^{-1}). Free SNARF-5F dye concentration was equivalent to that loaded in SNARF-PAA NPs. The possible change in the optical absorption property of each sample containing either free SNARF-5F or SNARF-PAA NPs caused by interaction with HSA was measured using the UV-1601 Spectrometer (Shimadzu).

Imaging system

PAI of phantoms and animals *in vivo* was performed using our US and PA dual imaging system built on a commercially available research US platform (V1, Verasonics, Redmond, WA) and a linear array probe working at a central frequency of 11.25 MHz (CL15-7, Philips, Andover, MA,). The laser light was from an optical parameters oscillator (Slopo, Continuum, Santa Clara, CA) pumped by an Nd:YAG laser (Surelite, Continuum, Santa Clara, CA) working at a 10 Hz pulse repetition rate and with a pulse width of 5 ns. The details of this imaging system have been introduced in our former publication[45]. Powered by a GPU card, this dual-modality system can acquire PA and US images from the same sample at the same time, both in real-time fashion with a frame rate of 10 Hz (i.e. the laser pulse repetition rate). The fast imaging speed is highly valuable for functional PA imaging, because multi-wavelength images need to be acquired within a relatively short time period before functional parameters potentially change. The quantified spatial resolution for PAI are 226 μm lateral and 166 μm axial at a depth of 6 mm. The light beam on the sample surface formed a rectangle shape with a size of 1.5 cm by 3 cm. The light fluence was less than 20 mJ cm^{-2} which, according to the ANSI standard, is safe for human skin.

The good sensitivity of this system in imaging SNARF-PAA NPs in subsurface tissue has been validated, as the details shown in **Figure 2.15**. At a very low concentration of 0.05 mg ml^{-1} (400 times dilution of the injection concentration), an SNR over 20 dB was achieved in imaging SNARF-PAA NPs at 6-mm depth in optically scattering tissue.

Method of dual-wavelength ratiometric photoacoustic pH measurement

To obtain the calibration line for dual-wavelength ratiometric PA measurement of pH, SNARF-PAA NP solutions (concentration 20 mg ml^{-1}) with different pH levels from 5.8 to 7.7 (0.1 pH interval) were measured at two wavelengths (i.e. 565 nm and 600 nm). The pH level of each solution was confirmed by the pH electrode. Illuminated by the laser beam, the PA signals from each solution were collected by a cylindrically focused ultrasound transducer (V312, Panametrics). The signal amplitude at 600 nm divided by the signal amplitude at the isosbestic point of 565 nm gave a ratio. With ratios from three samples at each pH level (n=3), an average and a standard deviation were obtained.

Method of quad-wavelength PA ratiometric imaging of pH

To overcome the problem faced by dual-wavelength ratiometric PAI, a method based on PAI at additional wavelengths, i.e. quad-wavelength ratiometric PAI was proposed. Besides the original two optical wavelengths involved in dual-wavelength ratiometric imaging (i.e. 565 nm and 600 nm), another two additional wavelengths (i.e. 576 nm and 584 nm) were introduced to separate the contributions to spectroscopic PA measurement from the two forms of hemoglobin and the SNARF-PAA NP. The wavelength at 584 nm is an isosbestic point where HbO_2 and Hb

have the same optical extinction coefficient. At 576 nm, the optical extinction coefficient of HbO_2 has a local peak, enabling high sensitivity in separating the two forms of hemoglobin.

Assuming that the main chromophores in the target sample are HbO_2, Hb, and SNARF-PAA NP, then the PA intensity at wavelength λ can be expressed as in Equation (1):

$$P_\lambda = k\left[\varepsilon_{HbO_2\_\lambda}\, C_{HbO_2} + \varepsilon_{Hb\_\lambda}\, C_{Hb} + \varepsilon_{NP\_\lambda}\, C_{NP}\right], \quad (1)$$

where k is a constant depending on experimental conditions including the Grüneisen parameter of the tissue, the light fluence, and the sensitivity of the imaging system. Assuming that the light fluence, after calibration of the output energy from the laser, are the same for all the optical wavelengths, k will be independent of the wavelength. This assumption holds when the optical wavelengths applied are close and the imaging depth is limited, as discussed in detail in **Figure 2.14**. ε indicates the absorption coefficient of HbO_2, Hb, or NP at wavelength λ, and C is the concentration of HbO_2, Hb, or NP. Similar to the optical absorption of SNARF-PAA NPs at 600 nm, the optical absorption of SNARF-PAA NPs at 576 nm or 584 nm can be expressed as a linear function of the optical absorption at the isosbestic point of 565 nm and the pH value:

$$\varepsilon_{NP\_\lambda} = \varepsilon_{NP\_\lambda 565}(\alpha \cdot \mathrm{pH} + b) \quad (2)$$

where the constants α and b for each wavelength (576 nm, 584 nm, and 600 nm) can determined by performing ratiometric PA measurement of the SNARF-PAA NPs *ex vivo*. Therefore, the PA signal amplitudes at all the four wavelengths can be written as:

$$P_{\lambda 565} = k\left[\varepsilon_{HbO_2\_\lambda 565}\, C_{HbO_2} + \varepsilon_{Hb\_\lambda 565}\, C_{Hb} + 0 \cdot \mathrm{pH}\, \varepsilon_{NP\_\lambda 565}\, C_{NP} + 1 \cdot \varepsilon_{NP\_\lambda 565} C_{NP}\right] \quad (3)$$

$$P_{\lambda576} = k\left[\varepsilon_{HbO_2\_\lambda576}\, C_{HbO_2} + \varepsilon_{Hb\_\lambda576}\, C_{Hb} + \alpha_{\frac{I_{\lambda576}}{I_{\lambda565}}}\,\mathrm{pH}\,\varepsilon_{NP\_\lambda565}\, C_{NP} + b_{\frac{I_{\lambda576}}{I_{\lambda565}}}\,\varepsilon_{NP\_\lambda565} C_{NP}\right] \quad (4)$$

$$P_{\lambda584} = k\left[\varepsilon_{HbO_2\_\lambda584}\, C_{HbO_2} + \varepsilon_{Hb\_\lambda584}\, C_{Hb} + \alpha_{\frac{I_{\lambda584}}{I_{\lambda565}}}\,\mathrm{pH}\,\varepsilon_{NP\_\lambda565}\, C_{NP} + b_{\frac{I_{\lambda584}}{I_{\lambda565}}}\,\varepsilon_{NP\_\lambda565} C_{NP}\right] \quad (5)$$

$$P_{\lambda600} = k\left[\varepsilon_{HbO_2\_\lambda600}\, C_{HbO_2} + \varepsilon_{Hb\_\lambda600}\, C_{Hb} + \alpha_{\frac{I_{\lambda600}}{I_{\lambda565}}}\,\mathrm{pH}\,\varepsilon_{NP\_\lambda565}\, C_{NP} + b_{\frac{I_{\lambda600}}{I_{\lambda565}}}\,\varepsilon_{NP\_\lambda565} C_{NP}\right] \quad (6)$$

The Equation (3)-(6) can be converted to matrix form:

$$k \cdot \begin{bmatrix} \varepsilon_{HbO_2\_\lambda565} & \varepsilon_{Hb\_\lambda565} & 0 & \varepsilon_{NP\_\lambda565} \\ \varepsilon_{HbO_2\_\lambda576} & \varepsilon_{Hb\_\lambda576} & \alpha_{\frac{I_{\lambda576}}{I_{\lambda565}}}\varepsilon_{NP\_\lambda565} & b_{\frac{I_{\lambda576}}{I_{\lambda565}}}\varepsilon_{NP\_\lambda565} \\ \varepsilon_{HbO_2\_\lambda584} & \varepsilon_{Hb\_\lambda584} & \alpha_{\frac{I_{\lambda584}}{I_{\lambda565}}}\varepsilon_{NP\_\lambda565} & b_{\frac{I_{\lambda584}}{I_{\lambda565}}}\varepsilon_{NP\_\lambda565} \\ \varepsilon_{HbO_2\_\lambda600} & \varepsilon_{Hb\_\lambda600} & \alpha_{\frac{I_{\lambda600}}{I_{\lambda565}}}\varepsilon_{NP\_\lambda565} & b_{\frac{I_{\lambda600}}{I_{\lambda565}}}\varepsilon_{NP\_\lambda565} \end{bmatrix} \begin{bmatrix} C_{HbO_2} \\ C_{Hb} \\ \mathrm{pH}\cdot C_{NP} \\ C_{NP} \end{bmatrix} = \begin{bmatrix} P_{\lambda565} \\ P_{\lambda576} \\ P_{\lambda584} \\ P_{\lambda600} \end{bmatrix} \quad (7)$$

$$k \cdot \begin{bmatrix} C_{HbO_2} \\ C_{Hb} \\ \mathrm{pH}\cdot C_{NP}\cdot\varepsilon_{NP\_\lambda565} \\ C_{NP}\cdot\varepsilon_{NP\_\lambda565} \end{bmatrix} = \begin{bmatrix} \varepsilon_{HbO_2\_\lambda565} & \varepsilon_{Hb\_\lambda565} & 0 & 1 \\ \varepsilon_{HbO_2\_\lambda576} & \varepsilon_{Hb\_\lambda576} & \alpha_{\frac{I_{\lambda576}}{I_{\lambda565}}} & b_{\frac{I_{\lambda576}}{I_{\lambda565}}} \\ \varepsilon_{HbO_2\_\lambda584} & \varepsilon_{Hb\_\lambda584} & \alpha_{\frac{I_{\lambda584}}{I_{\lambda565}}} & b_{\frac{I_{\lambda584}}{I_{\lambda565}}} \\ \varepsilon_{HbO_2\_\lambda600} & \varepsilon_{Hb\_\lambda600} & \alpha_{\frac{I_{\lambda600}}{I_{\lambda565}}} & b_{\frac{I_{\lambda600}}{I_{\lambda565}}} \end{bmatrix}^{-1} \begin{bmatrix} P_{\lambda565} \\ P_{\lambda576} \\ P_{\lambda584} \\ P_{\lambda600} \end{bmatrix}. \quad (8)$$

The left side of Equation (8) as a 4×1 matrix can be computed when all the variables on the right side of the equation are known or can be determined by multi-wavelength PA measurements. Then blood sO_2 and the pH level of each pixel in the imaging plane can be computed by

$$\mathrm{sO}_2 = \frac{kC_{HbO_2}}{k(C_{HbO_2}+C_{Hb})} \quad (9)$$

$$\mathrm{pH} = \frac{k \cdot pH \cdot C_{NP} \cdot \varepsilon_{NP\_\lambda 565}}{k \cdot C_{NP} \cdot \varepsilon_{NP\_\lambda 565}} \quad . \tag{10}$$

The images showing the relative distribution of total hemoglobin concentration and the relative distribution of the SNARF-PAA NP can be computed by

$$\mathrm{THb} = k \cdot (C_{HbO_2} + C_{Hb}) \tag{11}$$

$$\mathrm{NP} = C_{NP} \cdot \varepsilon_{NP\_\lambda 565} \tag{12}$$

where both k and $\varepsilon_{NP\_\lambda 565}$ are constants. MATLAB (R2010a, Mathworks, Natick, MA) was used for simulation of the results from the phantoms and the animals.

Before quad-wavelength ratiometric PAI can be performed, we first need to obtain the calibration lines for 576 nm and 584 nm wavelengths, respectively, in addition to the calibration line for 600 nm as shown in **Figure 2.9b**. Following the same procedure, SNARF-PAA NP (concentration 20 mg ml^{-1}) with pH from 5.8 to 7.7 (0.1 pH interval) was measured at the wavelengths of 565 nm, 576 nm, and 584 nm. The PA signal amplitudes at 576 nm and 584 nm were divided by the signal amplitude at the isosbestic point of 565 nm. With measurements from three samples at each pH level (n=3), averages and standard deviations were obtained. The calibration lines here (**Figure 2.10a**) were obtained using the well-calibrated single-element V312 transducer, benefiting from its excellent receiving sensitivity. However, the calibration lines are independent of the detection system, and also work for the PAI system based on the Verasonics US platform (**Figure 2.17**).

We intentionally selected the four optical wavelengths that are close so that the optical spectral range for quad-wavelength PA ratiometric imaging is relatively small (565-600 nm). In

this case, when the incident light energy on the sample surface can be calibrated for each wavelength, the distributions of the light fluence in the tissue can be considered similar for all the wavelengths. Otherwise, largely separated wavelengths can lead to significant difference in optical attenuation in tissue, which, if not compensated, can affect the accuracy in quantifying tumor pH using quad-wavelength PA ratiometric imaging. In other words, the optical spectrum selected needs to differentiate the optical spectra of HbO_2, Hb and pH-dependent SNARF-PAA NPs; while the optical attenuation in tissue cannot be largely different within the selected spectrum. We have further studied the potential error in pH quantification due to the spectroscopic difference in optical attenuation in tissue, as the details shown in **Figure 2.13**. At a depth of 6 mm in optically scattering tissue, the potential error caused by the difference in optical attenuation over the spectral range of 565-600 nm is about 0.16 pH. This already minor error can be further reduced by compensating the light attenuation in the simulation.

PAI on phantoms

For the studies on phantoms, including both dual-wavelength and quad-wavelength ratiometric imaging, the phantoms were made from porcine gel (concentration 80g L^{-1}). Each phantom contained SNARF-PAA NPs with a concentration of 20 mg ml^{-1}, and was buffered at different pH levels (pH 6.6, pH 7.0, and pH 7.4). For dual-wavelength ratiometric imaging, the PA image of a phantom at 600 nm, after being smoothed by Gaussian filter, was divided by the PA image at 565 nm, which led to a pixel-by-pixel PA ratiometric image of the phantom. For quad-wavelength ratiometric imaging, each phantom was imaged with the four wavelengths. Then the 2D pH image was computed following the procedure described. To study the potential

error in pH imaging caused by the background optical absorption, whole blood was added in some phantoms with a concentration of 1% (w/w). 1% blood content is reasonable, considering that, as reported in a literature, the blood content in human glioma tumor ranges from 0.95 to 2.79%[46]. To find out whether the pH measurement based on quad-wavelength ratiometric imaging is affected by the concentration of the SNARF-PAA NPs, phantoms were also made with different NP concentrations (2 mg ml^{-1}, 10 mg ml^{-1}, and 20 mg ml^{-1}).

PAI of tumor pH in a mouse model *in vivo*

All the procedures on live animals were approved by the University Committee on the Use and Care of Animals (UCUCA) of the University of Michigan (U-M). The mice were housed at the U-M Medical School in the Unit for Laboratory Animal Medicine (ULAM). In total, four mice (5 weeks old male, Athymic nude Fox/NU, Envigo) were used. 9L rat glioma cell line (American Type Culture Collection) was cultured in RPMI 1640 medium supplemented with 10% Fetal Bovine Serum (FBS) and 1% Antibiotic-antimycotic. Approximately 10^6 cells in 100 μL of culture media were subcutaneously injected on the back of each mouse. Each tumor was allowed to grow for 2-3 weeks until its volume reached around 0.5 cc as measured using a caliper.

The nude mice were anesthetized with the inhalation of 1.0-2.0% isoflurane mixing with oxygen. During imaging, the laser light covered the entire tumor area as well as some surrounding tissue. The ultrasound probe was fixed around 1 cm above the tumor. During imaging experiment, the body temperature of mouse was also maintained with a heating lamp. The SNARF-PAA NP solution (20 mg ml^{-1} in saline) was injected through tail-vein (250 mg NP

per kg body weight). The PA images were acquired before the injection (0 min), and at 15 min, 45 min, and 75 min respectively after the injection. To improve the signal-to-noise ratio, the PA images acquired at each wavelength were averaged 50 times. Considering that the wavelength switching time was 5-10 second, the total time period for PA imaging at the four wavelengths was less than 60 seconds. To avoid potential motion artifact, the animal especially the tumor area under the scan was fixed tightly during image acquisition using a home-fabricated fixation device. With the images from the four wavelengths acquired, the spatially distributed NP concentrations and the spatially distributed pH levels were computed for each time point. For image pixels with weak PA signals, calculating the ratios among different wavelengths, as performed in quad-wavelength PA ratiometric imaging, could have large errors caused by the background noise. Therefore, to reduce the possible errors, a universal threshold of 6 dB above the background noise level was set for PA intensity images, meaning that the pixel-by-pixel computation of the pH level was performed only for those pixels with intensities above the 6 dB threshold.

To provide a control, quad-wavelength PAI was also performed on normal tissues. For each mouse, the SNARF-PAA NP solution (20 mg ml^{-1} in saline) was subcutaneously injected into the thigh (50 mg NP per kg body weight). Since the distribution of the locally injected NPs in the thigh is relying on perfusion, instead of a single injection of a high dose, multiple spatially scattered injections each with smaller dose were applied aiming at achieving more homogenous distribution of NPs in the thigh. The PA images of the treated thigh were obtained at 10 min after the injection. The PA images at the four wavelengths were used to compute the spatially distributed pH levels in the thigh. After the imaging experiment was finished, the pH levels in the tumors and the thighs were measured by inserting the micro pH electrode in multiple positions in

the target tissues.

2.6 References

1. Adrogue, H.J. & Madias, N.E. Management of life-threatening acid-base disorders. First of two parts. *N Engl J Med* **338**, 26-34 (1998).
2. Grinstein, S., Swallow, C.J. & Rotstein, O.D. Regulation of cytoplasmic pH in phagocytic cell function and dysfunction. *Clin Biochem* **24**, 241-247 (1991).
3. Egginton, S., Taylor, E.W. & Raven, J.A. Regulation of tissue pH in plants and animals : a reappraisal of current techniques. (Cambridge University Press, Cambridge, UK ; New York; 1999).
4. Hsu, P.P. & Sabatini, D.M. Cancer cell metabolism: Warburg and beyond. *Cell* **134**, 703-707 (2008).
5. Warburg, O. On the origin of cancer cells. *Science* **123**, 309-314 (1956).
6. Vaupel, P., Kallinowski, F. & Okunieff, P. Blood flow, oxygen and nutrient supply, and metabolic microenvironment of human tumors: a review. *Cancer Res* **49**, 6449-6465 (1989).
7. Eil, R. et al. Ionic immune suppression within the tumour microenvironment limits T cell effector function. *Nature* **537**, 539-+ (2016).
8. Höckel, M. & Vaupel, P. Tumor Hypoxia: Definitions and Current Clinical, Biologic, and Molecular Aspects. *Journal of the National Cancer Institute* **93**, 266-276 (2001).
9. Raghunand, N. et al. Enhancement of chemotherapy by manipulation of tumour pH. *Br J Cancer* **80**, 1005-1011 (1999).
10. Tredan, O., Galmarini, C.M., Patel, K. & Tannock, I.F. Drug resistance and the solid tumor microenvironment. *J Natl Cancer Inst* **99**, 1441-1454 (2007).
11. Kato, Y. et al. Acidic extracellular microenvironment and cancer. *Cancer Cell Int* **13**, 89 (2013).
12. Gallagher, F.A. et al. Magnetic resonance imaging of pH in vivo using hyperpolarized 13C-labelled bicarbonate. *Nature* **453**, 940-943 (2008).
13. Gillies, R.J., Raghunand, N., Garcia-Martin, M.L. & Gatenby, R.A. pH imaging. A review of pH measurement methods and applications in cancers. *IEEE Eng Med Biol Mag* **23**, 57-64 (2004).
14. Longo, D.L. et al. A general MRI-CEST ratiometric approach for pH imaging: demonstration of in vivo pH mapping with iobitridol. *J Am Chem Soc* **136**, 14333-14336 (2014).
15. Rottenberg, D.A. et al. In vivo measurement of brain tumor pH using [11C]DMO and positron emission tomography. *Ann Neurol* **17**, 70-79 (1985).
16. Vavere, A.L. et al. A novel technology for the imaging of acidic prostate tumors by positron emission tomography. *Cancer Res* **69**, 4510-4516 (2009).
17. Berezin, M.Y. et al. Near-infrared fluorescence lifetime pH-sensitive probes. *Biophys J* **100**, 2063-2072 (2011).
18. Lee, H., Berezin, M.Y., Tang, R., Zhegalova, N. & Achilefu, S. Pyrazole-substituted near-infrared cyanine dyes exhibit pH-dependent fluorescence lifetime properties. *Photochem*

Photobiol **89**, 326-331 (2013).
19. Gilson, R.C. et al. Protonation and Trapping of a Small pH-Sensitive Near-Infrared Fluorescent Molecule in the Acidic Tumor Environment Delineate Diverse Tumors in Vivo. *Mol Pharm* **12**, 4237-4246 (2015).
20. Chen, Q. et al. A Self-Assembled Albumin-Based Nanoprobe for In Vivo Ratiometric Photoacoustic pH Imaging. *Adv Mater* **27**, 6820-6827 (2015).
21. Xu, M.H. & Wang, L.H.V. Photoacoustic imaging in biomedicine. *Rev Sci Instrum* **77** (2006).
22. Wang, X. et al. Noninvasive laser-induced photoacoustic tomography for structural and functional in vivo imaging of the brain. *Nature biotechnology* **21**, 803-806 (2003).
23. Wang, L.V. Multiscale photoacoustic microscopy and computed tomography. *Nature photonics* **3**, 503-509 (2009).
24. Yuan, J. et al. Real-time photoacoustic and ultrasound dual-modality imaging system facilitated with graphics processing unit and code parallel optimization. *Journal of Biomedical Optics* **18**, 86001-86001 (2013).
25. Chatni, M.R. et al. Functional photoacoustic microscopy of pH. *Journal of biomedical optics* **16**, 100503 (2011).
26. Kimbrough, C.W. et al. Targeting Acidity in Pancreatic Adenocarcinoma: Multispectral Optoacoustic Tomography Detects pH-Low Insertion Peptide Probes In Vivo. *Clin Cancer Res* **21**, 4576-4585 (2015).
27. Guha, S., Shaw, G.K., Mitcham, T.M., Bouchard, R.R. & Smith, B.D. Croconaine rotaxane for acid activated photothermal heating and ratiometric photoacoustic imaging of acidic pH. *Chem Commun (Camb)* **52**, 120-123 (2016).
28. Horvath, T.D., Kim, G., Kopelman, R. & Ashkenazi, S. Ratiometric photoacoustic sensing of pH using a "sonophore". *Analyst* **133**, 747-749 (2008).
29. Ray, A., Yoon, H.K., Koo Lee, Y.E., Kopelman, R. & Wang, X. Sonophoric nanoprobe aided pH measurement in vivo using photoacoustic spectroscopy. *Analyst* **138**, 3126-3130 (2013).
30. Orringer, D.A. et al. In vitro characterization of a targeted, dye-loaded nanodevice for intraoperative tumor delineation. *Neurosurgery* **64**, 965-971; discussion 971-962 (2009).
31. Winer, I. et al. F3-targeted cisplatin-hydrogel nanoparticles as an effective therapeutic that targets both murine and human ovarian tumor endothelial cells in vivo. *Cancer research* **70**, 8674-8683 (2010).
32. Nie, G. et al. Hydrogel nanoparticles with covalently linked coomassie blue for brain tumor delineation visible to the surgeon. *Small* **8**, 884-891 (2012).
33. Reddy, G.R. et al. Vascular targeted nanoparticles for imaging and treatment of brain tumors. *Clin Cancer Res* **12**, 6677-6686 (2006).
34. Koo, Y.E. et al. Brain cancer diagnosis and therapy with nanoplatforms. *Adv Drug Deliv Rev* **58**, 1556-1577 (2006).
35. Koo, Y.E. et al. Photonic explorers based on multifunctional nanoplatforms for biosensing and photodynamic therapy. *Appl Opt* **46**, 1924-1930 (2007).
36. Buck, S.M. et al. Optochemical nanosensor PEBBLEs: photonic explorers for bioanalysis with biologically localized embedding. *Curr Opin Chem Biol* **8**, 540-546 (2004).
37. Burtis, C.A. & Ashwood, E.R. Tietz Textbook of Clinical Chemistry, Edn. 3rd. (Saunders, 1999).

38. Jacques, S.L. Optical properties of biological tissues: a review. *Physics in Medicine and Biology* **58**, R37 (2013).
39. Loja, M.N. et al. Optical molecular imaging detects changes in extracellular pH with the development of head and neck cancer. *Int J Cancer* **132**, 1613-1623 (2013).
40. Hulikova, A., Vaughan-Jones, R.D. & Swietach, P. Dual role of CO2/HCO3(-) buffer in the regulation of intracellular pH of three-dimensional tumor growths. *J Biol Chem* **286**, 13815-13826 (2011).
41. Anderson, M., Moshnikova, A., Engelman, D.M., Reshetnyak, Y.K. & Andreev, O.A. Probe for the measurement of cell surface pH in vivo and ex vivo. *Proc Natl Acad Sci U S A* **113**, 8177-8181 (2016).
42. Chen, L.Q. & Pagel, M.D. Evaluating pH in the Extracellular Tumor Microenvironment Using CEST MRI and Other Imaging Methods. *Advances in Radiology* **2015**, 206405 (2015).
43. Winer, I. et al. F3-targeted cisplatin-hydrogel nanoparticles as an effective therapeutic that targets both murine and human ovarian tumor endothelial cells in vivo. *Cancer Res* **70**, 8674-8683 (2010).
44. Nie, G. et al. Hydrogel nanoparticles with covalently linked coomassie blue for brain tumor delineation visible to the surgeon. *Small* **8**, 884-891 (2012).
45. Yuan, J. et al. Real-time photoacoustic and ultrasound dual-modality imaging system facilitated with graphics processing unit and code parallel optimization. *J Biomed Opt* **18**, 86001 (2013).
46. Jain, R. et al. Quantitative estimation of permeability surface-area product in astroglial brain tumors using perfusion CT and correlation with histopathologic grade. *AJNR Am J Neuroradiol* **29**, 694-700 (2008).

Chapter 3: Photoacoustic and Fluorescence Potassium Imaging

This chapter has been adapted from the following publications with minor modifications:

Lee, C. H.; Folz, J.; Zhang, W.; Jo, J.; Tan, J.; Wang, X.; Kopelman, R., "Ion-selective nanosensor for photoacoustic and fluorescence imaging of potassium", *Analytical Chemistry,* **2017,** 89 (15), 7943-7949.

Lee, C. H.; Folz, J.; Zhang, W.; Jo, J.; Tan, J.; Wang, X.; Kopelman, R., "Correction to ion-selective nanosensor for photoacoustic and fluorescence imaging of potassium", *Analytical Chemistry,* **2017,** 89 (24), 13674-13674.

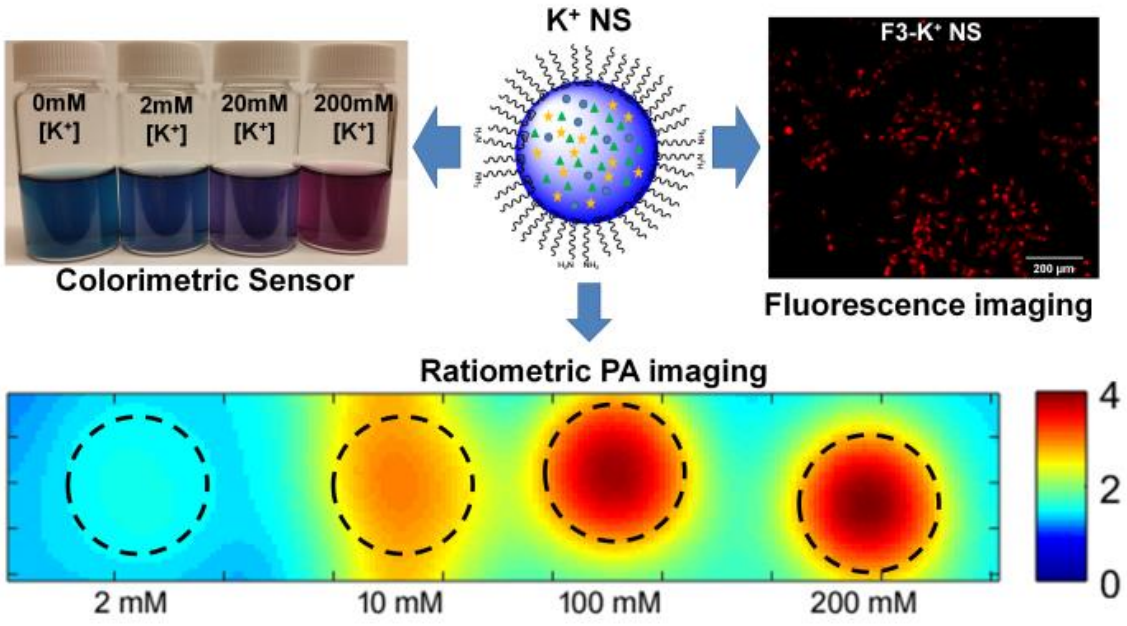

Figure 3.0 Graphical abstract

3.1 Introduction

The analysis of complex *ex vivo* biological fluids, such as whole blood or urine, has been one of the most valuable diagnostic tools in clinical chemistry, where much use is made of *ion selective electrodes* (ISEs).[1] The more recent alternative to ISEs, the *ion selective optodes* (ISOs), were originally ion selective bulk optodes - a type of electrolyte sensor composed of lipophilic sensing components embedded in lipophilic materials that provided colorimetric detection of the sensed ions.[1-4] A *cation selective bulk optode* senses the analyte cation through the competing equilibrium between H^+ and the analyte.[1-4] As the analyte binds to the lipophillic *ionophore* in the sensing matrix, the H^+ from the lipophillic *chromoionophore* (a pH indicator dye), in that sensing matrix, is exchanged with the analyte cation, so as to maintain the equilibrium between the media inside and outside the optode. The ratio between protonated and unprotonated chromoionophore, derived from the optical spectra, correlates with the analyte concentrations at fixed pH values. To achieve equivalent information inside live cells, *in vitro*, the ISOs had to be miniaturized, i.e, to the minute volumes covering optical fiber nano-tips,[5] or contained in nanoparticle-sensors (called NanoPEBBLEs).[6-26] With such miniaturization, the traditional optical absorbance based detection is impractical, and thus these ISOs had to be adapted to work in a fluorescence based mode, as *nano-optodes*, using fluorescence microscopy. Here we extend their capabilities, so as to also work as ISPAOs (ion-selective photo-acoustic optodes).

As pointed out above, optical ion sensors (or optodes) can be utilized by either absorbance or fluorescence based spectroscopy, depending on the design of the sensors and their application. Information acquired through optical spectroscopy allows accurate chemical sensing at a given location. However, the performance of such optodes has to compete with that of the “gold standard” of ion-selective electrodes (ISEs) for *in vivo* or *ex vivo* studies. A key advantage of

using optodes over ISEs is their potential to generate *non-invasive* chemical imaging, *in vitro* as well as *in vivo*. To generate chemical images using optically induced nano-sensors, one of two imaging modalities (fluorescence imaging and photoacoustic imaging) can be applied. Fluorescence imaging has already been applied to *in vivo* chemical, ion-selective, imaging.[27] However, as the imaging depth increases, not only does the signal-to-noise ratio decrease drastically, but also the spatial resolution degrades, as a result of the overwhelming scattering of light in tissues. As an alternative technology, photoacoustic (PA) imaging overcomes the above limitations of fluorescence imaging, while still keeping the high sensitivity in imaging the optical contrast agents.[27-32] The absorption of pulsed light by the molecules of the optical contrast agents is transferred into thermo-elastic expansion of tissue and then detected through ultrasound, with little scattering by tissues, thus significantly enhancing the spatial resolution when imaging objects beyond the sample's surface.

Here, a bimodal nanosensor (NS) has been prepared for K^+ as the target ion (called K^+ NS), which can be applied for both fluorescence and PA imaging modalities, i.e., as ISO or ISPAOs. The potassium ion, K^+ is one of the major biological cations; it is involved in controlling numerous physiological processes, such as enzyme activation, maintaining pH, regulation of blood pressure, as well as in nerve and muscle signal transmission. Just recently, Eil et al. reported that the typical elevation of extracellular K^+ concentration (5 to 10 folds increase) in the tumor microenvironment led to the suppression of the activity of immune cells.[33] *Immunotherapy* of tumors has been considered as one of the most promising avenues of cancer therapy, outdoing the traditional avenues of radiation- and chemo-therapy. Thus understanding the immune suppression mechanism due to abnormally high extracellular K^+ concentration (local *hyperkalemia*) created by the tumor is of high biological interest and may have a large

impact on research as well as in the clinic.

This bimodal K^+ sensing nanosensor (K^+ NS) is prepared with primary amine groups on the nanoparticle's surface, which can be used for surface modification, such as cell-specific targeting for *in vivo* applications.[34-36] Another potential usage of the primary amine groups is demonstrated by conjugating a near infrared (NIR) absorbing/fluorescence reference dye, so as to achieve an NIR absorbing nanosensor, which is preferable for *in vivo* studies, in order to minimize tissue light scattering during optical imaging. The prepared K^+ NS shows an excellent response to biologically relevant K^+ concentration changes (from extracellular 5 mM to intracellular 150 mM values),[37] while remaining silent towards other biologically relevant cations in that concentration range. The K^+ NS's response to K^+ concentrations is demonstrated here by using UV-VIS spectroscopy, fluorescence spectroscopy and PA spectroscopy, as well as by PA imaging.

3.2 Results and discussion

K^+ sensing nanosensor (K^+ NS) preparation and its response to different [K^+]

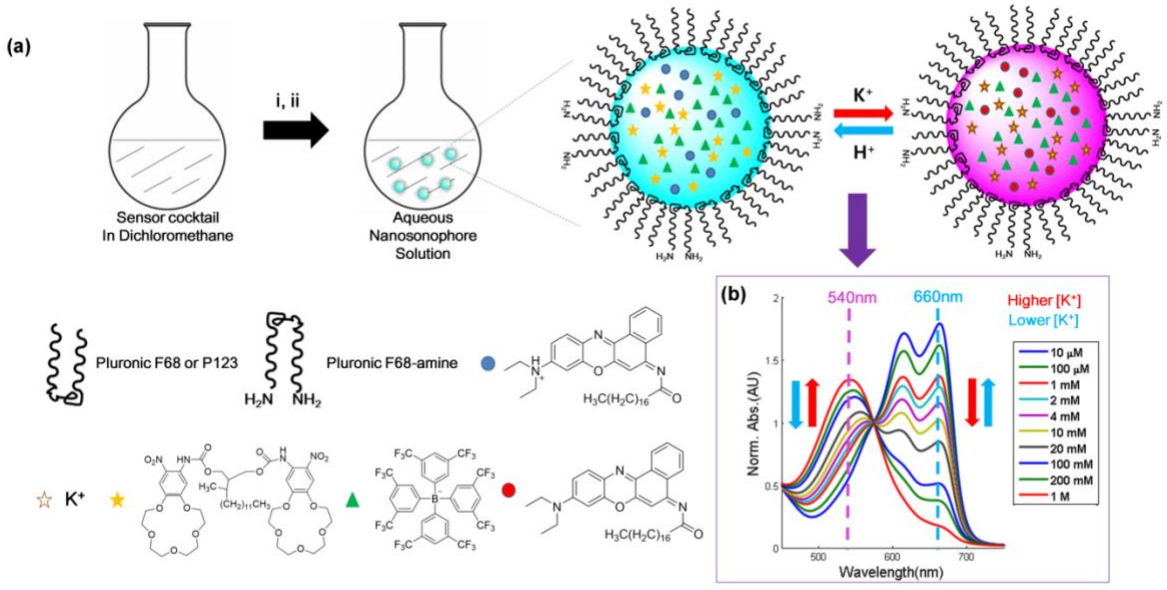

Figure 3.1 Nanosensor preparation and sensing schematic. (a) The K+ NS is prepared in two steps. i. DCM evaporation via vacuum and rehydration. ii. Free radical polymerization. The nanosensor matrix contains DOS and polybutylmethacrylate (depicted as background). (b) Absorption spectra of K+ NS at different concentrations of potassium (from 10 µM to 1 M). At low [K^+], the absorbance at 660 nm (depicted as blue dashed line in each spectrum) is much higher than the absorbance at 540 nm (depicted as pink dashed line in each spectrum). At high [K^+], the absorbance at 660 nm is much lower than the absorbance at 540 nm.

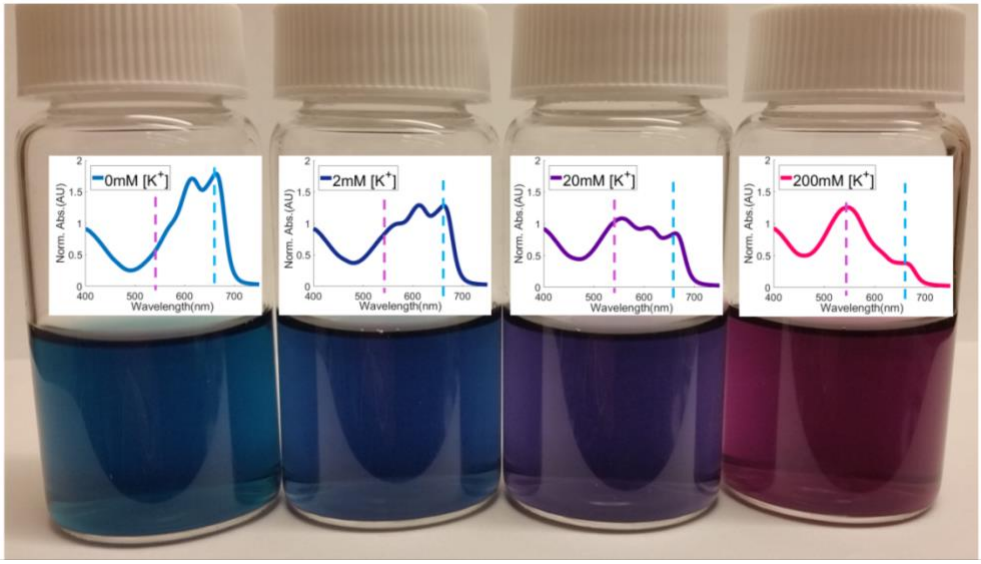

Figure 3.2 Photo and absorbance spectra of the K^+ NS at different K^+ concentrations.

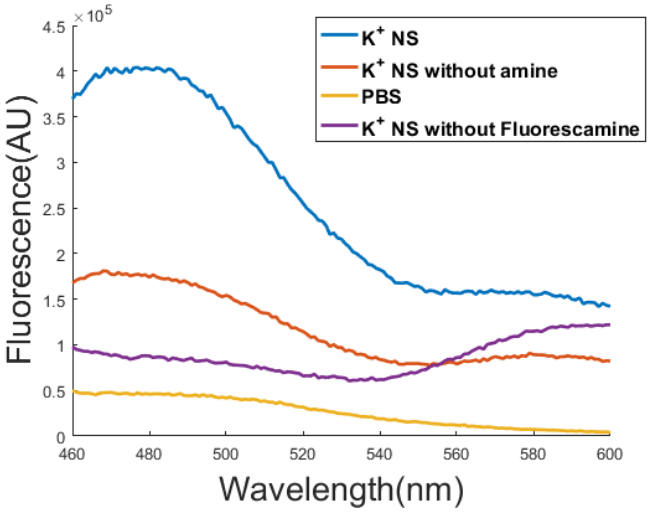

Figure 3.3 Determining Primary amine group availability by using Fluorescamine assay (390 nm ex). An analogue batch of K^+ NS without F68-amine was prepared (labeled "K^+ NS without amine"). Into 0.3mg/mL in PBS pH 7.4, 50 µL of fluorescamine solution (3mg/mL in DMSO) was added and left at room temperature for 10 min. "K^+ NS without Fluorescamine" is just K^+ NS fluorescence without addition of fluorescamine with 390 nm excitation. "PBS" indicates just fluorescamine and PBS pH 7.4.

The K^+ NS was prepared via regular micelle formation using Pluronics (**Figure 3.1a**). Each of

the self-assembled micelles contains all of the hydrophobic sensing components including acrylic monomers. The acrylic monomers in the core of the nano-sized micelles were polymerized via free radical polymerization to form the K^+ NS. Micelles are prone to fall apart below the critical micelle concentration. Thus, acrylic polymerization makes the core of the matrix more rigid, allowing the sensor to be more stable in biological settings. The K^+ NS exhibited an average size of around 60 nm when measured by dynamic light scattering. The sensor shows direct colorimetric changes with differing potassium concentrations (**Figure 3.2**). The primary amine group availability on the K^+ NS is confirmed by fluorescamine assay (**Figure 3.3**). Fluorescamine reacts with primary amines becoming fluorescence. The fluorescence of fluorescamine in K^+ NS was around 2 folds higher than the fluorescence of fluorescamine in K^+ NS without primary amine availability. **Figure 3.1b** shows absorption spectra of the K^+ NS at different K^+ concentrations. As the K^+ concentration increases, the chromoionophore inside the K^+ NS gets deprotonated (540 nm peak increases and 660 nm peak decreases), and *vice versa*. The ratio between two sensing peaks (540 nm and 660 nm) is used for calibration in the later studies.

K^+ NS calibration and its selectivity with respect to other cations

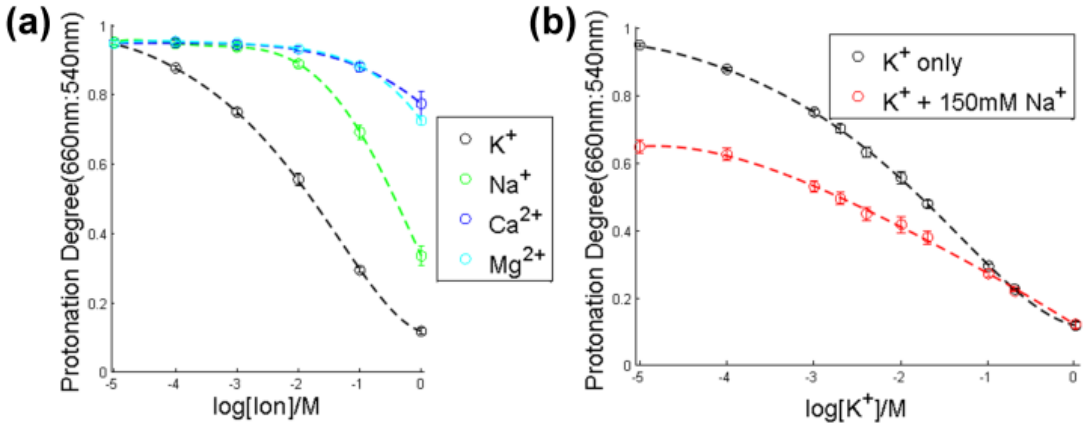

Figure 3.4 Characterization of the K^+ NS using UV-VIS spectroscopy. (a) Calibration curve of K^+ NS with protonation degree and log of potassium concentration by using the peak intensity ratios of the 540nm absorbance and 660nm absorbance of the K^+ NS in a pH 7.4 Tris-buffer (10 mM).[3] The selectivity of the K+ NS in comparison to other biological relevant cations (K^+, Na^+, Ca^{2+}, and Mg^{2+}). (b) The sensitivity of the K^+ NS to K^+ with and without Na^+ background (150 mM).

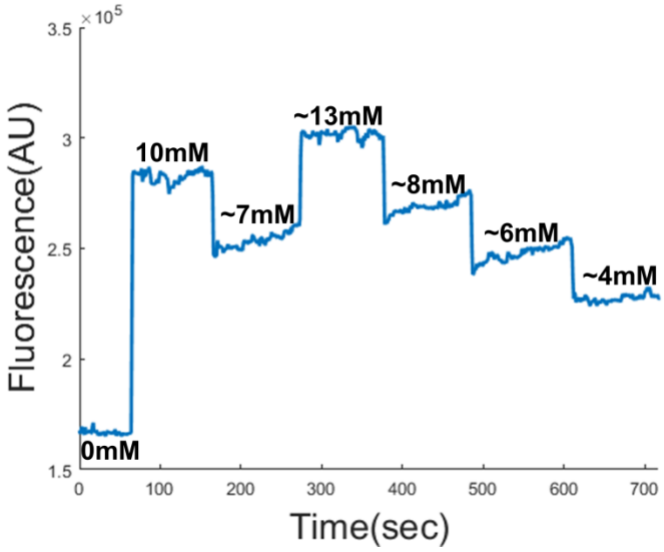

Figure 3.5 Reversibility of the K^+ NS. Into the stirring K^+ NS solution, potassium was added or diluted by adding extra solvent. The measurement was done using fluorescence spectrometer (540 nm ex/625nm em).

Both sensing peaks can be used to compute the calibration curve between protonation degree

and log of [K^+]. The protonation degree was calculated based on previously described methods using two sensing peaks.[3] The sensing component ratios were experimentally found to give a maximum change from 1 mM to 100 mM of K^+ concentrations (**Figure 3.4**). It was experimentally determined that the dynamic range of the sensor was influencing by the ratios between the sensing components. For example, a sensor made with low molar amounts of potassium ionophore III compared to chromoionophore I has optimal sensing range at lower potassium concentrations.

The K^+ NS is capable of sensing outside of the range (1 μM to 1 M), but absorbance changes at the sensing peaks are not as drastic as the 1 mM to 100 mM range. Although the potassium ionophores inside the optodes are designed to have strong binding affinities to certain ions, binding other ions that have similar sizes and properties cannot be completely avoided. The K^+ NS was tested for its selectivity compared to other biologically relevant cations (**Figure 3.4a**, Na^+, Ca^{2+}, and Mg^{2+}). The K^+ NS only starts to respond to Na^+, Ca^{2+} and Mg^{2+} concentrations higher than 10 mM while the sensor response in 100 μM of K^+. The sensor's selectivity of potassium over other cations is a few orders of magnitude higher. The responses of the K^+ NS from Ca^{2+} and Mg^{2+} are negligible since typical extracellular Ca^{2+} and Mg^{2+} concentrations are around 2.5 mM and 2 mM, respectively.[38] On the other hand, Na^+ is one of the most abundant cations in biological systems along with K^+ and sodium's typical extracellular concentration is around 140 mM.[37] In **Figure 3.4b**, the K^+ NS still possesses its sensing capability to potassium even with high background Na^+ concentration (150 mM). The background interference of sodium causes the calibration curve to shift a little bit, but similar trend has already been observed in ISOs and ISEs.[1] Thus, satisfactory calibrations can be generated in presence of other competing cations so as to measure K^+ in complex biological fluids. The sensor is fully reversible and can respond to local potassium changes within a few seconds (**Figure 3.5**).

K^+ NS Calibration by Photoacoustic (PA) Spectroscopy

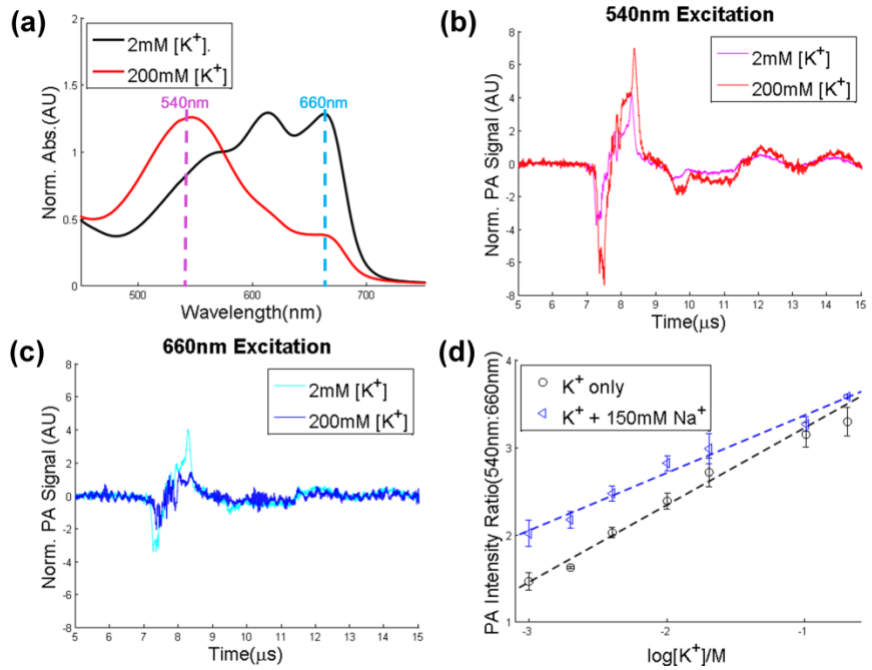

Figure 3.6 Characterization of the K^+ NS using photoacoustic spectroscopy. (a) Exemplary absorbance spectra of K^+ NS at 2 mM [K^+] (black) and 200 mM [K^+] (red). Two sensing peaks are indicated as dashed lines (540 nm as pink and 660 nm as blue). (b) Exemplary PA signals of the K^+ NS with 540 nm excitation. Purple line is PA signal of K^+ NS at 2 mM [K^+] with 540 nm excitation. Red line is PA signal of K^+ NS at 200 mM [K^+] with 540 nm excitation. (c) Exemplary PA signals of the K^+ NS with 660 nm excitation. Navy line is PA signal of K^+ NS at 2 mM [K^+] with 660 nm excitation. Blue line is PA signal of K^+ NS at 200 mM [K^+] with a 660 nm excitation. (d) Photoacoustic calibration curve of K^+ NS using the ratio (PA signal intensity at 540 nm divided by the PA signal intensity at 660nm) from 1 mM to 200 mM [K^+]. The PA ratios show logarithmic relationship with potassium concentrations in the absence (black circle) and presence (blue triangle) of 150 mM [Na^+].

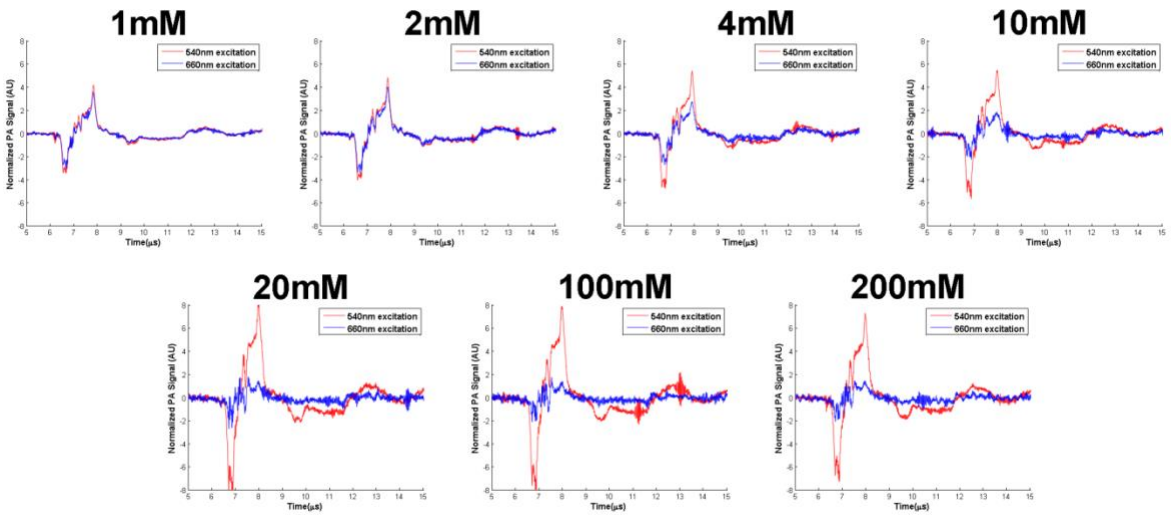

Figure 3.7 Examples of raw PA signals at different potassium concentrations.

The photoacoustic effect correlates with the absorbance characteristics of the optical contrast agent.[29] **Figure 3.6a** shows two absorption spectra of the K^+ NS in two different potassium concentrations (2 mM and 200 mM). As described, the absorbance at 540 nm increases and absorbance at 660 nm peak decreases as potassium concentration increases. **Figure 3.6b** and **Figure 3.6c** show the exemplary PA signals of K^+ NS in phantoms at different potassium concentrations. As potassium concentration increases from 2 mM to 200 mM, the PA signal intensity increases when excited with 540 nm (**Figure 3.6b**). On the other hand, PA signal intensity decreases as the potassium increases when excited with 660 nm (**Figure 3.6c**). Examples of raw PA signals at other potassium concentrations are shown in **Figure 3.7**. The sensor's absorption properties can be also detected through PA spectroscopy. The ratio between the intensities of PA spectra at two excitations (540 nm and 660 nm) gave the calibration curve (**Figure 3.6d**). Here, we directly plotted the ratio between two excitations to form the calibration curve. The PA ratio of the 540 nm over the 660 nm excitations shows a logarithmic relationship with the K^+ concentrations that we have tested (1 mM to 200 mM) in phantoms. From the absorbance

calibrations (**Figure 3.4b**), it is evident that the influence of the sodium background (150 mM) cannot be neglected. The PA ratios derived from the 540 nm and the 660 nm excitations were generated in the presence of physiological sodium concentrations (150 mM) and still formed logarithmic relationship with the potassium concentrations. Evidently, the sensitivity of the K^+ NS has been lowered due to the sodium interference. However, the typical extracellular potassium concentration is ~ 5mM while the tumor extracellular potassium concentration has been reported to be 5 to 10 folds higher.[33] The K^+ NS can still differentiate between 4 mM and 20 mM, as shown in the calibration curve.

K^+ NS Response to Photoacoustic (PA) Imaging

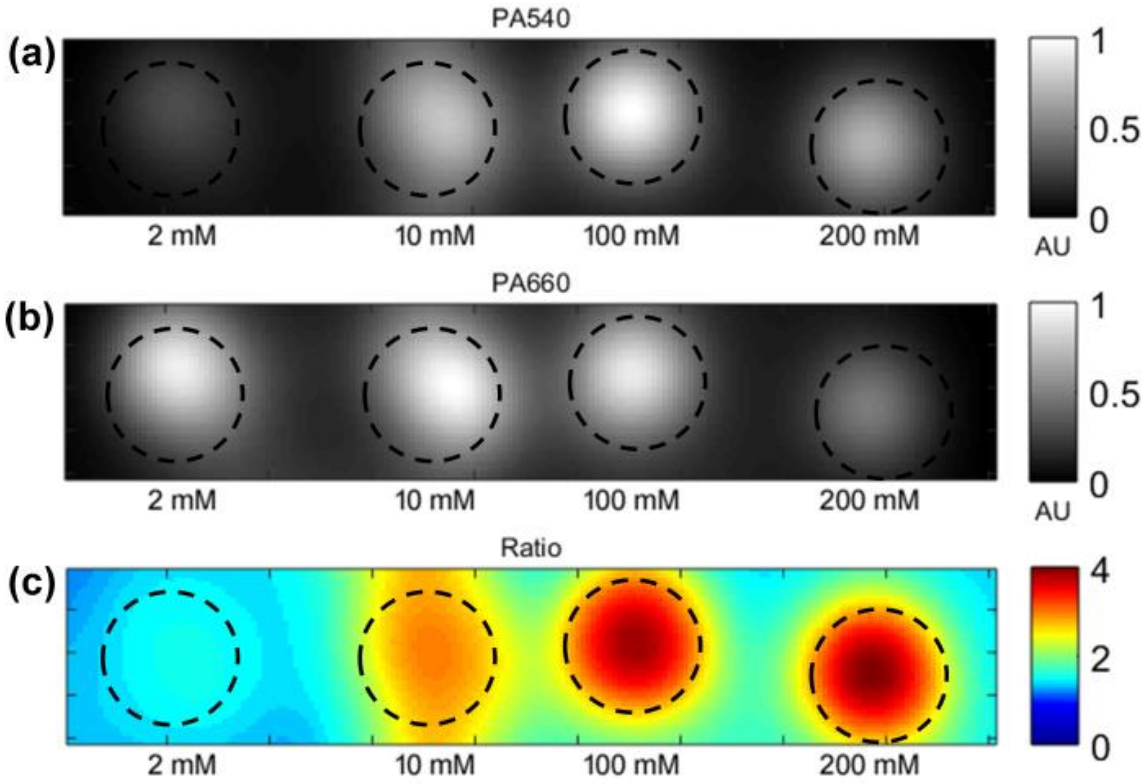

Figure 3.8 Photoacoustic imaging of phantoms containing K+ NS at different [K^+], labeled below each image (2mM. 10mM, 100mM, and 200mM). Black dashed circle indicates where the K^+ NS solutions are located in the phantom. (a) "PA540" is PA images of phantoms with a 540nm excitation. (b) "PA660" is a PA image of phantoms with a 660nm excitation.(c) Ratiometric photoacoustic images (540 nm over 660 nm) of phantoms containing K+ NS at different [K^+], as labeled below each image (2mM. 10mM, 100mM, and 200mM). PA imaging processing was performed by Dr. Janggun Jo.

The PA images of the four different K^+ concentrations (2 mM, 10 mM, 100 mM, and 200 mM) were taken simultaneously. Two images were taken with 540 nm (**Figure 3.8a**) excitation and 660 nm excitation (**Figure 3.8b**). Both Figure 4a and 4b do not show any specific trend at different potassium concentrations. Because a diverging lens was used to guide the laser pulse to the entire phantom, the power of the laser was not uniformly distributed among samples. The ratiometric PA

image (**Figure 3.8c**) shows clear differences between 2 mM, 10 mM, and 100 mM of potassium (**Figure 3.8c**). At concentrations 100 mM and 200 mM, the ratiometric PA intensities from the image do not differ too much, indicating that the sensor has almost reached its saturation near 200 mM. The results suggest that the sensor is applicable in PA imaging.

Utilization of primary amine groups on K^+ NS for Near-Infrared Absorption/Emission (NIR-K^+ NS)

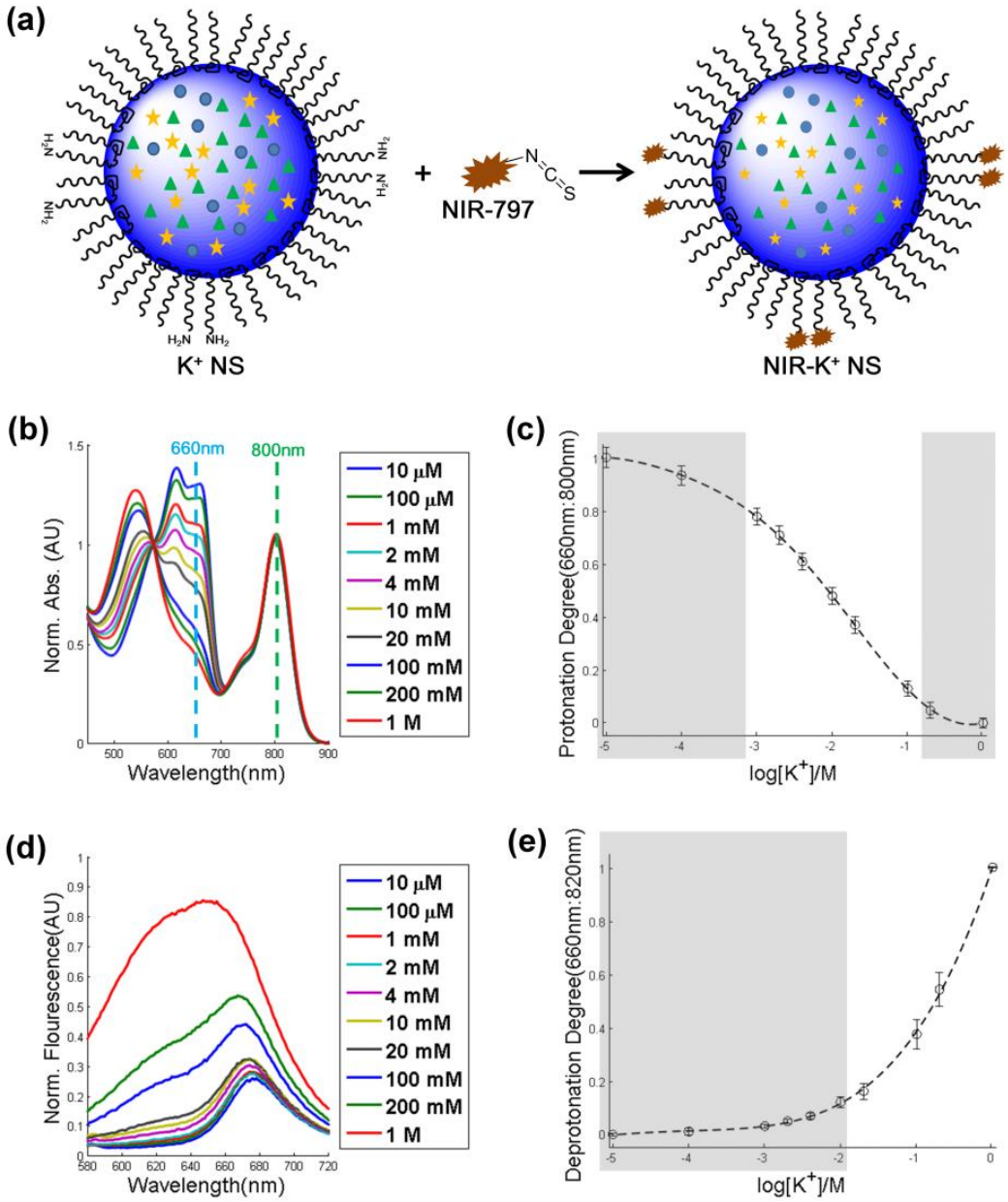

Figure 3.9 Optical and Sensing properties of NIR-K^+ NS. (a) Schematic of NIR-K^+ NS preparation. (b) Absorbance spectra of NIR K+ NS at different K^+ concentrations (10 μM to 1 M). (c) Calibration curve of K^+ NS with protonation degree *vs.* log potassium concentration, by using the peak intensity ratios of the sensing 660 nm absorbance and the reference 800 nm absorbance of the NIR-K^+ NS, in a pH 7.4 Tris-buffer.[3] (d)

Fluorescence emission spectra (540 nm excitation/660 nm emission) of NIR K^+ NS at different K^+ concentrations (10 μM to 1 M). The spectra were normalized by potassium independent NIR fluorescence (760 nm excitation/820 nm emission, data not shown). (e) Calibration curve of K^+ NS with deprotonation degree *vs.* log potassium concentration, by using the potassium dependent sensing emission (620 nm to 700 nm emission) and potassium independent reference emission (800 nm to 840 nm emission) of the NIR-K^+ NS, in a pH 7.4 Tris-buffer.[3]

One of the unique features that the K^+ NS possesses is the molecular engineering availability using a primary amine. Primary amine groups can be utilized for surface modification to conjugate both targeting moieties and reference dyes. Targeting moieties allow the nanoparticle to actively home in on a certain type of cells, e.g. cancer cells, giving the nanoparticle its cancer targetability *in vivo*.[34, 36] As for the PA imaging, the K^+ NS do not need a secondary reference dye because the chromoionophore already has two sensing peaks, the ratio of which can be used as an internal reference. However, the K^+ NS has only a single emission (~660 nm). One solution to this issue is by conjugating onto the K^+ NS nanoparticle matrix another potassium independent reference dye that absorbs at a higher wavelength (i.e., NIR-797), so as to acquire NIR absorbing K^+ NS. Generally, NIR wavelengths are preferred for light sources used for *in vivo* studies, as this minimizes both potential autofluorescence and the ubiquitous Raleigh light scattering, thereby allowing deeper penetration into biological tissues. Having primary amine groups on the surface of the K^+ NS provides much flexibility for modifications of the sensor. We conjugated an NIR absorbing dye that is insensitive to K^+ (NIR-797) onto the surface of the K^+ NS (giving NIR-K^+ NS, **Figure 3.9a**). **Figure 3.9b** shows the absorption spectra of the NIR-K^+ NS at different K^+ concentrations. As shown, the NIR absorbance at 800 nm can be used as the reference absorbance while that at 660 nm can still be used as the sensing peak. **Figure 3.9c** shows a calibration curve, plotting the protonation degree (using 660 nm for sensing and 800 nm for reference)[3] *vs.* log [K^+]. The absorbance based characterization shows no significant difference in the dynamic sensing

range of this modified sensor, compared to the original K^+ NS.

Interestingly, the fluorescence of the NIR-K^+ NS has quite a significantly different sensing range than the absorbance (**Figure 3.9d and Figure 3.9e**). The fluorescence of the NIR-K^+ NS gives the most drastic changes from 20 mM to 1M potassium (**Figure 3.9e**). This sensing range suites the intracellular potassium monitoring (typical intracellular potassium concentration is about 150 mM[37] while that of the sodium concentration is about 10 mM[12]). When the majority of the absorbance of K^+ NS is at 660 nm (i.e. low [K^+]), the fluorescence at 660 nm is low. When the majority of the absorbance of K^+ NS is at 540 nm (i.e. high [K^+]), the fluorescence at 660 nm is significantly higher. The chromoionophore, which is essentially a pH indicator, stays mostly protonated in the absence of potassium and becomes deprotonated in the presence of potassium. In the fluorescence calibration, the degree of protonation is only dictated by the deprotonated sensing peak (540 nm excitation), thus, forming an opposite trend from that of the absorbance calibration.

Fluorescence imaging of K^+ NS

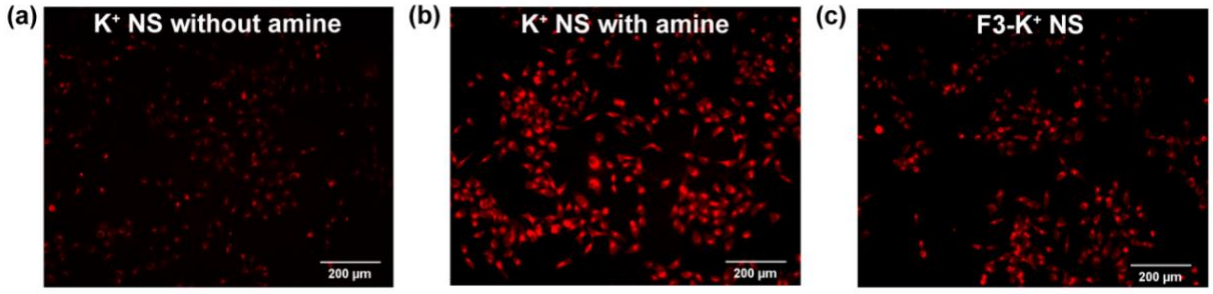

Figure 3.10 Fluorescence images of HeLa cells incubated with K^+ NS (10x). (a) K^+ NS without primary amine groups. (b) K^+ NS-with amine groups. (c) F3 peptide modified K^+ NS.

Another potential application of the primary amine groups for the K^+ NS is surface modification with targeting moieties, such as tumor homing F3 peptide[34, 35] and cardiac myoctye homing CTP[36]. Previous *in vivo* studies indicate that F3 peptide modified nanoparticles show an increased retention time and target tumors significantly better than non-targeted nanopraticles.[34, 35] The K^+ NS was surface modified with F3 peptide and fluorescence images were taken to monitor the uptake of the nanosensor by the cancer cells. **Figure 3.10** shows the fluorescence images of the cancer cells incubated with different types of the nanosensors. **Figure 3.10a** was incubated with K^+ NS without primary amine groups, **Figure 3.10b** was incubated with K^+ NS containing primary amine groups, and **Figure 3.10c** was incubated with F3 peptide modified K^+ NS (F3-K^+ NS).

The surfaces of the K^+ NS without primary amine groups are essentially PEGylated surfaces, making it least favorable for the uptake by the cancer cells (**Figure 3.10a**). On the other hand, the surface of the K^+ NS containing primary amine groups are positively charged and can be attracted by the negatively charged cellular membrane, leading to the highest uptake by the cancer cells (**Figure 3.10b**). During the surface modification with F3 peptide, the K^+ NS is essentially

PEGylated; thus, the surface charge is slightly neutralized compared to the unmodified K^+ NS (**Figure 3.10c**). The cellular uptake of the K^+ NS suggests that intracellular potassium imaging can indeed be accomplished through fluorescence imaging.

3.3 Conclusion

We report, for the first time to the best of our knowledge, an ion-selective nanosensor enabled through PA imaging. Furthermore, this sensor is bimodal, enabling also fluorescence-based ion-selective imaging. The sensor's sensitivity and selectivity to potassium, as demonstrated by the studies on phantoms, using both traditional absorbance spectroscopy and PA measurements, are well suited for the biologically relevant extracellular K^+ concentration range (1–100 mM). We also proposed, and demonstrated, a method of conjugating NIR dye molecules to the nanosensors, one that utilizes their surface modification by primary amine groups, thus, allowing having a fluorescence K^+ sensor with a biologically relevant intracellular potassium concentration sensing range, from 20 mM to 1 M. Also, the NIR absorption can shift the working wavelengths of the nanosensors into the NIR range, thereby facilitating both a lower background noise and a better imaging depth, which would be crucial for in vivo imaging. These results provide a proof of concept for enabling a nanoparticle that serves as a PA ion-selective sensor, and also serves as a fluorescence based, ion-selective sensor. We also demonstrated the ease of attaching a tumor homing ligand to the NS, without affecting its functionality. This work is an important stepping stone and may have a large impact on future studies of the local potassium ion concentrations in the tumor microenvironment in vivo (extracellular through PA imaging and intracellular through fluorescence imaging), especially when considering the importance of investigating the local

hyperkalemia found in tumor microenvironments and its reported suppression of immunotherapy. Furthermore, this design for an ISPAO can be easily generalized to most biologically relevant ions, in analogy to traditional ISOs, as well as ISEs.

3.4 Methods

Materials

All of the chemicals were purchased from Sigma-Aldrich unless otherwise noted.

K^+ Nanosensor (K^+ NS) preparation and characterization

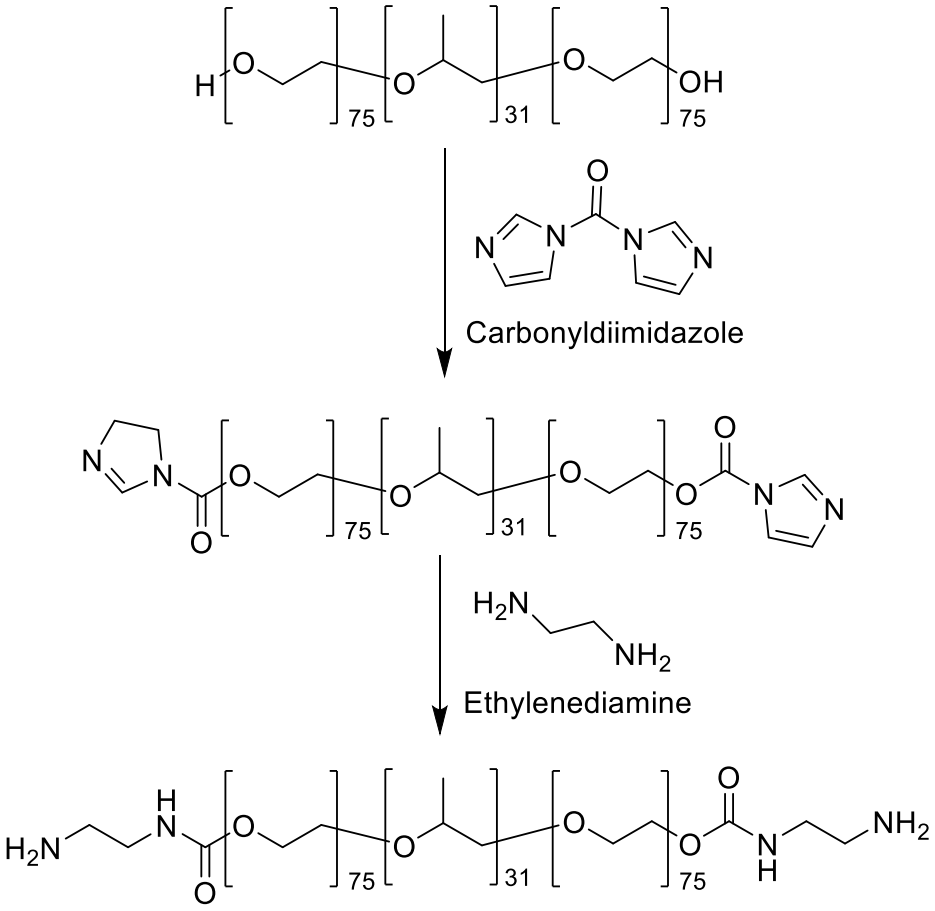

Figure 3.11 Synthetic route for Pluronic F68-Amine.[39]

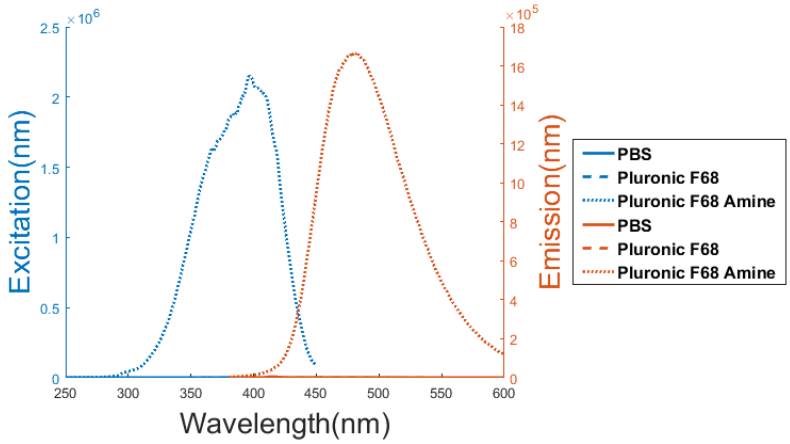

Figure 3.12 Determining Primary amine group availability by using Fluorescamine assay. Excitation and emission spectra of PBS, Pluoronic F68, and amine modified Pluronic F68 ("Pluronic F68 Amine") with fluorescamine addition. Into 1 mg/mL in PBS pH 7.4, 50 µL of fluorescamine solution (3mg/mL in DMSO) was added and left at room temperature for 10 min. "PBS" indicates just fluorescamine and PBS pH 7.4.

Amine modified Pluronic F68 was synthesized according to the previously reported methods (**Figure 3.11**).[39] Pluronic F68 (75.6mg), Pluronic P123 (116 mg, BASF), amine modified Pluronic F68 (8.4 mg), Dioctyl Secabacate (14 µL), chromoionphore I (1.5 mg, 2.57 mmol), potassium ionophore III (5 mg, 5.15 mmol), sodium tetrakis[3,5-bis(trifluoromethyl)phenyl]borate (NaTFPB) (9.75mg, 11mmol), butyl methacrylate (5 µL), and 1,6-hexanediol dimethaacrylate (5 µL) were dissolved in ~ 10 mL dichloromethane. Then, the solvent was evaporated via rotary evaporation and left in the hood, open, overnight. The thin film generated at the round bottom flask was re-suspended in Millipore water (10 mL). The suspended solution was flushed with Argon, while stirring, and 100 µL of ammonium persulfate (10% w/w in water) and 100 µL of N,N,N',N'-Tetramethylethylenediamine were injected into the solution to initiate radical polymerization of butyl methacrylate and 1,6-hexanediol diacrylate. After 2 hrs, the solution was purified by Amicon Ultra-15 Centrifugal Filter (100 kDa) with water (5 times) and Tris-HCl buffer (10mM) pH 7.4 (5 ~ 10 times) until the sensing solution turns blue. The size of K^+ Nanosonophore was measured by

Dynamic Light Scattering (Beckman Coulter). Absorption spectra were obtained by a UV-VIS spectrometer (Shimadzu UV-1601) and fluorescence spectra were obtained by a fluorimeter (Horiba FluoroMax-3). The primary amine group availability on the K^+ NS is confirmed by a fluorescamine assay (**Figure 3.3** and **Figure 3.12**). Fluorescamine is a non-fluorescence molecule which fluoresces upon reacting with primary amines. An analogous batch of K^+ NS was prepared with only Pluronic F68 instead of amine modified Pluronic F68. The fluorescence of fluorescamine in K^+ NS was several folds higher than the fluorescence of fluorescamine in K^+ NS without primary amine availability.

Photoacoustic Spectroscopy Setup

An optically clear polyvinyl chloride tube (I.D. x O.D. = 1/16 in. x 1/8 in.), containing solutions of the K^+ NS (~5mg/mL), with various concentrations of K^+ was placed in a water bath. An optical parametric oscillator (SLOPO Plus, Continuum), pumped with the second harmonic of a pulsed (5 ns) neodymium-doped aluminum garnet (Nd: YAG) laser (Surelite, Continuum), was used for excitation (at 540 nm and 660 nm wavelengths, respectively). The PA signal was detected by a 2.25 MHz unfocused ultrasonic transducer (V323, Panametrics) connected to an amplifier (5072PR, Olympus). The signal, digitalized by an oscilloscope (TDS540, Tektronix), was collected (averaged over 200 pulses). The laser pulse was focused with a converging lens where the sample is located inside the tube. The raw PA signals are normalized with the power of the laser and PA signals from the empty tube. The signal intensity at 540 nm when divided by the signal intensity at 660 nm gave the ratio used for calibration. With ratios determined for each sample at each potassium concentration (n = 4), an average and a standard deviation were obtained.

Photoacoustic Imaging Setup

Gelatin phantoms were prepared by dissolving gelatin (from porcine skin) in hot water (80g/L) containing four 16 gauge needles. Then, the phantom cooled down to room temperature overnight. The 16 gauge needles were carefully removed and 4 different solutions of K^+ NS (~5mg/mL) were carefully filled. As soon as the solutions were inserted, the PA images were acquired by an imaging system built on a commercially available research ultrasound platform (V1, Verasonics) with a linear array probe (CL15-7 with central frequency 11.25 MHz, Philips) working at 10 Hz. The laser pulse was diverged with a diverging lens so as to cover the entire imaging region (1.5 cm by 3 cm). The phantom PA images (540 nm and 660 nm) were averaged over 50 images and were smoothed by a Gaussian filter. The phantom PA image at 540 nm was divided by the phantom PA image at 660 nm so as to acquire the ratiometric potassium image.

Near Infrared absorbing K^+ Nanosensor (NIR-K^+ NS) preparation

To a stirring 10 mL of solution (~15mg of the K^+ NS in pH 7.4 phosphate buffered saline pH 7.4), 0.05 mg of NIR-797 isothiocyanate (5mg/100 μL in DMSO) was added and stirred overnight. The solution was purified by an Amicon Ultra-15 Centrifugal Filter (100 kDa) with water (5 times) and Tris-HCl buffer (10mM) pH 7.4 (5 to 10 times). The prepared NIR-K^+ NS was analyzed by a UV-VIS spectrometer and fluorimeter.

F3-K^+ NS preparation

To modify the surface of the K^+-NS, Bi-functional Polyethylene Glycol (MAL-PEG-SCM, 2kDa, Creative PEGWorks) (8 mg) was added into K^+-NS in PBS (pH 7.4) (50 mg/2.5mL). After 30 min of stirring, it was washed with PBS using an Amicon Ultra-15 Centrifugal Filter (100 kDa) and an F3 Peptide (KDEPQRRSARLSAKPAPPKPEPKPKKAPAKKC, RS Synthesis) (22mg)

was added and stirred overnight. Cysteine (1.26 mg) was added and stirred for 2 hours to deactivate unreacted maleimide groups. The nanosensor solution was washed with water (5 times) then concentrated before usage. To confirm F3 conjugation onto the K^+-NS, a separate batch was synthesized where the F3-peptide was pre-conjugated with NIR-797. The absorbance of NIR-797 was still visible after the purification.

Fluorescence Imaging Setup

HeLa cells (ATCC) were cultured in DMEM medium supplemented with 10% Fetal Bovine Serum (FBS) and 1% Antibiotic-antimycotic. Cells were incubated with K^+ NS (without amine), K^+ NS, and F3-K^+-NS (200 μg/mL) inside the growth medium for 30 minutes. After incubation, the nanosensor containing media were removed and washed with fresh colorless DMEM media (3 times). Cell images were immediately taken on an Olympus IX71 microscope (10x) using a high resolution monochromatic camera (Retiga 6000, QImaging). Cells were illuminated using a broad excitation filter (510-550nm) with a red (630nm) emission filter; the filters were originally optimized, and used without any modification, for propidium iodide. Images were captured using the Micro-Manager software package - an extension of ImageJ.

Degree of Protonation calculations

We note that calibrations in this field are performed as protonation degree, termed π or (1-α), *vs.* concentration, for both absorbance and fluorescence based measurements. The PA calibrations were generated by simply using the ratios of the two signal intensities. This degree of protonation (π = 1-α) was calculated as described previously.[3, 25] For the K^+ NS, the degree of protonation, for a system using two sensing signals, follows the standards equation (1) below.

$$\pi = 1 - \alpha = \frac{R - R_{min}}{R_{max} - R_{min}}, \quad (1)$$

where S is the scaling factor defined as $A_{540nm\ at\ 0.01M\ NaOH}/A_{540nm\ at\ 0.01M\ HCl}$, R is A_{660nm}/A_{540nm}, R_{min} is $A_{660nm\ at\ 0.01M\ NaOH}/A_{540nm\ at\ 0.01M\ NaOH}$, and R_{max} is $A_{660nm\ at\ 0.01MHCl}/A_{540nm\ at\ 0.01M\ HCl}$.

For NIR-K^+ NS, the degree of protonation, for a system using one sensing signal and one reference signal, follows the equation (2) below.

$$\pi = 1 - \alpha = \frac{R - R_{max}}{R_{max} - R_{min}}, \quad (2)$$

where R is A_{660nm}/A_{800nm} (or Fl_{660nm}/Fl_{820nm}), R_{max} is using R_{max} as $A_{660nm\ at\ 10\mu M\ KCl}/A_{800nm\ at\ 10\mu M\ KCl}$ (or $Fl_{660nm\ at\ 1M\ KCl}/Fl_{820nm\ at\ 1M\ KCl}$), and R_{min} as $A_{660nm\ at\ 1M\ KCl}/A_{800nm\ at\ 1M\ KCl}$ (or $Fl_{660nm\ at\ 10\mu M}/Fl_{820nm\ at\ 10\mu M}$). Fl_{660nm} represents all fluorescence intensities from Fl_{620nm} to Fl_{700nm} and Fl_{820nm} represents all fluorescence intensities from Fl_{800nm} to Fl_{840nm}.

3.5 References

1. Bakker, E., Bühlmann, P. & Pretsch, E. Carrier-Based Ion-Selective Electrodes and Bulk Optodes. 1. General Characteristics. *Chemical Reviews* **97**, 3083-3132 (1997).
2. Bühlmann, P., Pretsch, E. & Bakker, E. Carrier-Based Ion-Selective Electrodes and Bulk Optodes. 2. Ionophores for Potentiometric and Optical Sensors. *Chemical Reviews* **98**, 1593-1688 (1998).
3. Mistlberger, G., Crespo, G.A. & Bakker, E. Ionophore-Based Optical Sensors. *Annual Review of Analytical Chemistry* **7**, 483-512 (2014).
4. Xie, X. & Bakker, E. Ion selective optodes: from the bulk to the nanoscale. *Analytical and Bioanalytical Chemistry* **407**, 3899-3910 (2015).
5. Tan, W., Shi, Z., Smith, S., Birnbaum, D. & Kopelman, R. Submicrometer intracellular chemical optical fiber sensors. *Science* **258**, 778-781 (1992).
6. Shortreed, M.R., Dourado, S. & Kopelman, R. Development of a fluorescent optical potassium-selective ion sensor with ratiometric response for intracellular applications. *Sensors and Actuators B: Chemical* **38**, 8-12 (1997).
7. Clark, H.A., Hoyer, M., Philbert, M.A. & Kopelman, R. Optical Nanosensors for Chemical Analysis inside Single Living Cells. 1. Fabrication, Characterization, and Methods for Intracellular Delivery of PEBBLE Sensors. *Analytical Chemistry* **71**, 4831-4836 (1999).
8. Sumner, J.P., Aylott, J.W., Monson, E. & Kopelman, R. A fluorescent PEBBLE nanosensor for intracellular free zinc. *Analyst* **127**, 11-16 (2002).

9. Xu, H., Aylott, J.W. & Kopelman, R. Fluorescent nano-PEBBLE sensors designed for intracellular glucose imaging. *Analyst* **127**, 1471-1477 (2002).
10. Retter, R., Peper, S., Bell, M., Tsagkatakis, I. & Bakker, E. Flow Cytometric Ion Detection with Plasticized Poly(Vinyl Chloride) Microspheres Containing Selective Ionophores. *Analytical Chemistry* **74**, 5420-5425 (2002).
11. Brasuel, M.G., Miller, T.J., Kopelman, R. & Philbert, M.A. Liquid polymer nano-PEBBLEs for Cl- analysis and biological applications. *Analyst* **128**, 1262-1267 (2003).
12. Park, E.J., Brasuel, M., Behrend, C., Philbert, M.A. & Kopelman, R. Ratiometric Optical PEBBLE Nanosensors for Real-Time Magnesium Ion Concentrations Inside Viable Cells. *Analytical Chemistry* **75**, 3784-3791 (2003).
13. Sumner, J.P. & Kopelman, R. Alexa Fluor 488 as an iron sensing molecule and its application in PEBBLE nanosensors. *Analyst* **130**, 528-533 (2005).
14. Dubach, J.M., Harjes, D.I. & Clark, H.A. Ion-Selective Nano-optodes Incorporating Quantum Dots. *Journal of the American Chemical Society* **129**, 8418-8419 (2007).
15. Dubach, J.M., Harjes, D.I. & Clark, H.A. Fluorescent Ion-Selective Nanosensors for Intracellular Analysis with Improved Lifetime and Size. *Nano Letters* **7**, 1827-1831 (2007).
16. Dubach, J.M., Das, S., Rosenzweig, A. & Clark, H.A. Visualizing sodium dynamics in isolated cardiomyocytes using fluorescent nanosensors. *Proceedings of the National Academy of Sciences* **106**, 16145-16150 (2009).
17. Koo Lee, Y.E., Smith, R. & Kopelman, R. Nanoparticle PEBBLE Sensors in Live Cells and In Vivo. *Annual Review of Analytical Chemistry* **2**, 57-76 (2009).
18. Si, D., Epstein, T., Koo Lee, Y.-E. & Kopelman, R. Nanoparticle PEBBLE Sensors for Quantitative Nanomolar Imaging of Intracellular Free Calcium Ions. *Analytical Chemistry* **84**, 978-986 (2012).
19. Ruckh, T.T., Mehta, A.A., Dubach, J.M. & Clark, H.A. Polymer-Free Optode Nanosensors for Dynamic, Reversible, and Ratiometric Sodium Imaging in the Physiological Range. *Scientific Reports* **3**, 3366 (2013).
20. Xie, X., Crespo, G.A., Zhai, J., Szilagyi, I. & Bakker, E. Potassium-selective optical microsensors based on surface modified polystyrene microspheres. *Chemical Communications* **50**, 4592-4595 (2014).
21. Xie, X., Zhai, J. & Bakker, E. pH Independent Nano-Optode Sensors Based on Exhaustive Ion-Selective Nanospheres. *Analytical Chemistry* **86**, 2853-2856 (2014).
22. Ruckh, T.T. et al. Ion-Switchable Quantum Dot Förster Resonance Energy Transfer Rates in Ratiometric Potassium Sensors. *ACS Nano* **10**, 4020-4030 (2016).
23. Xie, X., Zhai, J., Jarolímová, Z. & Bakker, E. Determination of pKa Values of Hydrophobic Colorimetric pH Sensitive Probes in Nanospheres. *Analytical Chemistry* **88**, 3015-3018 (2016).
24. Brasuel, M., Kopelman, R., Kasman, I., Miller, T.J. & Philbert, M.A. in Proceedings of IEEE Sensors, Vol. 1 288-292 vol.281 (2002).
25. Barker, S.L.R., Shortreed, M.R. & Kopelman, R. Utilization of Lipophilic Ionic Additives in Liquid Polymer Film Optodes for Selective Anion Activity Measurements. *Analytical Chemistry* **69**, 990-995 (1997).
26. Shortreed, M., Bakker, E. & Kopelman, R. Miniature Sodium-Selective Ion-Exchange Optode with Fluorescent pH Chromoionophores and Tunable Dynamic Range. *Analytical Chemistry* **68**, 2656-2662 (1996).

27. Cash, K.J., Li, C., Xia, J., Wang, L.V. & Clark, H.A. Optical Drug Monitoring: Photoacoustic Imaging of Nanosensors to Monitor Therapeutic Lithium in Vivo. *ACS Nano* **9**, 1692-1698 (2015).
28. Wang, L.V. & Yao, J. A practical guide to photoacoustic tomography in the life sciences. *Nat Meth* **13**, 627-638 (2016).
29. Xu, M. & Wang, L.V. Photoacoustic imaging in biomedicine. *Review of Scientific Instruments* **77**, 041101 (2006).
30. Ray, A., Rajian, J.R., Lee, Y.-E.K., Wang, X. & Kopelman, R. Lifetime-based photoacoustic oxygen sensing in vivo. *Journal of Biomedical Optics* **17**, 057004 (2012).
31. Ray, A., Yoon, H.K., Koo Lee, Y.E., Kopelman, R. & Wang, X. Sonophoric nanoprobe aided pH measurement in vivo using photoacoustic spectroscopy. *The Analyst* **138**, 3126-3130 (2013).
32. Chen, Q. et al. A Self-Assembled Albumin-Based Nanoprobe for In Vivo Ratiometric Photoacoustic pH Imaging. *Advanced Materials* **27**, 6820-6827 (2015).
33. Eil, R. et al. Ionic immune suppression within the tumour microenvironment limits T cell effector function. *Nature* **537**, 539-543 (2016).
34. Herzog, E. et al. Optical Imaging of Cancer Heterogeneity with Multispectral Optoacoustic Tomography. *Radiology* **263**, 461-468 (2012).
35. Reddy, G.R. et al. Vascular Targeted Nanoparticles for Imaging and Treatment of Brain Tumors. *Clinical Cancer Research* **12**, 6677-6686 (2006).
36. Avula, U.M.R. et al. Cell-selective arrhythmia ablation for photomodulation of heart rhythm. *Science Translational Medicine* **7**, 311ra172 (2015).
37. Walker, H.K., Hall, W.D. & Hurst, J.W. (eds.) Clinical Methods: The History, Physical, and Laboratory Examinations, Edn. 3rd. (Butterworths, Boston; 1990).
38. Moe, S.M. Disorders Involving Calcium, Phosphorus, and Magnesium. *Primary care* **35**, 215-vi (2008).
39. Lu, H.-F. et al. Galactosylated PVDF membrane promotes hepatocyte attachment and functional maintenance. *Biomaterials* **24**, 4893-4903 (2003).

Chapter 4: Lifetime-based Photoacoustic O_2 Imaging

The introduction of this chapter has been adapted from a following submitted book chapter with minor modifications:

Lee, C. H.; Jo, J.; Wang, X.; Kopelman, R. "Photoacoustic imaging of oxygen" (Chapter 10). In D. B. Papkovsky and R. I. Dmitriev (Eds.), *Quenched-phosphorescence Detection of Molecular Oxygen*. The Royal Society of Chemistry.(2018, In Press).

4.1 Introduction

Oxygen (O_2) is inevitable for most living organisms. Humans, like other mammals, have evolved to precisely control the oxygen levels in their body. Imbalances or decreases in oxygen levels are expressed in various pathological states and can be fatal.[1, 2] Especially in tumors, oxygen levels are known to be significantly lower than in normal tissue. This cancer phenomena of *hypoxia*, has been discussed and explained by the Warburg effect.[3, 4] Hypoxia is observed not only in cancer but also in other inflammatory diseases, as well as in relation to the growth of stem cells.[5, 6]

There are two main approaches of measuring oxygen levels through PA imaging. One approach is through direct ratiometric measurements of oxygen carrying proteins, such as hemoglobin and myoglobin.[7-33] Hemoglobin (as well as myoglobin) changes its optical property, or simply color, with varying oxygen concentration, a well-established principle of pulse oximetry.[34, 35] The ratio of the PA signals at two or more light wavelengths allows a non-invasive indirect oxygen measurement *in vivo*. Another approach of measuring oxygen levels through PA is an extension of time-resolved (or transient absorption) spectroscopy, called *lifetime-based PA imaging*.[36-46] The

sensing mechanism is similar to that of phosphorescence quenching based oxygen sensors, but it is measured by PA imaging/spectroscopy, i.e. it is based on optical absorption rather than emission. Theories and examples for both methods are discussed in the subsequent sections.

Blood oxygenation provides indirect measurements of oxygen through oxygen binding blood proteins, not by measuring tissue oxygen. It is important to note that tissue hypoxia is not always accompanied by ischemia.[47] Moreover, intracellular oxygen monitoring can be as valuable a diagnostics tool as extracellular (i.e. blood) oxygen monitoring.[48] So as to directly measure tissue oxygenation, photoacoustic lifetime measurements for oxygen sensing (PALT) was introduced.[36, 37, 40, 41, 43-46, 49-51]

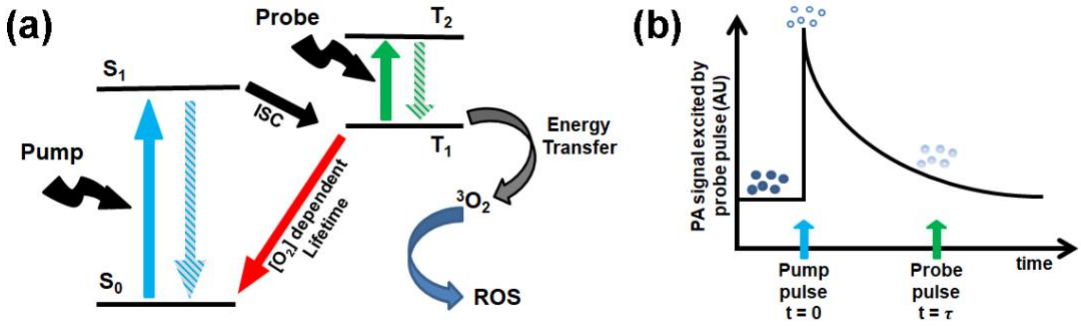

Figure 4.1 Basic mechanism of PALT. (a) An oxygen sensing dye (a dye molecule with a long-lived phosphorescence) at its ground state (S_0) absorbs the initial "pump" pulse (solid blue arrow). The excited molecule, through internal conversion (not shown) and intersystem crossing (ISC), quickly relaxes from the first excited singlet state (S_1) to the first (lowest) triplet state (T_1). Then, the "probe" pulse (solid green arrow) excites the dye molecules from the first triplet state to a higher lying triplet state. (b) The phosphorescence always decays exponentially and the exponential decay rate is known to correlate linearly with the oxygen concentration, typical of a first order reaction. The delay time between the pump and probe pulse ($t = \boldsymbol{\tau}$) can be controlled by a delay generator. Multiple PA signals from probe pulses are collected by varying

the delay times so as to compute the exponential decay rate.

The mechanism behind lifetime-based PA O_2 sensing is equivalent to that of phosphorescence quenching based O_2 sensing (**Figure 4.1**), but the signal is detected photoacoustically rather than optically. A standard phosphorescence based oxygen sensing dye can be excited into the first excited singlet state from its ground state by non-ionizing photonic radiation. This excited first singlet state can quickly relax into the lowest triplet state, which has a relatively long lifetime (typically in the μs range) due to the "forbidden" nature of the transition (requiring a change of spin, only allowed by a relativistic effect). Energy from the T_1 state can also be transferred into the paramagnetic triplet ground state of a neighboring oxygen molecule, creating "singlet oxygen" and then other reactive oxygen species (ROS) as side products. Thus the phosphorescence is "quenched" (red arrow) by oxygen, and the lifetime of the phosphorescence is dependent upon the probability of colliding with O_2 molecules, i.e. linear with the local O_2 concentration. The dashed lines represent non-radiative relaxation, i.e. local heating that creates ultrasound, which can be detected by the PA signal, including the long-lived relaxation (green dashed arrow).

The lifetime of the sensor dye's excited triplet state can be shortened by its interactions with the local environment, such as molecular O_2. The excited triplet state energy is thereby transferred into the paramagnetic "triplet") ground state O_2 molecule, creating singlet oxygen, and consequently other reactive oxygen species (ROS) as side products, while the sensor dye's triplet state lifetime is shortened during the process. The lifetime of the excited state of the dye (as well as its phosphorescence) correlates linearly with the local O_2 concentrations, as shown below by the Stern-Volmer relationship.

$$\frac{T^0}{T} = 1 + k_Q T^0 pO_2. \quad (1)$$

where T is the lifetime, pO_2 is the partial pressure of oxygen, T^0 is the lifetime at $pO_2 = 0$, and k_Q is the quenching rate constant.

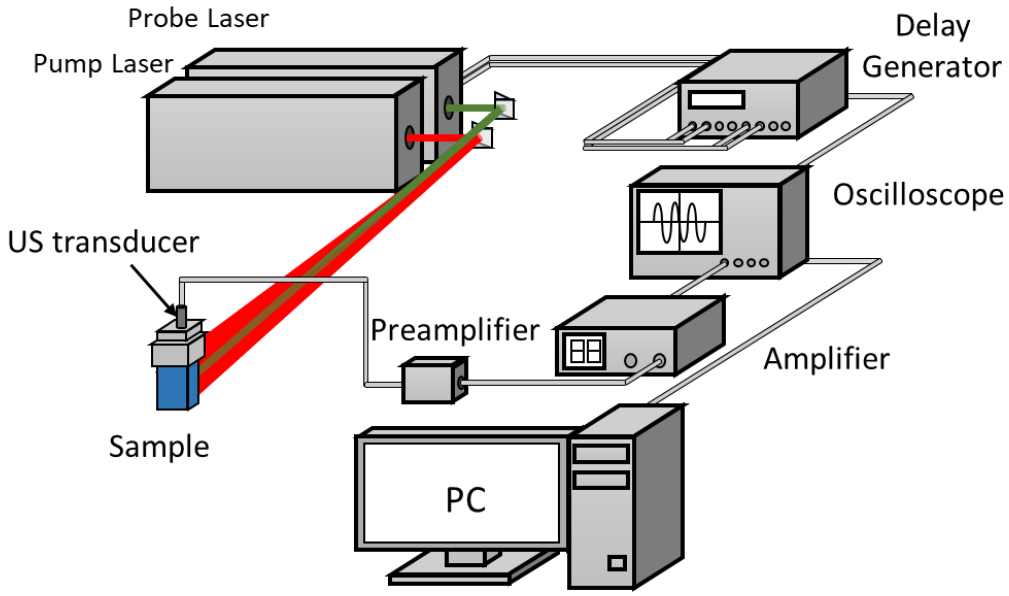

Figure 4.2 Exemplary PALT setup. The "pump" and "probe" laser beams are guided into the target (sample) region, triggered by a delay generator. PA signals are collected by an ultrasound (US) transducer.

Lifetime-based PA O_2 monitoring employs two laser pulses, called "pump" and "probe" beams (**Figure 4.2**). The pump beam excites the oxygen sensing dye molecules into their first excited singlet state, which quickly transfers the energy into the first triplet state. The PA signal acquired from the "pump" excitation can be detected through an ultrasound transducer. The probe beam allows measuring the transient absorption of the dye's triplet state, which can also be detected through the ultrasound transducer. By varying the delay times between the pump and probe beams (i.e. 1 µs, 2 µs, etc.), the exponential decay of the dye's triplet state can be computed (**Figure 4.1b**). The decay rate and lifetime vary with the O_2 concentration. It is also important to note that any

long-times transient absorption is not present for other biological chromophores, such as blood and melanin.

It is important to note that PALT requires a oxygen sensing dye, which can be easily coupled with nanotechnology.[52-56] Nanotechnology for biomedical applications has made significant advances over the past few decades. The main advantages relate to the delivery (i.e. by targeting) and protection (i.e., from blood enzymes).[57, 58] The surface of the nanoparticles can be engineered to conjugate targeting moieties, such as peptides and antibodies. The nanoparticle (NP) matrix can physically encapsulate and protect the the sensing dyes so as to protect them from interactions with any larger biomolecules, such as proteins (including enzymes). Such interactions may cause degradation of dyes or alterations in their optical properties. The NP can also include additional calibration dyes required for reliable chemical analysis *in vivo*. Several chemical nanosensors have been developed for multiple analytes, including oxygen.[58-63]

Here, a nanoparticle containing a known PALT oxygen indicator, Oxyphor G2, is prepared. The "proof-of-concept" experiment on the O2 sensing nanoparticle's oxygen sensing capability was performed by generating a calibration curve with photoacoustically measured lifetime and known oxygen concentrations. Also, an initial experiment on a mouse model *in vivo* has been performed. The PA lifetime imaging is able to differentiate tissue oxygen levels.

4.2 Results

Oxyphor G2 loaded polyacrylamide nanoparticle (G2-PAA NP) preparation and characterization

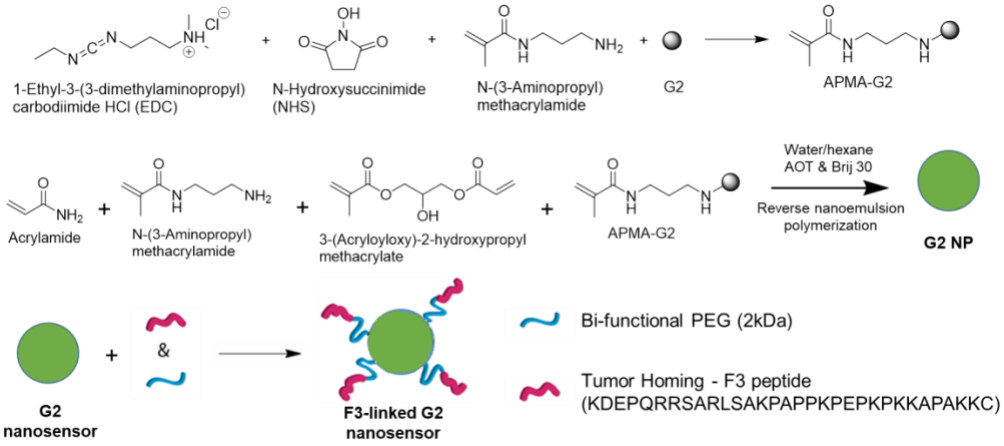

Figure 4.3 Schematic of Oxyphor G2 conjugated polyacrylamide nanoparticles.

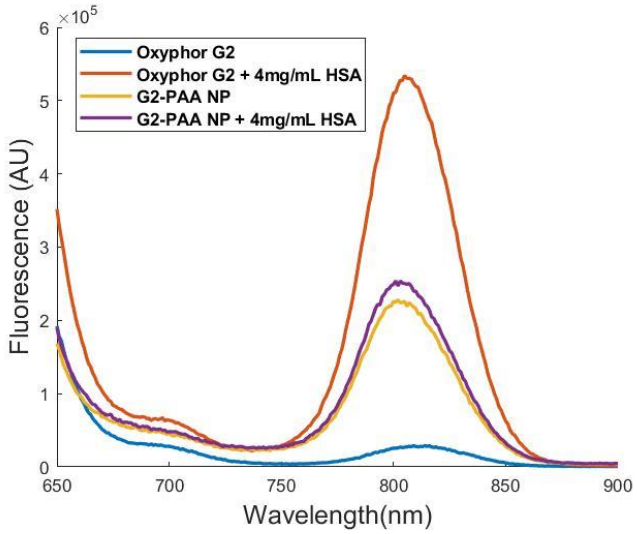

Figure 4.4 Fluorescence spectra of G2 PAA NP (0.5 mg/ml) and Oxyphor G2 (5 µg/ml) in phosphate buffered saline (pH 7.4) with and without human serum albumin (HSA, 4mg/ml).

Figure 4.3 describes the synthetic schematic of Oxyphor G2 conjugated polyacrylamide nanoparticles (G2-PAA NP). The surface of the G2-loaded nanoparticles (G2-PAA NP) was

PEGylated so as to minimize immune system recognition and further modified with a targeting moiety, the tumor homing F3 peptide. The hydrodynamic size of the G2-PAA NP was ~80 nm when measured by dynamic light scattering. One of the greatest advantages of using nanoparticles is contents protection. Oxyphor G2 has been known to interact with HSA changing its optical properties.[46] As shown in **Figure 4.4**, the fluorescence of free Oxyphor G2 has changed significantly when HSA (4mg/mL) was introduced into the solution. On the other hand, G2-PAA NP showed significantly less changes in fluorescence with HSA. Small molecules can interact with bigger bio-macromolecules such as HSA to undergo changes in its optical properties. The nanoparticle matrix can physically protect the sensing dye, Oxyphor G2, from interference, especially from large biomolecules, which would cause complications in *in vivo* studies.

PALT wavelength selection of G2-PAA NP

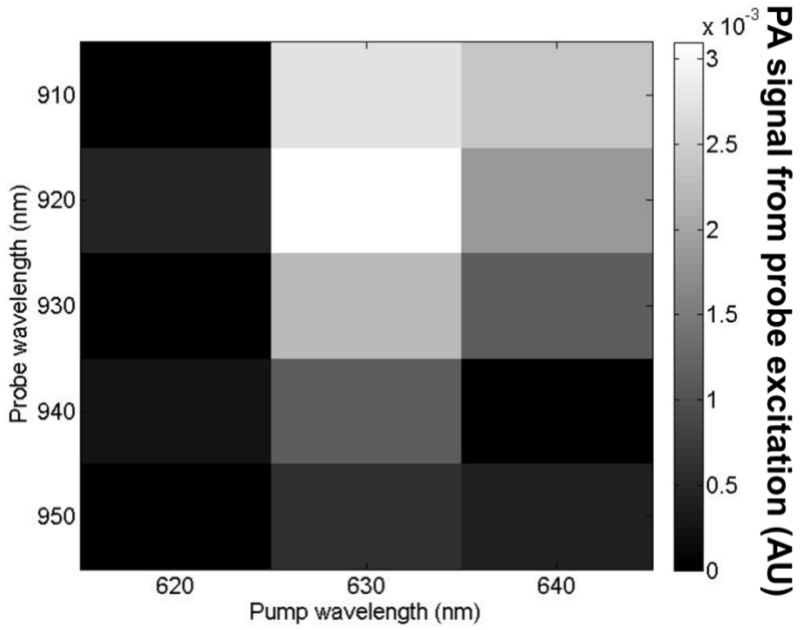

Figure 4.5 PA signal from probe beam distribution with different wavelengths of pump and probe beams. The gray-scale represents PA signal intensities from probe beam excitation.

Oxyphor G2, in its free dye form, has been tested with a PALT system previously.[46] It is well-known that absorption and fluorescence of the dye incorporated into nanoparticles are shifted from the dye's innate optical properties.[58] The PALT wavelengths used for Oxyphor G2 were 630 nm for the pump beam and 950 nm for the probe beam. However, we observed that PA signal from 630 nm and 950 nm was not optimal for the G2-PAA NPs (**Figure 4.5**). PA signal intensities from different probe beam wavelengths (910 nm, 920 nm, 930 nm, 940 nm, and 950 nm) with different pump beam wavelengths (620 nm, 630 nm, and 640 nm) were monitored. All 15 combinations of pump and probe beam wavelengths were tested. As shown in **Figure 4.5**, the combination of 630 nm pump beam and 920 nm probe beam gave the highest PA signals. Thus, these two wavelengths hve been applied for later PALT experiments.

PALT calibration *in vitro*

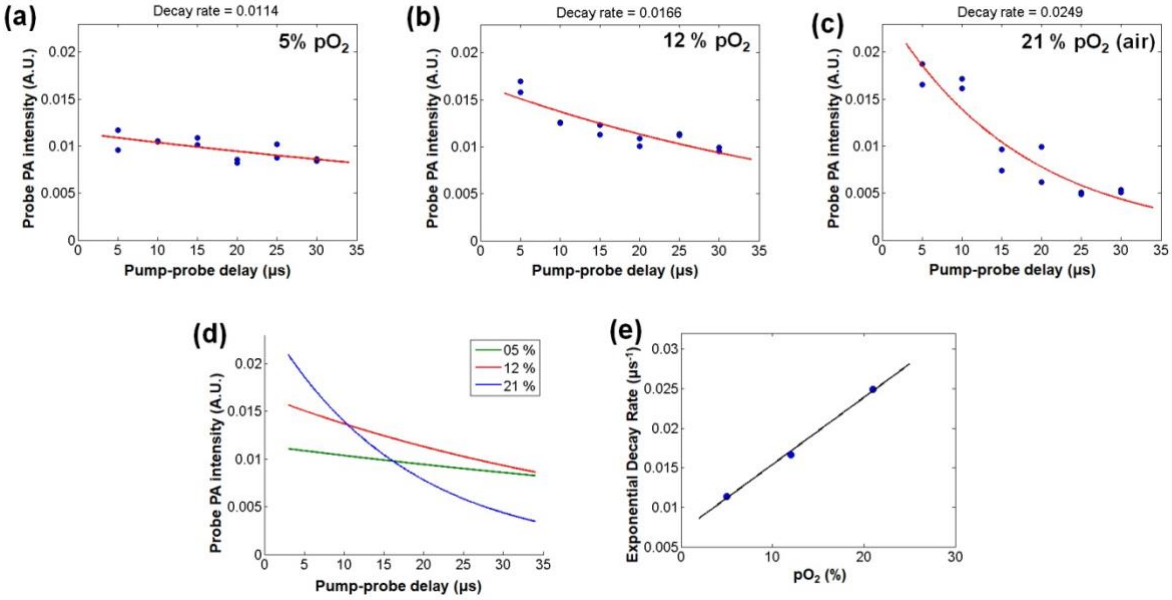

Figure 4.6 PALT with G2-PAA NP. The probe PA intensity was extracted with similar algorithm introduced in the previous section. 6 different pump-probe delays (5 μs, 10 μs, 15 μs, 20 μs, 25 μs, and 30 μs) were taken for the exponential decay curve fitting: (a) when pO_2 = 5%, (b) when pO_2 = 12%, and (c) when pO_2 = 21%. (d) Overlapped fitted exponential decay curves at different pO_2. (e) Calibration curve with pO_2 and computed exponential decay rates.

The oxygen sensitivity of the G2-PAA NP was confirmed by the PALT experiment (**Figure 4.6**). In **Figures 4.6a**, **4.6b**, and **4.6c**, the blue dots represent the extracted probe PA signal intensities, and the red lines represent the average exponential decay fit. As shown, the PA signal from the probe beam excitation decreased as the delay between pump and probe beam increases, indicating that the PA signal from the probe beam is relevant to the transient absorption. Also, the decay rate differs significantly at different oxygen concentrations (**Figure 4.6d**). The decay trend was fitted exponentially to give computed decay rates at different pO_2. The G2-PAA NP's computed exponential decay rates linearly correlate with pO_2, as described by a Stern-Volmer relationship, $\frac{T^0}{T} = 1 + k_Q T^0 pO_2$(**Figure 4.6e**).

PALT imaging of G2-PAA NP *in vivo*

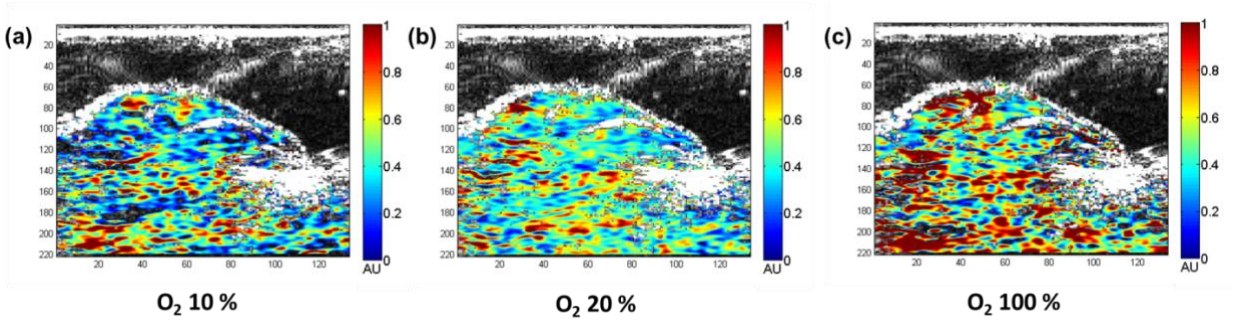

Figure 4.7 In vivo PALT imaging of G2-PAA NPs locally administrated in the thigh muscle of a mouse. Systemic oxygen saturation of the mouse was changed by adjusting the oxygen content in the inhaled gas. The colorimetric scale represents the normalized PALT exponential decay rates from 0 to 1 scale (AU). (a) Image when inhaling 10% oxygen. (b) Image when inhaling 20% oxygen. (c) Image when inhaling 100% oxygen. PA imaging processing and analyses were performed by Dr. Janggun Jo.

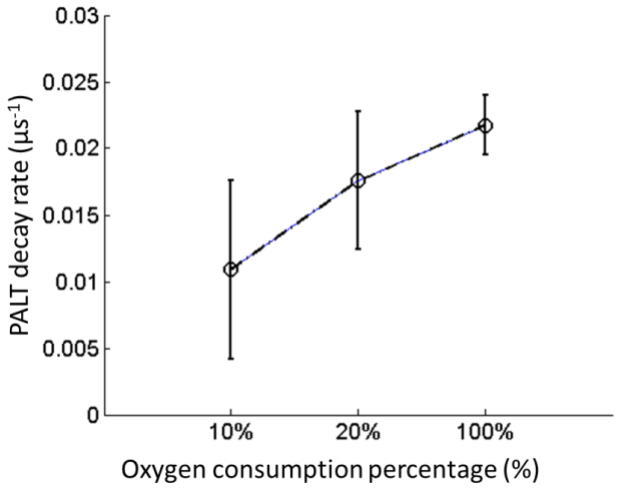

Figure 4.8 Normalized PALT exponential decay rate from the PALT images from Figure 4.7 (10%, 20% and 100% oxygen were allowed to inhale). Error bars represent the standard deviation (n=3).

An initial experiment on a mouse model *in vivo* has been performed (**Figure 4.7**). The oxygen saturation in the thigh muscle was imaged using PALT, where G2-PAA NPs were locally administrated into the thigh muscle. To change the tissue oxygen saturation level in the target

thigh muscle, we changed the content of oxygen in the breathing gas provided to the mouse. As shown, 100% oxygen inhalation (**Figure 4.7c**) exhibits much higher PALT decay rates in comparison to 10% (**Figure 4.7a**) and 20% (**Figure 4.7b**). As shown in **Figure 4.8**, average PALT decay rates from the PALT images show differences at different oxygen inhalation (**Figure 4.8**). The decay rates presented by the PALT image can reflect the change in local oxygen saturation in the imaged thigh muscle. This is an important preliminary study suggesting that our G2-PAA NP is responsive to different oxygen concentrations *in vivo*.

PALT imaging of G2-PAA NP *in vivo* tumor model

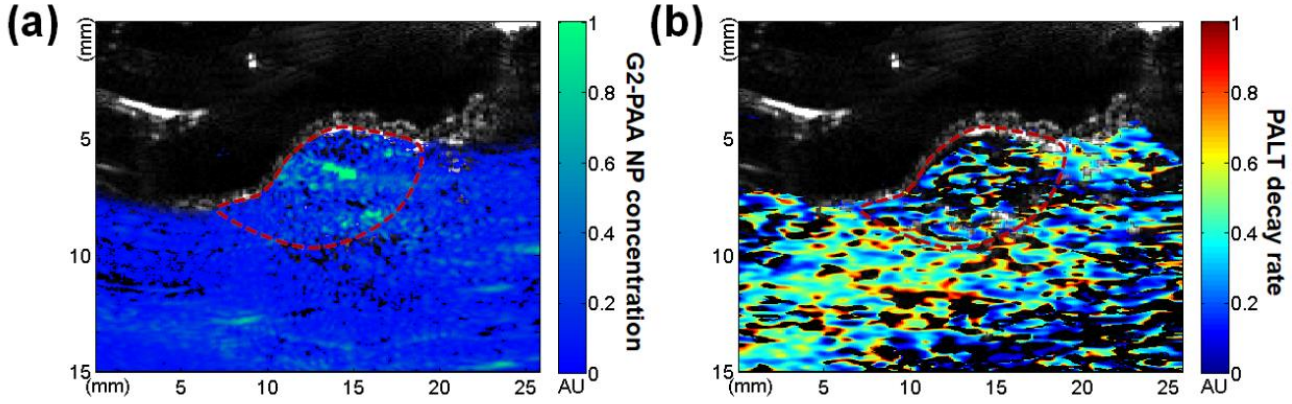

Figure 4.9 NP accumulation PA image and PALT image of the tumor *in vivo*. The PA image in pseudo-color is superimposed on the gray-scale US image. US image is used to delineate the tumor boundary (red dashed line). (a) PA image of the tumor *in vivo*. The colorimetric scale indicates G2-PAA NP concentration in arbitrary units. (b) PALT image of the tumor *in vivo*. The colorimetric scale indicates PALT decay rate in arbitrary units. PA imaging processing and analyses were performed by Dr. Janggun Jo.

The PA image shows nanoparticle accumulation around the tumor tissue *in vivo* (**Figure 4.9a**). The PA signals from G2-PAA NP were extracted by using algorithms similar to those

described previously.[58] The PA signal from NPs were spectrally unmixed using an algorithm similar to that introduced in PA hemoglobin oxygen monitoring (PA images from 576 nm, 584 nm, and 630 nm are used). PA signals are treated so that deoxy-hemoglobin, oxy-hemoglobin, and the tumor-targeted G2-PAA NP are the only optical absorbers in the imaging region. It is clear from the image that more G2-PAA NP accumulated inside the tumor in comparison to outside of the tumor.

PALT imaging of the tumor using the targeted nanosensor is also demonstrated *in vivo* (**Figure 4.9b**). The collected PA images were computed in a method similar to that described previously. The image contains raw PALT decay rates, normalized into a 0 to 1 scale. At a glance, the average PALT decay rate inside the tumor seems much less than the average PALT decay rate outside of the tumor. Also, the tumor boundary shows a slightly lower PALT delay rate (indicating a lower O_2 concentrations), in comparison to the normal tissue outside of the tumor boundary.

4.3 Discussion and Conclusion

Oxyphor G2 embedded nanosensors have been applied for PALT spectroscopy and imaging. The PALT decay rates measured with G2-PAA NP showed a linear correlation with known oxygen concentrations in phantoms. *In vivo* PALT images, showing PALT decay rates in colorimetric scale, were taken with subcutaneous injection of G2-PAA NP into the thigh of normal mice. The mice were allowed to breathe with 10%, 20%, or 100% oxygen concentrations, and the PALT images showed clear differences in the computed decay rates for the three conditions. A PALT image of an *in vivo* tumor embedded mouse also showed spatial gradient dependent information from the

decay rates.

Nanotechnology enabled PALT spectroscopy and *in vivo* PALT imaging have great potentials. The work is still inconclusive and needs more experiments. A key validation for this technique is to confirm that it is nanoparticle concentration independent. In case of *in vivo* studies, it is difficult to calculate exact nanoparticle concentrations. Other supplementary experiments, such as sensitivity of the G2-PAA NPs, minimal G2-PAA NP concentration requirements, photobleaching rate of the G2-PAA NPs, maximum imaging depth of the PALT imaging, minimum laser power requirement, etc., may all be in the future.

We conclude that PALT can be much advanced by combination with nanotechnology. PALT indicating dyes can be encapsulated by nanoparticles, providing great potential advantages for *in vivo* studies. The nanoparticle matrix serves a critical role in chemical imaging *in vivo,* protecting the sensing dyes from direct interactions with large protein or enzyme molecules, as well as by its specific targeting ability. The nanoparticles can also be incorporated with other therapeutic agents (i.e., chemotherapy and/or photo-activated therapy), in addition to its sensing capability, thus turning into multifunction *theranostic* nanoparticles.

4.4 Methods

Chemicals

All chemicals were purchased from Sigma Aldrich or ThermoFisher Scientific unless otherwise noted.

Synthesis of G2-PAA NP and F3 surface modification

The Oxyphor G2 (4 mg) was conjugated with one of the monomers, 3-(aminopropyl)methacrylamide hydrochloride salt (APMA, 53.6 mg), through carbodiimide crosslinking chemistry by stirring with 1-Ethyl-3-(3-dimethylaminopropyl)carbodiimide (EDC, 2.9 mg or 6.5 mg) and Sulfo-*N*-hydroxysuccinimide (Sulfo-NHS, 8.22 mg or 18.5 mg) in Phosphate Buffered Saline (PBS, pH 7.4, 1.3 mL). Acrylamide (689.5 mg) was added into the mixture and stirred for 2 hrs in room temperature. Then, the crosslinker, 3-(Acryloyloxy)-2-hydroxypropyl methacrylate (AHM, 321.3 mg) was added and vortexed to complete the monomer solution. The monomer solution was added and emulsified in a surfactant solution of AOT (1.6g) and Brij L4 (3.3 mL) in Hexane (45 mL). The polymerization was initiated by addition of N,N,N′,N′-tetramethylethylenediamine (TEMED) (100 μL) and 10% (w/w) Ammonium Persulfate (100 μL). The unreacted APMA provides primary amines used for later surface modification. The reaction was allowed to stir for 2 hours and hexane was removed by rotary evaporation. The prepared nanoparticles were washed with ethanol and water with Amicon Filter Cell using a 300 kDa filter, and then lyophilized. Although slight leaching of the dye was observed initially, during purification, there was no leaching during further steps of the synthesis. The surface of the SNARF-PAA NP was PEGylated and conjugated with tumor homing F3

peptides, following previous protocols[64]. The cancer targeting capability of our PAA NPs conjugated with F3 peptides has been extensively studied[65-67]. Bi-functional Polyethylene Glycol (MAL-PEG-SCM, 2kDa, Creative PEGWorks) (4 mg) was added into G2-PAA NP in PBS (pH 7.4) (50 mg per 2.5mL). After 30 min of stirring, it was washed with PBS using Amicon Ultra Centrifugal Filter (100 kDa) and F3 Peptide (KDEPQRRSARLSAKPAPPKPEPKPKKAPAKKC, RS Synthesis) (11mg) was added and stirred overnight. Cysteine (0.63 mg) was added and stirred for 2 hours to deactivate unreacted maleimide groups. The NP solution was washed with water and lyophilized. The SNARF-PAA NP was characterized by UV-VIS spectroscopy (UV-1601 Spectrometer, Shimadzu), fluorescence spectroscopy (FluoroMax-3, Horiba), and Dynamic Light Scattering instrument (DLS, Delsa Nano C particle analyzer instrument, Beckman Coulter).

In vitro PALT calibration setup

G2-PAA NP (5mg/ml in PBS) solution was stored in a vial in continuous flow into an optically clear polyvinyl chloride tube (I.D. x O.D. = 1/16 in. x 1/8 in.) using a peristaltic pump sealed with rubber septum. A needle type oximeter (Microx TX3, Presens) was inserted directly into the NP solution and used to monitor oxygen concentrations for the calibration. The oxygen concentration was controlled by bubbling nitrogen or nitrogen/air mixture. It is important not to bubble during the measurements since bubbles might be introduced to the tube causing high noises.

An optical parametric oscillator (Surelite OPO plus, Continuum) pumped with the second harmonic of a pulsed neodymium-doped aluminum garnet (Nd: YAG) laser generated the pump

beam at 630 nm. Another optical parametric oscillator laser (Vibrant B, Opotek) generated pulsed beam at 920 nm. The two laser beams were overlapped onto the tube while triggers of the two lasers were controlled by a delay generator (DG535, Standford Research Systems). PA signals were collected using cylindrically focused ultrasound transducer (V312, Panametrics). PA signals from probe beam excitations at different delay times between pump and probe beams (5 μs, 10 μs, 15 μs, 20 μs, 25 μs, and 30 μs) were collected. The probe PA signal intensities were extracted by subtracting pump only excitation and probe only excitation from pump and probe excitation. The extracted PA signals were used to fit into exponential decay curve.

PALT imaging setup

The laser setup was similar to *in vitro* PALT setup. Laser light was allowed to cover the entire imaging region. PA imaging *in vivo* was performed using our US and PA dual imaging system built on a commercially available research US platform (V1, Verasonics, Redmond, WA) and a linear array probe working at a central frequency of 11.25 MHz (CL15-7, Philips, Andover, MA,). The details of this imaging system have been introduced in our former publication[68]. Powered by a GPU card, this dual-modality system can acquire PA and US images from the same sample at the same time, both in real-time fashion with a frame rate of 10 Hz (i.e. the laser pulse repetition rate).

PALT imaging of G2-PAA NP *in vivo*

All the procedures on live animals were approved by the University Committee on the Use and Care of Animals (UCUCA) of the University of Michigan (U-M). The mice were housed at

the U-M Medical School in the Unit for Laboratory Animal Medicine (ULAM). G2-PAA NP (20 mg/ml in PBS, 0.1 mL) solution was injected into the thigh of mice. Mice were anesthetized with inhalation of 1.0 – 2.0% isoflurance mixing with oxygen or oxygen/nitrogen mixture making 100%, 20%, or 10% oxygen concentration. After 20 min of inhalation of different mixtures of oxygen, PALT images were taken. The PA images from probe beam excitation were extracted by subtracting pump only excitation and probe only excitation from pump and probe excitation by pixels intensities. By computing exponential decay rates between PA images at different delay times, PALT images were prepared.

PALT imaging of G2-PAA NP *in vivo* tumor

All the procedures on live animals were approved by the University Committee on the Use and Care of Animals (UCUCA) of the University of Michigan (U-M). The mice were housed at the U-M Medical School in the Unit for Laboratory Animal Medicine (ULAM). Nude mice (5 weeks old male, Athymic nude Fox/NU, Envigo) were used. 9L rat glioma cell line (American Type Culture Collection) was cultured in RPMI 1640 medium supplemented with 10% Fetal Bovine Serum (FBS) and 1% Antibiotic-antimycotic. Approximately 10^6 cells in 100 μL of culture media were subcutaneously injected on the back of each mouse. Each tumor was allowed to grow for 2-4 weeks until its volume reached around 0.5 cc as measured using a caliper.

The nude mice were anesthetized with the inhalation of 1.0-2.0% isoflurane mixing with oxygen. The PALT images were acquired 60 min after the G2-PAA NP solution (20 mg/ml in PBS, 250 mg NP per kg body weight) tail-vein injection. PA images with 576 nm, 584 nm, 630 nm were taken in order to provide the nanoparticle accumulation images by spectral unmixing

using a similar algorithm explained previously.[58] PALT images were collected using similar method described previously.

4.5 References

1. Papkovsky, D.B. & Dmitriev, R.I. Biological detection by optical oxygen sensing. *Chemical Society Reviews* **42**, 8700-8732 (2013).
2. Ingram, J. et al. Oxygen and seizure dynamics: I. Experiments. *Journal of Neurophysiology* **112**, 205-212 (2014).
3. Wilson, W.R. & Hay, M.P. Targeting hypoxia in cancer therapy. *Nat Rev Cancer* **11**, 393-410 (2011).
4. Warburg, O. On the Origin of Cancer Cells. *Science* **123**, 309 (1956).
5. Eltzschig, H.K. & Carmeliet, P. Hypoxia and Inflammation. *The New England journal of medicine* **364**, 656-665 (2011).
6. Abdollahi, H. et al. The Role of Hypoxia in Stem Cell Differentiation and Therapeutics. *The Journal of surgical research* **165**, 112-117 (2011).
7. Wang, X. et al., Vol. 5320 69-76 (2004).
8. Wang, X., Xie, X., Ku, G., Wang, L.V. & Stoica, G. Noninvasive imaging of hemoglobin concentration and oxygenation in the rat brain using high-resolution photoacoustic tomography. *BIOMEDO* **11**, 024015-024015-024019 (2006).
9. Yao, J., Maslov, K.I., Zhang, Y., Xia, Y. & Wang, L.V. Label-free oxygen-metabolic photoacoustic microscopy in vivo. *BIOMEDO* **16**, 076003-076003-076011 (2011).
10. Jo, J. & Yang, X. Functional photoacoustic imaging to observe regional brain activation induced by cocaine hydrochloride. *BIOMEDO* **16**, 090506-090506-090503 (2011).
11. Friedrich, C.-S. et al., Vol. 8088 808814-808814-808819 (2011).
12. Alles, E.J., Papaevangelou, E. & Bamber, J.C. in 2014 IEEE International Ultrasonics Symposium 1284-1287 (2014).
13. Bayer, C.L., Wlodarczyk, B.J., Finnell, R.H. & Emelianov, S.Y. Ultrasound-guided spectral photoacoustic imaging of hemoglobin oxygenation during development. *Biomed. Opt. Express* **8**, 757-763 (2017).
14. Mathangi, S., Konstantin, M., Hao, F.Z., George, S. & Lihong, V.W. Limitations of quantitative photoacoustic measurements of blood oxygenation in small vessels. *Physics in Medicine & Biology* **52**, 1349 (2007).
15. Tzoumas, S. et al. Eigenspectra optoacoustic tomography achieves quantitative blood oxygenation imaging deep in tissues. **7**, 12121 (2016).
16. Stein, E.W., Maslov, K. & Wang, L.V. Noninvasive, in vivo imaging of blood-oxygenation dynamics within the mouse brain using photoacoustic microscopy. *BIOMEDO* **14**, 020502-020502-020503 (2009).
17. Yao, J. et al. High-speed Label-free Functional Photoacoustic Microscopy of Mouse Brain in Action. *Nature methods* **12**, 407-410 (2015).
18. Hussain, A., Petersen, W., Staley, J., Hondebrink, E. & Steenbergen, W. Quantitative blood

oxygen saturation imaging using combined photoacoustics and acousto-optics. *Opt. Lett.* **41**, 1720-1723 (2016).
19. Yin, G., Xing, D. & Yang, S. Dynamic monitoring of blood oxygen saturation in vivo using double-ring photoacoustic sensor. *Journal of Applied Physics* **106**, 013109 (2009).
20. Arthuis, C.J. et al. Real-Time Monitoring of Placental Oxygenation during Maternal Hypoxia and Hyperoxygenation Using Photoacoustic Imaging. *PLOS ONE* **12**, e0169850 (2017).
21. Rich, L.J. & Seshadri, M. Photoacoustic Imaging of Vascular Hemodynamics: Validation with Blood Oxygenation Level–Dependent MR Imaging. *Radiology* **275**, 110-118 (2015).
22. Kolkman, R.G.M., Steenbergen, W. & van Leeuwen, T.G. In vivo photoacoustic imaging of blood vessels with a pulsed laser diode. *Lasers in Medical Science* **21**, 134-139 (2006).
23. Fainchtein, R., Stoyanov, B.J., Murphy, J.C., Wilson, D.A. & Hanley, D.F., Vol. 3916 19-33 (2000).
24. Zhang, H.F., Maslov, K., Sivaramakrishnan, M., Stoica, G. & Wang, L.V. Imaging of hemoglobin oxygen saturation variations in single vessels in vivo using photoacoustic microscopy. *Applied Physics Letters* **90**, 053901 (2007).
25. Saha, R.K., Karmakar, S. & Roy, M. Assessment of blood oxygen saturation using photoacoustic technique. *Journal of Optics* **42**, 141-147 (2013).
26. Petri, M. et al. Photoacoustic imaging of real-time oxygen changes in chronic leg ulcers after topical application of a haemoglobin spray: a pilot study. *Journal of Wound Care* **25**, 87-91 (2016).
27. Valluru, K.S. & Willmann, J.K. Clinical photoacoustic imaging of cancer. *Ultrasonography* **35**, 267-280 (2016).
28. Hennen, S.N. et al. Photoacoustic tomography imaging and estimation of oxygen saturation of hemoglobin in ocular tissue of rabbits. *Experimental Eye Research* **138**, 153-158 (2015).
29. Luis Dean-Ben, X. & Razansky, D. Adding fifth dimension to optoacoustic imaging: volumetric time-resolved spectrally enriched tomography. *Light Sci Appl* **3**, e137 (2014).
30. Wang, X. et al. Noninvasive laser-induced photoacoustic tomography for structural and functional in vivo imaging of the brain. *Nat Biotech* **21**, 803-806 (2003).
31. Zhang, H.F., Maslov, K., Stoica, G. & Wang, L.V. Functional photoacoustic microscopy for high-resolution and noninvasive in vivo imaging. *Nat Biotech* **24**, 848-851 (2006).
32. Herzog, E. et al. Optical Imaging of Cancer Heterogeneity with Multispectral Optoacoustic Tomography. *Radiology* **263**, 461-468 (2012).
33. Lin, L., Yao, J., Li, L. & Wang, L.V. In vivo photoacoustic tomography of myoglobin oxygen saturation. *BIOMEDO* **21**, 061002 (2016).
34. Jubran, A. Pulse oximetry. *Critical Care* **19**, 272 (2015).
35. Jobsis, F. Noninvasive, infrared monitoring of cerebral and myocardial oxygen sufficiency and circulatory parameters. *Science* **198**, 1264-1267 (1977).
36. Ashkenazi, S., Huang, S.-W., Horvath, T., Koo, Y.-E.L. & Kopelman, R. Photoacoustic probing of fluorophore excited state lifetime with application to oxygen sensing. *BIOMEDO* **13**, 034023-034023-034024 (2008).
37. Shao, Q. & Ashkenazi, S. Photoacoustic lifetime imaging for direct in vivo tissue oxygen monitoring. *BIOMEDO* **20**, 036004-036004 (2015).
38. Shao, Q., Biel, M.A. & Ashkenazi, S., Vol. 8931 89310H-89310H-89318 (2014).
39. Shao, Q., Morgounova, E. & Ashkenazi, S., Vol. 8943 89430F-89430F-89436 (2014).

40. Shao, Q. et al. In vivo photoacoustic lifetime imaging of tumor hypoxia in small animals. *BIOMEDO* **18**, 076019-076019 (2013).
41. Ashkenazi, S. Photoacoustic lifetime imaging of dissolved oxygen using methylene blue. *BIOMEDO* **15**, 040501-040501-040503 (2010).
42. Shao, Q., Morgounova, E. & Ashkenazi, S., Vol. 9323 932320-932320-932324 (2015).
43. Morgounova, E., Shao, Q., Hackel, B.J., Thomas, D.D. & Ashkenazi, S. Photoacoustic lifetime contrast between methylene blue monomers and self-quenched dimers as a model for dual-labeled activatable probes. *BIOMEDO* **18**, 056004 (2013).
44. Forbrich, A., Shao, P., Shi, W. & Roger, J.Z. Lifetime-weighted photoacoustic imaging. *Journal of Optics* **18**, 124001 (2016).
45. Jo, J., Lee, C.H., Kopelman, R. & Wang, X. Lifetime-resolved Photoacoustic (LPA) Spectroscopy for monitoring Oxygen change and Photodynamic Therapy (PDT). *Proc SPIE Int Soc Opt Eng* **9708** (2016).
46. Ray, A., Rajian, J.R., Lee, Y.-E.K., Wang, X. & Kopelman, R. Lifetime-based photoacoustic oxygen sensing in vivo. *BIOMEDO* **17**, 0570041-0570044 (2012).
47. Rajendran, J.G. & Krohn, K.A. Imaging hypoxia and angiogenesis in tumors. *Radiologic Clinics* **43**, 169-187.
48. Potter, M., Badder, L., Hoade, Y., Johnston, I.G. & Morten, K.J. in Oxygen Transport to Tissue XXXVII. (eds. C.E. Elwell, T.S. Leung & D.K. Harrison) 257-263 (Springer New York, New York, NY; 2016).
49. Shao, Q., Biel, M.A. & Ashkenazi, S. in Proceedings of SPIE, Vol. 8931 89310H-89310H-89318 (2014).
50. Shao, Q., Morgounova, E. & Ashkenazi, S. in Proceedings of SPIE, Vol. 8943 89430F-89430F-89436 (2014).
51. Shao, Q., Morgounova, E. & Ashkenazi, S. in Proceedings of SPIE, Vol. 9323 932320-932320-932324 (2015).
52. Koo, Y.-E.L. et al. Brain cancer diagnosis and therapy with nanoplatforms. *Advanced Drug Delivery Reviews* **58**, 1556-1577 (2006).
53. Clark, H., Kopelman, R. & Barker, S. in Biomedical Diagnostic Science (CRC Press, 2002).
54. Brasuel, M. et al. in Optical Biosensors 497-536 (Elsevier Science, Amsterdam; 2002).
55. Yong-EunKooLee, EricMonson, MurphyBrasuel, MartinAPhilbert & Kopelman, R. in Biomedical Photonics Handbook, Second Edition 555-574 (CRC Press, 2014).
56. Gupta, A. et al. Multifunctional Nanoplatforms for Fluorescence Imaging and Photodynamic Therapy Developed by Post-loading Photosensitizer and Fluorophore to Polyacrylamide Nanoparticles. *Nanomedicine : nanotechnology, biology, and medicine* **8**, 941-950 (2012).
57. Avula, U.M.R. et al. Cell-selective arrhythmia ablation for photomodulation of heart rhythm. *Science Translational Medicine* **7**, 311ra172 (2015).
58. Jo, J., Lee, C.H., Kopelman, R. & Wang, X. In vivo quantitative imaging of tumor pH by nanosonophore assisted multispectral photoacoustic imaging. *Nature Communications* **8**, 471 (2017).
59. Koo Lee, Y.-E. et al. Near Infrared Luminescent Oxygen Nanosensors with Nanoparticle Matrix Tailored Sensitivity. *Analytical Chemistry* **82**, 8446-8455 (2010).
60. Lee, C.H. et al. Ion-Selective Nanosensor for Photoacoustic and Fluorescence Imaging of Potassium. *Analytical Chemistry* **89**, 7943-7949 (2017).

61. Sasaki, K., Shi, Z.-Y., Kopelman, R. & Masuhara, H. Three-Dimensional pH Microprobing with an Optically-Manipulated Fluorescent Particle. *Chemistry Letters* **25**, 141-142 (1996).
62. Koo, Y.-E.L. et al. Real-Time Measurements of Dissolved Oxygen Inside Live Cells by Organically Modified Silicate Fluorescent Nanosensors. *Analytical Chemistry* **76**, 2498-2505 (2004).
63. Xu, H., Aylott, J.W. & Kopelman, R. Fluorescent nano-PEBBLE sensors designed for intracellular glucose imaging. *Analyst* **127**, 1471-1477 (2002).
64. Nie, G. et al. Hydrogel nanoparticles with covalently linked coomassie blue for brain tumor delineation visible to the surgeon. *Small* **8**, 884-891 (2012).
65. Orringer, D.A. et al. In vitro characterization of a targeted, dye-loaded nanodevice for intraoperative tumor delineation. *Neurosurgery* **64**, 965-971; discussion 971-962 (2009).
66. Winer, I. et al. F3-targeted cisplatin-hydrogel nanoparticles as an effective therapeutic that targets both murine and human ovarian tumor endothelial cells in vivo. *Cancer Res* **70**, 8674-8683 (2010).
67. Nie, G. et al. Hydrogel nanoparticles with covalently linked coomassie blue for brain tumor delineation visible to the surgeon. *Small* **8**, 884-891 (2012).
68. Yuan, J. et al. Real-time photoacoustic and ultrasound dual-modality imaging system facilitated with graphics processing unit and code parallel optimization. *J Biomed Opt* **18**, 86001 (2013).

Chapter 5: Summary and Future Directions

5.1 Summary

Nanoparticle research has been mostly focused on therapy rather than diagnostics. We believe that understanding the chemical information of tumors can guide a more accurate selection of treatments for each patient, and moreover, each tumor. Chemical information can guide us to our ultimate therapeutic goal, personalized medicine. Most common treatments for cancer include chemotherapy (affected by pH), radiation therapy (affected by O_2), and immunotherapy (affected by K^+). Here, some of the most recent advances regarding photoacoustic chemical imaging of each of the three analytes are introduced.

In Chapter 2, the first demonstration of quantitative photoacoustic pH imaging is introduced, having been recently published in *Nature Communications*.[1] Tumor acidosis, as a consequence of increased fermentative metabolism and poor perfusion, plays an important role in almost all steps of invasive growth and metastasis. Successful measurements of the extracellular pH of the tumor microenvironment can contribute to the clinical management of cancer as well as to basic research. We reported on an *in vivo* tumor pH mapping nanotechnology that includes the development of tumor-targeted, pH sensing nanoprobes, "nanosonophores", and multi-wavelength photoacoustic imaging (PAI) integrated with ultrasound imaging. The optical pH indicator, SNARF-5F, i.e., 5-(and-6)-Carboxylic Acid, was encapsulated into polyacrylamide nanoparticles with surface modification for tumor targeting. Protected by the polyacrylamide nanomatrix, the pH indicator's

optical performance is not affected by proteins or enzymes, making possible the quantitative assessment of tumor pH in vivo. Facilitated by the multi-wavelength PAI plus spectral unmixing technique, the accuracy in measuring the pH is not susceptible to the background optical absorption of hemoglobin. As a result, both the pH levels and the hemodynamic properties in the entire tumor can be quantitatively evaluated, with high sensitivity and with high spatial resolution. The experiments on precisely-controlled phantoms validated the accuracy and robustness of this pH imaging technology, while experiments on a mouse cancer model demonstrated its good performance in vivo. The statistical analysis shows that the average pH levels quantified in the tumors were significantly lower than those in normal tissue, which was also confirmed by measurements via an invasive pH electrode used as a gold standard.

In Chapter 3, the first photoacoustic and fluorescence optimized potassium sensor was described, which has recently been published in *Analytical Chemistry*.[2, 3] Notably, ion selective optical nanosensors allow highly selective and accurate ion measurements in biological systems, without the physical limitations imposed by the use of ion selective electrodes. We reported the first example of a potassium selective nanosensor optimized for photoacoustic (PA) as well as fluorescence imaging. This potassium selective nanosensor (K^+ NS) shows excellent response in the extracellular range, from 0 to 100 mM, as confirmed by both UV-Vis Spectroscopy and PA Spectroscopy, while also showing excellent response in the intracellular range, from 20 mM to 100 mM, as confirmed by fluorescence spectroscopy. Furthermore, thi K^+ PEBBLE showed a 2 orders of magnitude, or higher, selectivity to K^+, relative to any other cations, such as Na^+, Ca^{2+}, and Mg^{2+}. Notably, this example of a biological ion selective PA sensor can be easily applied to other biologically relevant ions, cations and anions (e.g., sodium, magnesium, calcium, chloride and nitrite), based on the standard principles of ion selective optodes, and thus to their utilization

for *in vivo* biological ion imaging.

In Chapter 4, some of the initial studies of photoacoustic lifetime (PALT) O_2 imaging were introduced. PALT imaging is based on transient absorption spectroscopy, using a phosphorescence quenching based oxygen sensor. The sensor can be incorporated into nanoparticles, thus granting targetability and protection of the sensing dye. A known PALT and phosphorescence quenching oxygen indicator, Oxyphor G2, is conjugated onto polyacrylamide nanoparticles (G2-PAA NP). The surface of the nanoparticle is further modified with the tumor homing F3-peptide. The oxyphor G2 is protected by the nanoparticle matrix, thus granting minimal interaction with human serum albumin, the most abundant protein in the body. The optical property of the dye, upon interaction with human serum albumin, would vary significantly. This innate oxygen sensing capability of G2-PAA NP was tested both *in vitro* and *in vivo*.

5.2 Future directions for pH imaging

For current diagnostics settings, the patients are first diagnosed through structural imaging (MRI, X-ray, PET, etc.). If doctors are suspicious of encountering a tumor in certain areas, the patient's cancer is then confirmed through tissue biopsy. We envision that our quantitative pH imaging can replace the biopsy step. The NP can be injected to the patients and the quantified pH images can be provided within a day. The biomedical community already extensively studied pH in the normal body and found that the pH levels everywhere in the body are very strictly controlled. Also, if the NPs are accumulated into the suspected tumor's tissue that would also provide a secondary proof that the suspicious tissue is in fact cancer. NPs can accumulate into tumors through both passive (EPR effect) and active targeting (F3 peptide in our studies, but can be replaced by

any other targeting moieties).

Another direction we plan to study is the role of pH in relation to tumor metastasis. Essentially every tumor has different pH levels and this is often the tumor's main characteristics. The more aggressive tumor may be smaller than the less aggressive tumor, but those aggressive tumors can be more acidic than other tumors. Because we can gather quantitative pH information, we can possibly, in the future, provide a statistical analysis on the relation between tumor pH and the tumor's metastatic potential. Acidic pH can also influence the tumor's resistance to chemotherapy, by up regulating the expression of p-glycoprotein, which increases drug efflux.[4] There are other types of cancer drugs such as camptothecin, topotecan, and irinotecan, which are inactive at physiological pH and only become active at acidic pH. Gathering information on its pH can provide a precise selection of therapies that would be most effective for certain patients (also known as "precision medicine").

There are some of the technical limitations that need to be overcome. First, SNARF-5F is a dye that cannot be directly conjugated onto the nanoparticles. Thus, loading of the dye is limited. Higher loading can be highly beneficial potentially lowering injection dose. For imaging technique, the quantitative pH imaging can only be done up to 6 mm in depth due to the local fluence differences of different wavelengths. Another function, which estimates the fluence difference in muscle tissues, can be introduced to further increase the quantitative imaging depth limit. Another potential approach to enhance imaging depth is by replacing SNARF-5F with a different near infrared absorbing pH indicators.

5.3 Future directions for K^+ imaging

One of the most urgent directions for PA K^+ imaging is to demonstrate it *in vivo*. To the best of our knowledge, there has not been an *in vivo* PA K^+ imaging. However, there is a technical limitation imposed to the current sensor. The K^+ NS is also sensitive to pH changes. Its calibration curve can be shifted slightly even with a 0.5 pH difference. The ion selective optodes essentially use pH indicators (chromoionophores) as the detection method; thus, influence of pH cannot be neglected in ion selective optodes, including the K^+ NS. As introduced in this thesis, pH levels of the tumor are not consistent, which brings complication to quantification. Typical pH values in tumor models we have tested are higher than pH 6.6; thus, a new potassium sensor, which shows consistent calibration at pH values ranging from 6.6 to 7.4, should be prepared.

Another interesting application would be in observing electrical cellular activity. Optical based chemical analysis methods provide a way to observe such cellular activity without the physical limitations imposed by electrodes. Most commonly used to monitor membrane potential are voltage-sensitive indicator dyes. However, the limitations preventing using voltage-sensitive dyes for *in vivo* studies are[5]:

1. When administered intravenously, the dyes do not have specific binding, or so called "targeting" ability to target the specific cells.

2. Most voltage-sensitive dyes exhibit significant toxicity.

3. Most voltage-sensitive dyes use short wavelengths (<600 nm) of light, which limits deep tissue light penetration.

Most voltage-sensitive dyes measure the electrochromic effect, also known as the Stark shift effect.

It is detected by a fluorescence emission change; however, fluorescence imaging has limited use *in vivo* due to the light penetration depth limit, even with longer wavelength light, because of the need to detect the light (emission) that emanates back from the response area. It is possible to overcome the light penetration depth limit of the conventional fluorescence imaging modality by applying photoacoustic (PA) Imaging.[6]

As an alternative to using voltage-sensitive dyes, ion concentration gradients can be measured in order to gather cellular activity information. Membrane potentials, or "action potentials", are generated by voltage-gated ion channels as the nerve cells or muscle cells maintain the homeostasis of ion concentration within the cells.[7] Overcoming the physical limitations and invasiveness of ion selective electrodes, ion selective nanoparticles (nanosensors) can be delivered non-invasively and enable real-time monitoring.[8-10] Ion-selective nanoparticles are essentially similar to ion-selective electrodes, where the membrane of the electrode is supplanted by the surface medium of the nanoparticle. Molecular sensors can be incorporated into their polymer matrix medium which serves to protect the molecular sensors from degradation and enables targeting a cancer or other specific tissue by conjugating a cell-targeting moiety onto the surface of the matrix.[2, 11]

5.4 Future directions for O_2 imaging

Although some of the initial studies have been shown in this thesis, there are still more experiments left to be done in order to conclude the story. The *in vivo* experiments presented need to be repeated (currently, n=2) to validate our findings and acquire statistical significance, along with some supporting *in vitro* and *ex vivo* experiments. For example, it is important to confirm that the technique is nanoparticle concentration independent, since the nanoparticles are spread

unevenly throughout the imaging region.

A side product of PALT is the production of reactive oxygen species (ROS, including singlet oxygen, superoxide, H_2O_2, etc.). This mechanism is actually also shared with photodynamic therapy (PDT). PDT is a therapeutic modality, which was originally developed for cancer treatment and later extended to different diseases such as bacterial and viral infections as well as cardiac arrhythmia.[12-19] Photosensitizers receive light energy, which is transferred into nearby O_2 molecules, so as to produce ROS. The excess ROS causes oxidative stress within the cell, leading to cell death. PDT is a highly selective therapeutic modality which requires spatial and temporal concomitance of all 3 components (light, photosensitizer, and O_2). During PDT, the molecular O_2 is essentially consumed. PALT has thus the potential to be combined with PDT so as to enable real-time therapeutic monitoring, thereby acquiring a *theranostic* operation, for therapy guidance, towards the ultimate therapeutic goal of personalized medicine (Fig 10).[20-22] An initial study of this application is introduced in the Appendix section.

PALT can also be applied to different analytes, such as glucose. We have previously used optical oxygen sensing nanoparticles for intracellular glucose measurements.[23] The nanosensor was composed of a polyacrylamide based nanoparticle containing an oxygen sensitive fluorescence indicator ($Ru[dpp(SO_3Na)_2I_3)Cl_2$), an oxygen insensitive reference fluorescence dye, and glucose oxidase. Glucose oxidase catalyzes oxidation of glucose to produce D-gluconolactone, which hydrolyzes into D-gluconic acid. The oxidation results in a local depletion of oxygen, which can be detected by the oxygen indicator.

5.5 References

1. Jo, J., Lee, C.H., Kopelman, R. & Wang, X. In vivo quantitative imaging of tumor pH by

nanosonophore assisted multispectral photoacoustic imaging. *Nature Communications* **8**, 471 (2017).
2. Lee, C.H. et al. Ion-Selective Nanosensor for Photoacoustic and Fluorescence Imaging of Potassium. *Analytical Chemistry* **89**, 7943-7949 (2017).
3. Lee, C.H. et al. Correction to Ion-Selective Nanosensor for Photoacoustic and Fluorescence Imaging of Potassium. *Analytical Chemistry* (2017).
4. Kato, Y. et al. Acidic extracellular microenvironment and cancer. *Cancer Cell International* **13**, 89 (2013).
5. Peterka, D.S., Takahashi, H. & Yuste, R. Imaging Voltage in Neurons. *Neuron* **69**, 9-21 (2011).
6. Wang, L.V. Multiscale photoacoustic microscopy and computed tomography. *Nat Photon* **3**, 503-509 (2009).
7. Bean, B.P. The action potential in mammalian central neurons. *Nat Rev Neurosci* **8**, 451-465 (2007).
8. Brasuel, M., Kopelman, R., Miller, T.J., Tjalkens, R. & Philbert, M.A. Fluorescent Nanosensors for Intracellular Chemical Analysis: Decyl Methacrylate Liquid Polymer Matrix and Ion-Exchange-Based Potassium PEBBLE Sensors with Real-Time Application to Viable Rat C6 Glioma Cells. *Analytical Chemistry* **73**, 2221-2228 (2001).
9. Xie, X., Zhai, J. & Bakker, E. pH Independent Nano-Optode Sensors Based on Exhaustive Ion-Selective Nanospheres. *Analytical Chemistry* **86**, 2853-2856 (2014).
10. Buck, S.M., Xu, H., Brasuel, M., Philbert, M.A. & Kopelman, R. Nanoscale probes encapsulated by biologically localized embedding (PEBBLEs) for ion sensing and imaging in live cells. *Talanta* **63**, 41-59 (2004).
11. Byrne, J.D., Betancourt, T. & Brannon-Peppas, L. Active targeting schemes for nanoparticle systems in cancer therapeutics. *Advanced Drug Delivery Reviews* **60**, 1615-1626 (2008).
12. Dolmans, D.E.J.G.J., Fukumura, D. & Jain, R.K. Photodynamic therapy for cancer. *Nat Rev Cancer* **3**, 380-387 (2003).
13. Avula, U.M.R. et al. Cell-selective arrhythmia ablation for photomodulation of heart rhythm. *Science Translational Medicine* **7**, 311ra172 (2015).
14. Yoon, H.K. et al. Nanophotosensitizers Engineered to Generate a Tunable Mix of Reactive Oxygen Species, for Optimizing Photodynamic Therapy, Using a Microfluidic Device. *Chemistry of Materials* **26**, 1592-1600 (2014).
15. Tang, W., Xu, H., Kopelman, R. & Philbert, M.A. Photodynamic Characterization and In Vitro Application of Methylene Blue-containing Nanoparticle Platforms¶. *Photochemistry and Photobiology* **81**, 242-249 (2005).
16. Qin, M. et al. Methylene blue covalently loaded polyacrylamide nanoparticles for enhanced tumor-targeted photodynamic therapy(). *Photochemical & photobiological sciences : Official journal of the European Photochemistry Association and the European Society for Photobiology* **10**, 832-841 (2011).
17. Dougherty, T.J. & Gomer, C.J. Introduction. *Lasers in Surgery and Medicine* **43**, 541-541 (2011).
18. Bernstein, Z.P. et al. Photopheresis in HIV-1 Infected Patients Utilizing Benzoporphyrin Derivative (BPD) Verteporfin and Light. *Current HIV Research* **6**, 152-163 (2008).
19. Gupta, A. et al. Multifunctional Nanoplatforms for Fluorescence Imaging and

Photodynamic Therapy Developed by Post-loading Photosensitizer and Fluorophore to Polyacrylamide Nanoparticles. *Nanomedicine : nanotechnology, biology, and medicine* **8**, 941-950 (2012).
20. Shao, Q., Biel, M.A. & Ashkenazi, S. in Proceedings of SPIE, Vol. 8931 89310H-89310H-89318 (2014).
21. Shao, Q., Morgounova, E. & Ashkenazi, S. in Proceedings of SPIE, Vol. 9323 932320-932320-932324 (2015).
22. Jo, J., Lee, C.H., Kopelman, R. & Wang, X. Lifetime-resolved Photoacoustic (LPA) Spectroscopy for monitoring Oxygen change and Photodynamic Therapy (PDT). *Proc SPIE Int Soc Opt Eng* **9708** (2016).
23. Xu, H., Aylott, J.W. & Kopelman, R. Fluorescent nano-PEBBLE sensors designed for intracellular glucose imaging. *Analyst* **127**, 1471-1477 (2002).

Appendix A

Monitoring photodynamic therapy (PDT) using photoacoustic lifetime based oxygen sensing

This section has been adapted from a following conference paper with modifications and updates:

Jo, J.[1]; **Lee, C. H.[1]**; Kopelman, R.; Wang, X., "Lifetime-resolved photoacoustic (LPA) Spectroscopy for Monitoring Oxygen Change and Photodynamic Therapy (PDT)", *Proc. SPIE,* 9708, Photons Plus UltrasoundL Imaging and Sensing, 97081L, **2016**. [1]Indicates co-first authorship

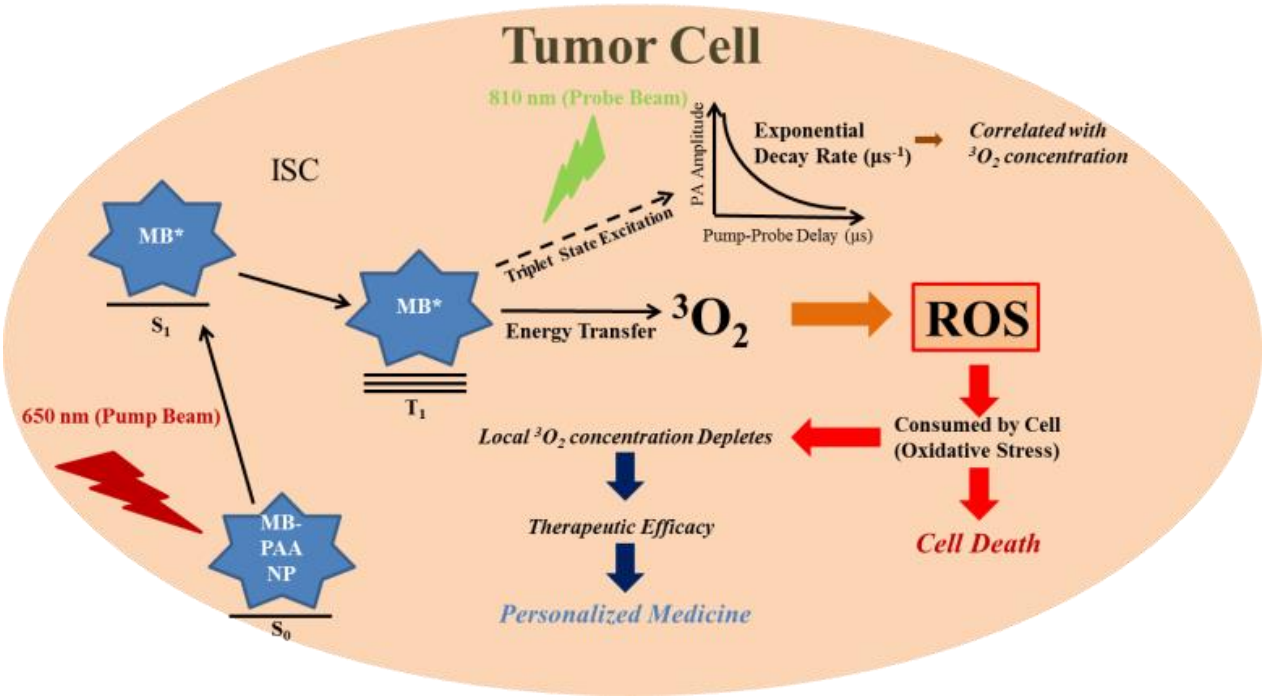

Figure A.0 Graphical abstract

A.1 Introduction

Photodynamic therapy (PDT) is a promising therapeutic modality for various tumors[1-5]. It is a highly targeted/local treatment, as the illumination is localized to the target tissue, with a certain wavelength of light used to excite a photosensitizer (PS) so as to convert the local ground state oxygen ($^3O_2$) molecules into cytotoxic reactive oxygen species (ROS). The ROS cause oxidative stress within the cells, inducing cell death by apoptosis, necrosis or a combination thereof [1-5]. Upon light excitation, the PS molecule's excited singlet state, through internal conversion and intersystem crossing, quickly relaxes to the excited triplet state of the PS. The emission from this triplet state (phosphorescence) is typically slow, due to its being a quantum mechanically

forbidden process, requiring a change in electronic spin state [1-5]. As a result, the excited PS state lifetime is long enough to allow quenching by collisional interaction with nearby $^3O_2$ molecules, thus creating $^1O_2$ and other ROS. PDT's advantages over conventional therapies are: (1) having minimal long-term toxicity effects, (2) enabling highly selective localized treatments by the focused laser beam, (3) enabling repeated treatments at the same site, and (4) presenting a significantly lower risk of side effects, compared to surgery, chemotherapy or ionizing radiation treatments. In addition, PDT can be employed to virtually any type of cancer. Numerous worldwide clinical trials have shown PDT as an effective and safe modality for various cancers [1-3]. Due to the increased attention to PDT, researchers have been interested in optimizing nanophotosensitizers, which have the potential to increase efficiency, targetability (with double targeting enabled by the focused laser beam and by the nanoparticle navigation of the PSs), and biocompatibility [4, 5]. Having developed *nanophotodynamics*, i.e. nano-enabled PDT [6-11], as well as Photoacoustic oxygen sensing via the method of PhotoAcoustic LifeTime (PALT) measurement [12-15], we here combine the two methods for achieving the added potential of personalized theranostic (therapeutic plus diagnostic) operation, i.e. precision medicine.

Methylene Blue (MB) is a promising candidate for working as a dual PS-oxygen-activator/sensor, due to its high triplet quantum yield (~0.5), enabling efficient energy transfer to oxygen and thus leading to high efficacy PDT. Moreover, MB has Near Infrared absorption wavelength (λ_{max} = 664 nm in aqueous media), allowing deeper tissue penetration [16]. The feasibility of MB oxygen sensing has already been explored previously [13, 14]. However, MB in free molecule form has only limited use *in vivo*, because the MB molecules, without being

protected, get reduced into PDT inactive, colorless isomeric molecules (*leuko*-MB) by blood enzymes [6, 8, 16]. Also, at higher concentrations, MB molecules may form aggregates that reduce their luminescence quantum yield, due to "self-quenching", leading to a decrease in PDT efficiency [8, 9, 16]. Furthermore, MB molecules cannot specifically target tumors when intravenously injected. In some of our previous works, MB loaded polyacrylamide nanoparticles (MB-PAA NP) have been developed, using several different methods to maximize their PDT efficacy [6-10]. Notably, the PAA matrix protects the MB molecules from the blood enzymes, thus avoiding isomerization of MB into *leuko*-MB. According to our previous measurements, in the presence of reducing enzymes, over 80% of the free floating MB molecules' fluorescence disappears after 1 hr; however, only less than 10% of the MB-PAA NP fluorescence disappears under the same condition [6]. Also, the amine functionalized PAA NPs enable surface functionalization, for attachment of tumor targeting moieties, such as the F3 tumor homing peptide, via conjugation with bi-functional polyethylene glycol, thus navigating the MB PS specifically to and into the tumor cells [7, 10, 17-19].

Oxygen depletion during PDT has been studied previously, and its relevance for PDT efficacy and its effects on tumor survival have been monitored very closely [20-22]. However, most experiments were performed using secondary probes, such as hypoxia markers [21]. The others involved the sticking-in of invasive oxygen sensing electrodes [23]. Presently, there is still not a good way for non-invasive monitoring of oxygen depletion during PDT, and in real-time fashion. PA imaging is a non-invasive imaging technique, using only non-ionizing light and external ultrasound detectors. One of the greatest advantages of PA imaging, for both structural and chemical imaging, compared to conventional fluorescence, is the deeper tissue penetration capability, meaning better

feasibility for *in vivo* studies. The PALT system uses two laser beams: a "pump" beam and a "probe" beam. Upon the photon pump-beam excitation, an oxygen indicator dye molecule's excited singlet state undergoes internal conversion and intersystem crossing, quickly relaxing to the excited triplet state. The PA signal induced by the probe beam measures the molecule's *transient absorption* (T_1 to T_n) of the excited triplet state. By changing the time delay between the pump and probe beams, exponential decay curves of the PA amplitudes are derived from the probe beam. *This exponential decay rate of the PS in the excited state correlates directly with the oxygen concentration in the medium*, as the oxygen quenching is a pseudo-first-order chemical reaction.

Hereby we demonstrate a *personalized theranostics* method, aimed at precision cancer medicine, by combining PDT and PALT oxygen sensing. The MB-PAA NP itself has a unique capability of enabling both nano-PDT and $^3O_2$ monitoring. It may not only perform separately PDT and $^3O_2$ monitoring, but can also be used to study the PDT efficacy, by simultaneous *in situ* $^3O_2$ depletion monitoring, through PALT measurement. This new method should allow one to determine, in a non-invasive manner, *in vivo,* the correct drug/light dosage (i.e. therapeutic window) for different types of cancers and for individual patients, as needed for *precision medicine*.

A.2 Results and discussion

Characterization of MB loaded polyacrylamide nanoparticles (MB-PAA NPs)

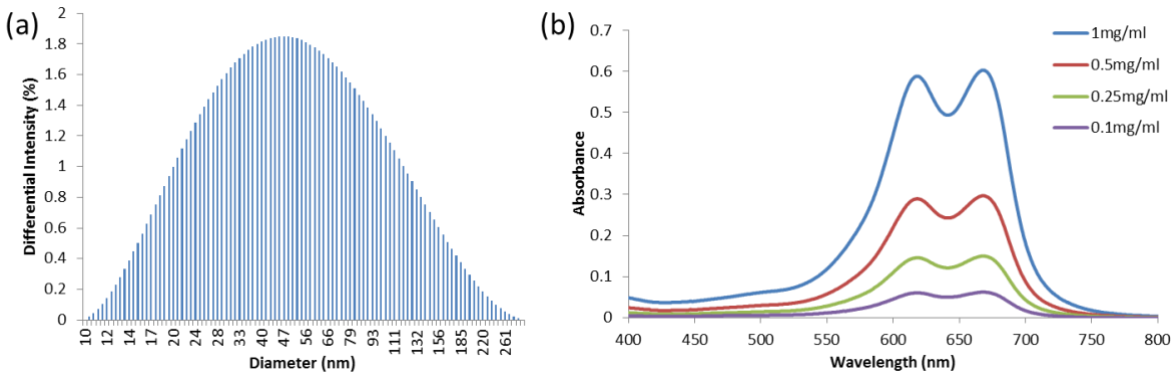

Figure A.1 (a) DLS of MB-PAA NPs (b) UV-Vis absorption spectra of MB-PAA NPs in PBS pH 7.4 buffer.

MB-PAA NPs were synthesized as previously described [6]. Dynamic Light Scattering measurements were taken to determine the hydrodynamic size of the MB-PAA NPs. The average size distribution was 73.7 nm (±6.8 nm) (**Figure A.1a**). The hydrodynamic size of the MB-PAA NPs is also optimal for *passive targeting* of cancer (10 nm to 100 nm) [4, 24]. The MB-PAA NPs exhibit absorption maxima at 669 nm and 619 nm, as previously reported [6]. The peak at 669 nm corresponds to the MB monomer peak while the peak at 619 nm corresponds to the aggregated MB dimer peak.[6, 16] The dimer and monomer absorption ratio stays constant at different concentrations of the MB-PAA NPs; thus, the solvent does not play a critical role in the aggregation of the MB embedded inside the MB-PAA NPs, as shown in **Figure A.1b**.

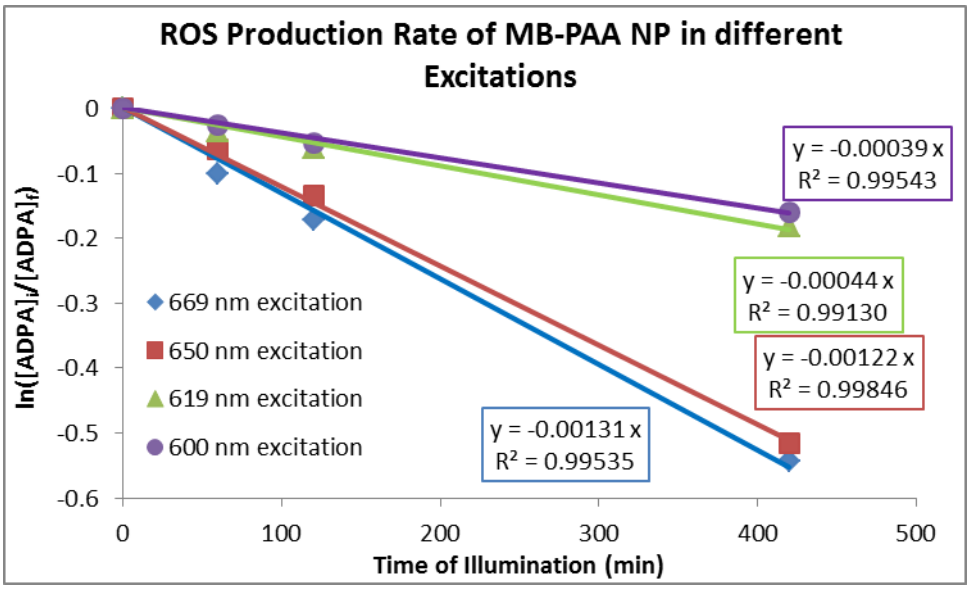

Figure A.2 The *k* value determination of ROS production by MB-PAA NPs with different excitation wavelengths. $[ADPA]_i$ indicates the initial ADPA fluorescence and $[ADPA]_f$ indicates the ADPA fluorescence after quenching by ROS.

The ROS production (photo-cytotoxicty) of the MB-PAA NPs was measured by using the ROS quenchers, ADPA, and their fluorescence *decay kinetics*.[6, 9, 25] As pointed out, the ADPA fluorescence decays follow first order kinetics under ROS exposure, and the *k value* indicates the decay constant. When the 669 nm wavelength light was used to excite the MB-PAA NPs, the *k* value was found to be 0.00131 s^{-1}, which is comparable to the previously reported *k* value, 0.00134 s^{-1}.[6] On the other hand, a 619 nm excitation of the same sample produced only ~30% of the ROS produced by the 669 nm excitation (**Figure A.2**). As discussed in previous section, MB-PAA NP exhibits two absorption peaks, which are a monomer peak at 669 nm and a dimer peak at 619 nm. One of the most dominant pathways for PDT needs the excited photosensitizers to be relaxed into the first triplet state. The dimer peak excitation loses most of the excited energy through "self-quenching" releasing its energy mostly through heat to cause less efficient PDT. The 650 nm

excitation, which was used for both PDT and PALT experiments, showed only a small reduction in ROS production rate, compared to the 669 nm excitation. The 650 nm position was chosen so as to compensate between the ROS production during PALT measurements of oxygen concentration and retaining the PDT effect causing the oxygen depletion.

PDT under the microscope using 9L glioma cells

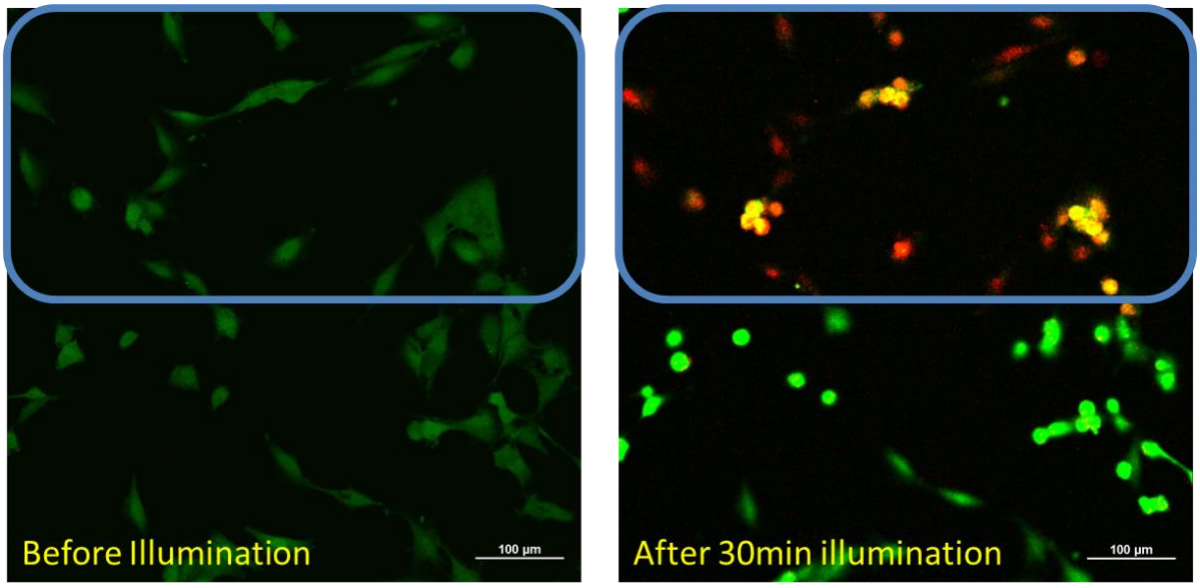

Figure A.3 Fluorescence microscope images of Live (Calcein AM, green)/Dead (PI, red) cell assays, before and after PDT treatment. The blue box (top half) designates the illumination area.

In **Figure A.3** the blue box, at the top, indicates the area of illumination. PDT was performed without rinsing off the MB-PAA NP solution in the cell media. This was to give a better comparison with the later described pulsed laser PDT experiments and PALT experiments, where we used the MB-PAA NP solution without rinsing. Only the region indicated in the blue box was illuminated

with the red laser. After 30 min of illumination, all of the cells had strong PI (red) uptakes and reduced Calcein AM (green) signals, thus indicating cell death. As shown in **Figure A.3**, only the area that was illuminated (blue box) showed PI uptake (red) while the other half did not.

For the confocal microscopy experiment, the top half of the cells showed PI uptake while the bottom half did not, indicating strongly that the PDT was only operative in the area of illumination. Because the MB-PAA NP solution was used without a rinsing off of the nanoparticle solution that did not enter the cells, the ROS are expected to be produced both inside and outside of the cells. However, the results suggest that the ROS produced inside the illumination area do not travel far enough to affect nearby cells, which is expected from the short lifetimes, and thus short diffusion lengths, of most ROS species.[26, 27] Notably, the nanoparticle uptake was also confirmed by microscopy. (**Figure A.3**)

PDT with pulsed laser and oxygen depletion during PDT

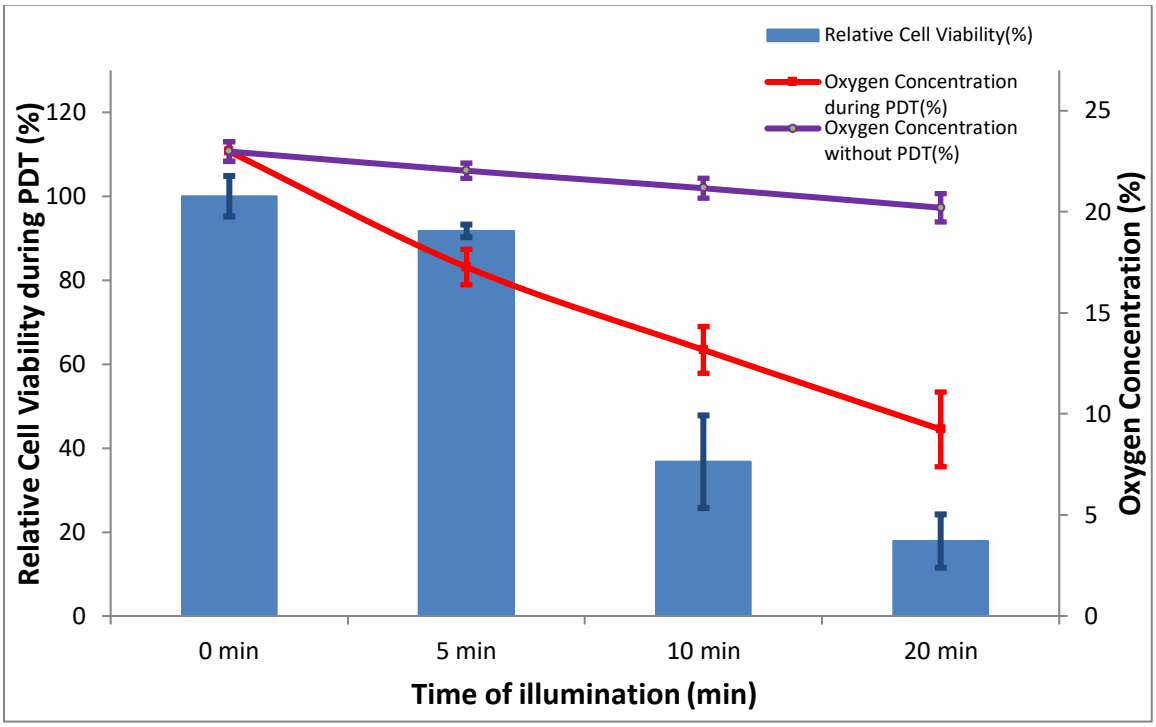

Figure A.4 Blue Boxes indicate the cell survival rate during PDT, using pulsed laser, and Red squares indicate the oxygen concentration at each time point during PDT. All oxygen concentrations were measured by the oximeter. "Oxygen Concentration without PDT (%)" refers to no light illumination with identical conditions to "Oxygen Concentration during PDT (%)".

PDT using pulsed lasers has been reported previously.[28, 29] PDT was performed using a pulsed laser system and the cell viability was monitored (**Figure A.4**). The oxygen concentration was plotted together with the cell survival rate, during PDT, as determined through flow cytometry. After 20 minutes of illumination with the pulsed laser, almost the whole population of cells underwent cell death. Also, the oxygen concentration was monitored, with and without PDT. The oxygen concentration dropped much more drastically with continuous "pump" beam exposure (red line) compared to without light exposure (purple line). The slight oxygen concentration decrease

without light exposure case (purple line) is attributed to the cell metabolism. We did not observe any oxygen depletion when cells were not present in the solution (just MB-PAA NP solution with light illumination). We believe that most of the oxygen depletion shown in **Figure A.4** (red line) is caused by PDT, with only a small fraction thereof due to cell metabolism (purple line), which can be corrected for. The oxygen is consumed during the first stage of PDT, producing ROS as a side product. Presumably, the ROS then oxidize nearby unsaturated biomolecules, disrupting the cell membranes, organelles, and proteins, thus leading to cell death. Thus, the oxygen depletion during PDT may infer cell death and can be used to monitor its therapeutic efficacy.

Oxygen depletion measured with PALT

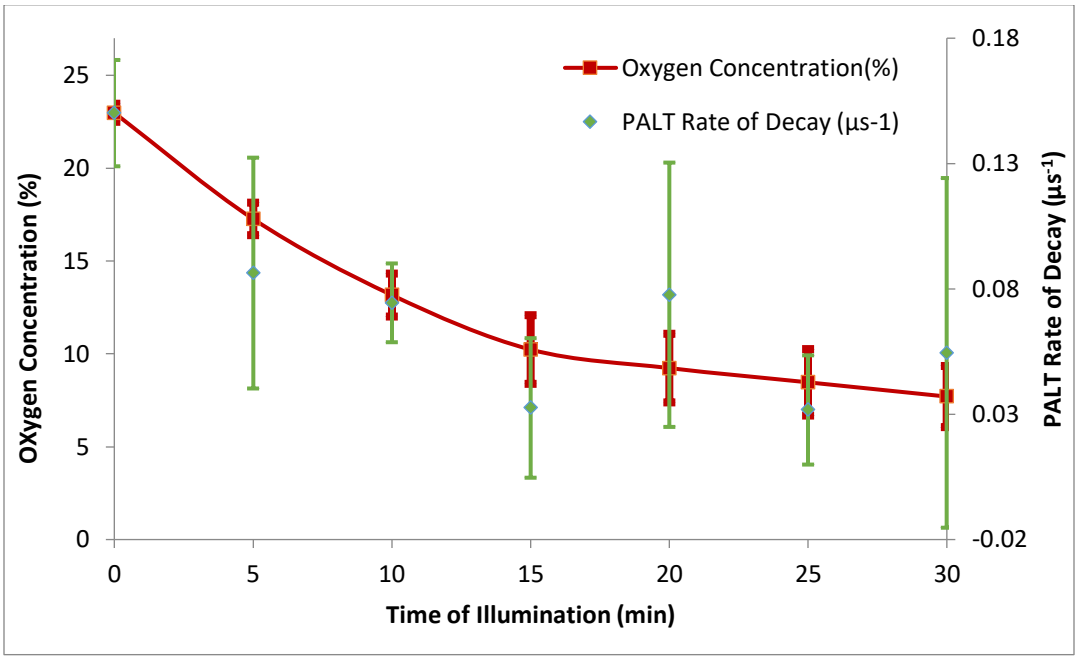

Figure A.5 The Green Triangles indicate the PALT decay rate measurements, after illumination (0 min to 30 min), and the Red Squares indicate the oxygen concentrations measured using the oximeter as the gold standard.

The PALT measurement was applied to monitor the oxygen concentration during PDT. An overlay of oxygen concentration decays, measured by oximeter and PALT is depicted in **Figure A.5**. The 650 nm laser was continuously illuminating during the 20 min period while the 810 nm laser was only illuminating during the PALT measurements (less than 1 min). The PA signals from the 810 nm laser (the "probe" beam) were exponentially fitted with delay times (1, 2, and 4 µs) signals, to give the exponential decay rate constants for the MB-PAA NPs at different oxygen concentrations. The oxygen concentration (red squares, **Figure A.5**) was measured by the oximeter.

The oxygen consumption rate falls off significantly after 20 min of illumination (**Figure A.5**, red line). We suspect that this is due to almost complete cell death by that time, so that the ROS

produced from PDT, not finding nearby oxidation sites, convert back to triplet (ground state) oxygen. Literature reports state that singlet oxygen, which is believed to be the majority of ROS, does not diffuse far [26, 27]. Also, we have performed an analogue experiment under the confocal microscope (**Figure A.3**). The results suggest that the ROS produced inside the illumination area do not travel far enough to affect un-illuminated nearby cells, which is expected from their short lifetimes, and thus short diffusion lengths [26, 27].

A.3 Conclusion

We have demonstrated the feasibility of using the MB-PAA NPs as an oxygen sensor. Previously, we demonstrated PALT both *in vitro* and *in vivo* using other oxygen sensors [12, 15]. We employed a double laser system, with "pump" and "probe" beams, for PALT on MB-PAA NPs. While the PDT experiments were conducted under the same conditions as previously, this time the PALT method was used to measure the oxygen concentration. As depicted in **Figure A.5**, the exponential decay rate shows a strong correlation with the oxygen concentration of the solution as measured with a standard oximeter. The oxygen concentration is constantly decaying because of the PDT process. Thus, we thought that the measurement time was a critical factor in minimizing the PDT effect during measurements. Because we wanted to demonstrate the feasibility of measuring oxygen *in situ*, we minimized the "pump" beam exposure during "probe" beam measurements, taking just 4 spectra (3 spectra from delay time signal and only 1 "pump" beam signal as background) in total. A larger number of delay times, from 0.1 μs to 20 μs, should decrease the errors in the exponential fit.

We believe that this is the first report to demonstrate the feasibility of MB-PAA NPs to be applied as both a diagnostic (measuring oxygen) and a therapeutic (PDT) modality. This unique dual capability of the MB-PAA NPs allows us to demonstrate here a potential non-invasive theranostic operation, by monitoring oxygen depletion during PDT *in situ,* without the addition of secondary probes. Specifically, we demonstrated the correlation between the oxygen concentration and the cytotoxicity of PDT, for 9L glioma cells, showing that the oxygen depletion during PDT can be monitored using PALT. The same approach can be further applied to *in vivo* studies, when treating tumors with PDT and simultaneously monitoring/imaging tissue oxygen photo-acoustically. Another potential advantage of the MB-PAA NPs is that their 619 nm light excitation may be applicable for enhancing PA structural imaging. As pointed out above, although the absorbances at 619 nm and 669 nm were found to be similar, the PDT efficacy at 619 nm was ~70% less than that with the 669 nm excitation (**Figure A.2**). Therefore, such use of MB excitation at 619 nm would allow *longer-term PA structural imaging without much photo-damage to the cells*. Also, similar to the use of Coomassie blue PAA NPs [17, 18], we presume that the MB-PAA NPs could also be applied for tumor surgery delineation, by offering an optical contrast that is visible to the surgeon's naked eye.

A.4 Methods

Materials

Acrylamide (AA), poly(ethylene glycol) dimethacrylate, Mn 550, (PEGDMA), ammonium persulfate (APS), N,N,N′,N′-tetramethylethylenediamine (TEMED), sodium

dioctylsulfosuccinate (AOT), Brij 30, dimethyl sulfoxide (DMSO), Ethanol, phosphate buffered saline (BioReagent, pH 7.4, for molecular biology) and hexane were purchased from Sigma-Aldrich (St. Louis, MO, USA). N-(3-aminopropyl)-methacrylamide hydrochloride (APMA) was purchased from Polysciences (Warrington, PA, USA). Dicarboxymethylene blue NHS ester (DCMB-SE) was purchased from European Molecular Precision Biotech (Berlin, Germany). Anthracene-9, 10-dipropionic acid disodium salt (ADPA), RPMI 1640 Medium, 100X Antibiotic-Antimycotic, Heat Inactivated Fetal Bovine Serum (FBS), Calcein AM, and Propidium Iodide (PI) from Life Technologies (Carlsbad, CA, USA). Annexin V:FITC Apoptosis Detection Kit I was purchased from BD Biosciences (San Jose, CA, USA). 9L rat gliosarcoma cell line was obtained from American Type Culture Collection (Manassas, VA, USA). The water was purified with a Milli-Q system from Millipore Corporation (Billerica, MA, USA). All chemicals were used without further purification.

Preparation of MB-PAA NPs

The MB-PAA NPs were prepared by MB conjugation to PAA as in a previously reported method.[6] All reactions were performed in the dark. The monomer solution was prepared as follows. DCMB-SE (5mg dissolved in 100 μL of DMSO) was added into 0.93 mL of Phosphate Buffered Saline (PBS, pH 7.4) containing AA (368 mg) and APMA (28mg). The monomer solution was stirred for 2 hr at room temperature. Then, AOT (1.07g) and Brij 30 (2.2 mL) were added into 30 mL of Hexane in a round bottom flask equipped with a stirring bar. After 30 min of argon flushing, the monomer solution was injected and flushed with argon for another 15 min. The radical

polymerization was initiated by addition of 100 μL of TEMED and 100 μL of APS (15mg / 100 μL in water), while stirring. After 2 hr, the hexane was evaporated with a rotary evaporator and the resulting MB-PAA NPs were suspended in Ethanol and transferred into an Amicon Stirred Ultrafiltration Cell equipped with a Biomax 300 kDa membrane. The solution was washed with Ethanol and water several times so as to remove any unreacted monomers and surfactants. Then, the MB-PAA NPs water suspension was freeze-dried and stored at -20^{o}C.

Characterization of MB-PAA NPs

A Dynamic Light Scattering instrument (DLS, Delsa Nano C particle analyzer instrument, Beckman Coulter, Brea, CA, USA) was used to determine the particle size. A UV-1601 Spectrometer (Shimadzu, Kyoto, Japan) was used for the Absorption spectra and a FluoroMax-2 Spectrofluorometer (Jobin Yvon Horiba, Kyoto, Japan) was used for the Fluorescence spectra. Both spectrometers were used to determine the dye loadings and NP's characteristics, comparing to the previously reported MB-PAA NP [6].

The ROS production rate can be quantified by the "*k value",* using the ADPA method.[6, 9, 25] ADPA is an ROS scavenger which irreversibly binds with ROS under room temperature. The ROS-oxidized ADPA product has no fluorescence. The reaction between the ROS and the ADPA follows *pseudo first order kinetics,* and the decay rate of the ADPA emission is the *k-value*. To 2 mL of MB-PAA NP (1mg/mL in PBS), 80 μL of ADPA (100 μM in water) was added. The emission spectra of ADPA (370 nm excitation) were taken, while illuminating with a given wavelength of

light (619 nm, 650 nm, or 669 nm), over different time periods (0 sec, 60 sec, 120 sec, and 420 sec). The *k value* was calculated as in our previously reported method.[6, 9, 25] Notably, while both 619 and 669 nm excitation have similar absorbance coefficients for these MB-PAA NPs, the former's ROS production efficiency is about 70% lower.

PDT using Pulsed Laser / Cell viability Experiments

The 9L cells (10^6 cells/ml) were incubated with a MB-PAA NP solution, containing a 1mg/ml FITC Annexin Binding Buffer, for 2 hr. Then, the cell containing solution was transferred into clean plastic cuvettes and sealed with a rubber septum to minimize air flow into the cuvette. An optical parametric oscillator (Surelite OPO plus, Continuum) pumped with the second harmonic of a pulsed neodymium-doped aluminum garnet (Nd: YAG) laser was used, with a pulse-width of 5 ns, at 650 nm wavelength (10mJ), for different time periods (0 min, 5 min, 10 min, and 20 min). The light source was scattered so as to cover the entire area of the cuvette. Each sample was then transferred into a round bottom tube and then FITC-Annexin V (5μL/10^5 cells) and PI (5μL/10^5 cells) were added into the test tubes. The tubes were incubated for 10 min, at room temperature, before introduced to a Flow Cytometer (MoFlo Astrios, Beckman Coulter).

Oxygen Depletion during PDT

The oxygen concentration was measured by an oximeter (Microx TX3, Presens), every 5 min. The 9L cells (10^6 cells/ml) were incubated with MB-PAA NPs for 2 hr and the oxygen

concentration was monitored with and without 650 nm laser illumination (i.e., with or without PDT).

PALT Spectroscopy setup

The schematic of the experiment setup for PALT is shown in **Figure A.6**. An optical parametric oscillator (Surelite OPO plus, Continuum), pumped with the second harmonic of a pulsed neodymium-doped aluminum garnet (Nd: YAG) laser, was used as the "pump laser", with a pulse width of 5 ns and a pulse energy of 10 mJ, at 650 nm wavelength. For the "probe laser", another optical parametric oscillator laser (Vibrant B, Opotek) generated pulsed beam, with a 7-mJ pulse energy, at 810 nm of wavelength was used. The triggers of the two lasers were controlled by a delay generator (DG535, Stanford Research Systems). The two laser beams were overlapped on the transparent cuvette containing the 9L cells pre-incubated with the MB-PAA NPs. The incubation method and conditions were identical to those in the Flow Cytometry experiments (2 hr). The Photoacoustic (PA) signal was detected by a hydrophone (HNC-1500, ONDA) and amplified with a preamplifier (AH-2010-CDBNS, ONDA) and an amplifier (5072PR, Olympus). The signal, digitalized by an oscilloscope (TDS540, Tektronix), was collected (averaged over 50 pulses).

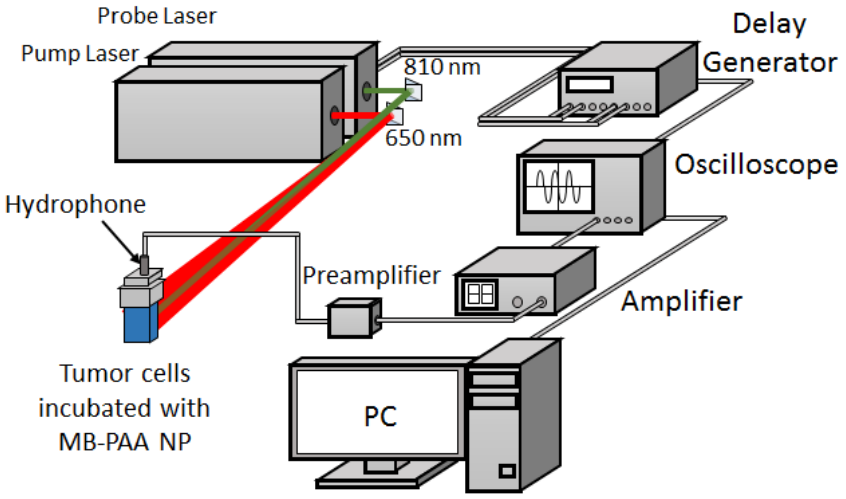

Figure A.6 The schematic of the experimental PALT setup, also used for PDT

To summarize, in our PALT experiments, the MB-PAA NPs are first excited with a *pump beam* at 650 nm, followed by a *probe beam* at 810 nm. The probe beam response measures the MB's transient absorption in the excited triplet state. By varying the time delay between pump and probe beams, the exponential decay curves of the photoacoustic amplitudes can be obtained, by measuring the signal from the probe beam [12-15]. *The rate of the exponential decay correlates directly with the oxygen concentration in the medium.*

A.5 References

1. Hopper, C. Photodynamic therapy: a clinical reality in the treatment of cancer. *The Lancet Oncology* **1**, 212-219 (2000).
2. Huang, Z. A Review of Progress in Clinical Photodynamic Therapy. *Technology in cancer research & treatment* **4**, 283-293 (2005).
3. Brown, S.B., Brown, E.A. & Walker, I. The present and future role of photodynamic therapy in cancer treatment. *The Lancet Oncology* **5**, 497-508 (2004).
4. Lee, Y.-E.K. & Kopelman, R. in Biomedical Nanotechnology, Vol. 726. (ed. S.J. Hurst) 151-178 (Humana Press, 2011).

5. Chatterjee, D.K., Fong, L.S. & Zhang, Y. Nanoparticles in photodynamic therapy: An emerging paradigm. *Advanced Drug Delivery Reviews* **60**, 1627-1637 (2008).
6. Yoon, H.K. et al. Nanophotosensitizers Engineered to Generate a Tunable Mix of Reactive Oxygen Species, for Optimizing Photodynamic Therapy, Using a Microfluidic Device. *Chemistry of Materials* **26**, 1592-1600 (2014).
7. Qin, M. et al. Methylene blue covalently loaded polyacrylamide nanoparticles for enhanced tumor-targeted photodynamic therapy. *Photochemical & Photobiological Sciences* **10**, 832-841 (2011).
8. Tang, W., Xu, H., Park, E.J., Philbert, M.A. & Kopelman, R. Encapsulation of methylene blue in polyacrylamide nanoparticle platforms protects its photodynamic effectiveness. *Biochemical and Biophysical Research Communications* **369**, 579-583 (2008).
9. Tang, W., Xu, H., Kopelman, R. & Philbert, M.A. Photodynamic Characterization and In Vitro Application of Methylene Blue-containing Nanoparticle Platforms¶. *Photochemistry and Photobiology* **81**, 242-249 (2005).
10. Avula, U.M.R. et al. Cell-Specific Nanoplatform-Enabled Photodynamic Therapy for Cardiac Cells. *Heart rhythm : the official journal of the Heart Rhythm Society* **9**, 1504-1509 (2012).
11. Xu, H. et al. Photoexcitation-Based Nano-Explorers: Chemical Analysis inside Live Cells and Photodynamic Therapy. *Israel Journal of Chemistry* **44**, 317-337 (2004).
12. Ashkenazi, S., Huang, S.-W., Horvath, T., Koo, Y.-E.L. & Kopelman, R. Photoacoustic probing of fluorophore excited state lifetime with application to oxygen sensing. *BIOMEDO* **13**, 034023-034023-034024 (2008).
13. Ashkenazi, S. Photoacoustic lifetime imaging of dissolved oxygen using methylene blue. *BIOMEDO* **15**, 040501-040501-040503 (2010).
14. Shao, Q. & Ashkenazi, S. Photoacoustic lifetime imaging for direct in vivo tissue oxygen monitoring. *BIOMEDO* **20**, 036004-036004 (2015).
15. Ray, A., Rajian, J.R., Lee, Y.-E.K., Wang, X. & Kopelman, R. Lifetime-based photoacoustic oxygen sensing in vivo. *BIOMEDO* **17**, 057004 (2012).
16. Tardivo, J.P. et al. Methylene blue in photodynamic therapy: From basic mechanisms to clinical applications. *Photodiagnosis and Photodynamic Therapy* **2**, 175-191 (2005).
17. Nie, G. et al. Hydrogel Nanoparticles with Covalently Linked Coomassie Blue for Brain Tumor Delineation Visible to the Surgeon. *Small* **8**, 884-891 (2012).
18. Ray, A. et al. Targeted blue nanoparticles as photoacoustic contrast agent for brain tumor delineation. *Nano Res.* **4**, 1163-1173 (2011).
19. Karamchand, L. et al. Modulation of hydrogel nanoparticle intracellular trafficking by multivalent surface engineering with tumor targeting peptide. *Nanoscale* **5**, 10327-10344 (2013).
20. Henderson, B.W. et al. Photofrin Photodynamic Therapy Can Significantly Deplete or Preserve Oxygenation in Human Basal Cell Carcinomas during Treatment, Depending on Fluence Rate. *Cancer Research* **60**, 525 (2000).
21. Busch, T.M., Hahn, S.M., Evans, S.M. & Koch, C.J. Depletion of Tumor Oxygenation during Photodynamic Therapy: Detection by the Hypoxia Marker EF3 [2-(2-Nitroimidazol-1[H]-yl)-N-(3,3,3-trifluoropropyl)acetamide]. *Cancer Research* **60**, 2636-

2642 (2000).
22. Sitnik, T.M., Hampton, J.A. & Henderson, B.W. Reduction of tumour oxygenation during and after photodynamic therapy in vivo: effects of fluence rate. *Br J Cancer* **77**, 1386-1394 (1998).
23. Tatum, J.L. Hypoxia: Importance in tumor biology, noninvasive measurement by imaging, and value of its measurement in the management of cancer therapy. *International Journal of Radiation Biology* **82**, 699-757 (2006).
24. Wang, M. & Thanou, M. Targeting nanoparticles to cancer. *Pharmacological Research* **62**, 90-99 (2010).
25. Moreno, M.J. et al. Production of singlet oxygen by Ru(dpp(SO3)2)3 incorporated in polyacrylamide PEBBLES. *Sensors and Actuators B: Chemical* **90**, 82-89 (2003).
26. Kim, S., Tachikawa, T., Fujitsuka, M. & Majima, T. Far-Red Fluorescence Probe for Monitoring Singlet Oxygen during Photodynamic Therapy. *Journal of the American Chemical Society* **136**, 11707-11715 (2014).
27. Kuimova, M.K., Yahioglu, G. & Ogilby, P.R. Singlet Oxygen in a Cell: Spatially Dependent Lifetimes and Quenching Rate Constants. *Journal of the American Chemical Society* **131**, 332-340 (2009).
28. Seguchi, K. et al. Critical Parameters in the Cytotoxicity of Photodynamic Therapy Using a Pulsed Laser. *Lasers Med Sci* **17**, 265-271 (2002).
29. Panjehpour, M., Overholt, B.F., Denovo, R.C., Petersen, M.G. & Sneed, R.E. Comparative study between pulsed and continuous wave lasers for Photofrin® photodynamic therapy. *Lasers in Surgery and Medicine* **13**, 296-304 (1993).